

Master's thesis

2020

Alex Sixie Cao

**NTNU**  
Norwegian University of  
Science and Technology  
Faculty of Engineering  
Department of Structural Engineering

Master's thesis

Alex Sixie Cao

# Dynamic response of semi-rigid timber frames subjected to wind loads

June 2020





Norwegian University of  
Science and Technology

# Dynamic response of semi-rigid timber frames subjected to wind loads

**Alex Sixie Cao**

Civil and Environmental Engineering

Submission date: June 2020

Supervisor: Haris Stamatopoulos, KT

Norwegian University of Science and Technology  
Department of Structural Engineering





Department of Structural Engineering

Faculty of Engineering

NTNU – Norwegian University of Science and Technology

ACCESSIBILITY

OPEN

## MASTER THESIS 2020

SUBJECT AREA: Timber structures Structural dynamics	DATE: 23. June 2020	NO. OF PAGES: 14+100+30
---	------------------------	----------------------------

TITLE:

**Dynamic response of semi-rigid timber frames subjected to wind loads**

BY:

Alex Sixie Cao



SUMMARY:

This thesis investigates the dynamic response of semi-rigid timber frames subjected to wind loads. The dynamic response of more than 1 million frames is assessed with a simplified frequency-domain method called the gust factor approach, and a time-domain method called the generalized wind load. The frames are simulated for three different wind velocities, resulting in more than 12 million simulations in total; qualitative and quantitative observations of the dataset are made; a frequency reduction factor is developed; empirical nonlinear expressions for the accelerations, displacements, and natural frequency are proposed; the accelerations are compared with the ISO 10137-2007 serviceability criteria; and the effect of uniform and nonuniform mass distributions are investigated.

RESPONSIBLE TEACHER:

Associate Professor Haris Stamatopoulos

SUPERVISOR(S)

Associate Professor Haris Stamatopoulos

CARRIED OUT AT:

Department of Structural Engineering, NTNU





Institutt for konstruksjonsteknikk

Fakultet for ingeniørvitenskap


NTNU – Norges teknisk-naturvitenskapelige universitet

TILGJENGELIGHET

ÅPEN

## MASTEROPPGAVE 2020

FAGOMRÅDE: Trekonstruksjoner Konstruksjonsdynamikk	DATO: 23. Juni 2020	ANTALL SIDER: 14+100+30
--	------------------------	----------------------------

TITTEL: <b>Dynamisk respons til halvstive trekonstruksjoner under vindlaster</b>	
UTFØRT AV:  Alex Sixie Cao	

SAMMENDRAG: <p>Denne masteroppgaven tar for seg den dynamiske responsen til halvstive trekonstruksjoner under vindlaster. Den dynamiske responsen til mer enn 1 million rammer er undersøkt ved bruk av <i>vindkastmetoden</i> (engelsk: <i>gust factor approach</i>) i frekvensdomenet, og en <i>generalisert vindlastmetode</i> (engelsk: <i>generalized wind load</i>) i tidsdomenet. Rammene simuleres for tre ulike vindhastigheter som resulterer i mer enn 12 millioner simuleringer totalt; kvalitative og kvantitative observasjoner for datasettet gjøres; en <i>frekvensreduksjonsfaktor</i> (engelsk: <i>frequency reduction factor</i>) utvikles; empiriske ikkelineære uttrykk for akselerasjoner, forskyvninger og naturlig frekvens foreslås; akselerasjonene sammenliknes med kriterier for bruksgrensetilstanden i ISO 10137-2007; og effekten av uniform og ikkeuniform fordeling av masse undersøkes.</p>
FAGLÆRER: Førsteamanuensis Haris Stamatopoulos
VEILEDER(E): Førsteamanuensis Haris Stamatopoulos
UTFØRT VED: Institutt for konstruksjonsteknikk, NTNU





## Preface

This thesis has been written in completion of the Master of Science in Civil & Environmental Engineering at the Norwegian University of Science and Technology (NTNU). The work was carried out in the spring semester of 2020 at the Department of Structural Engineering with the Timber Structures Group.

The topic and contents of this thesis is a result of the author's interest in structural dynamics, timber structures, a blank canvas, and free reins provided by supervisor Associate Professor Haris Stamatopoulos at NTNU. The result of this combination has been an incremental evolution of the topic and scope, with a free exchange of ideas and discussions between the author and supervisor.

The culmination of this process is a thesis which analyses the dynamic response of planar semi-rigid timber frames subjected to static and dynamic wind loads. The analyses are based on a MATLAB routine that has been developed as part of the work with this thesis. The routine has simulated more than 1 million unique moment-resisting timber frames subjected to different wind loads, which has resulted in more than 12 million simulations in total.

Important results in this thesis are the proposal of a novel frequency reduction factor, which shows the relation between the natural frequency of the structure and the connection stiffness; the effect of adding passive mass uniformly to the whole structure, or nonuniformly to only one floor; quantification of the technical feasibility of semi-rigid timber skeleton frames; and the sensitivity of the dynamic response to different structural parameters.

Due to the generation and post-processing of the large amount of data, access to sufficient computing power has proven to be a challenge. This has been solved by using five different computers running simulations simultaneously. For this, I would like to thank my brother for granting me access to his desktop computer which has run the bulk of the simulations, and my supervisor Associate Professor Haris Stamatopoulos for granting me access to his desktop computer which has also run a substantial part of the simulations. For the initial guidance in the vast field of wind engineering, I would also like to thank Professor Ole Øiseth at NTNU for pointing me in the right direction. For the excellent supervision and numerous constructive discussions in the work with this thesis, I would like to thank my supervisor Associate Professor Haris Stamatopoulos.

For my exchange year at Tsinghua University in Beijing, China, I would like to thank all the friends and lecturers who made it into a unique experience. Special thanks are due to my lecturer and friend, Tenured Associate Professor Xiaohui Cheng, in the course Elasticity & Plasticity, who sparked my interest in research.

For my time in Trondheim, I would like to thank all the friends and lecturers who have made this journey a memorable experience. Special recognition is due to my partner, of whom I have learned a great deal from, for her continuous support and encouragement, and for the many memorable moments. I would also like to thank my family, for their continuous support and guidance.

Trondheim, June 23, 2020



Alex Sixie Cao



## Abstract

The Eurocodes contain extensive information on the design principles and guidelines for concrete and steel structures. However, there is an information and knowledge gap on the design principles and concepts of load-bearing timber structures. The lack of knowledge comes from the long-standing ban on the use of timber in structural elements worldwide after extensive city-wide fires in small timber structures. However, the use of timber in structural elements is becoming more and more common as the bans on timber structures are lifted. Due to the long-standing ban on timber structures, the design concepts, and principles in the design of such structures have not been developed to the extent of steel and concrete structures. At present, the timber industry is expanding at an exponential rate, and the design principles and concepts are developed at a very fast pace.

One of the main challenges in timber structures is fulfilling the serviceability criteria with respect to deformations and accelerations. To address this challenge, this thesis is directed at the dynamic response of semi-rigid timber structures subjected to dynamic wind loads. The Eurocodes use a simplified method, called the gust factor approach, to estimate the wind loads and the dynamic response. In this thesis, both the gust factor approach and the theoretical time-domain generalized wind load method are used to estimate the dynamic response. Due to the simplifications of the gust factor approach, a comparison of the gust factor approach and the time-domain generalized wind load method is performed.

Based on the gust factor approach and the time-domain generalized wind load method, an extensive database of the dynamic response consisting of semi-rigid timber frames with different stiffness, damping, and mass properties is generated. The timber frames are subjected to different wind loads in terms of the fundamental value of the basic wind velocity. In total, more than 1 million unique timber frames are simulated for different wind loads, resulting in a database consisting of more than 12 million simulations in total. The database is visualized in as histograms, and some general observations are made. Nonlinear regressions are formulated for the accelerations, displacements, and the natural frequency, and the deviations between the gust factor approach and the time-domain generalized wind load are investigated.

In this thesis, a sigmoid relationship between the natural frequency and the connection stiffness is hypothesized, and subsequently validated. Based on the observed relationship, a novel frequency reduction factor is formulated, and a support rigidity index is defined to account for the rotational support stiffness. From the frequency reduction factor, the natural frequency of semi-rigid frames can be predicted with an average error of less than 5% within the simulated range.

The effect of uniform and nonuniform mass distributions in the structure is investigated, and the resulting data are discussed for both the gust factor approach and the time-domain generalized wind load. A deviation between the two methods is discovered in relation to a nonuniform mass distribution, and the effects of the mass distribution are presented and discussed. The optimal location for passive mass is at the top of the structure, where the accelerations can be reduced significantly if sufficient mass is added.



## Sammendrag

Eurokodene inneholder utfyllende informasjon om dimensjoneringsprinsipper og veiledning for betong- og stålkonstruksjoner. For bærende konstruksjoner i tre er det mangler innenfor dimensjoneringsprinsipper og veiledning ved valg av konsept for bæresystem. Manglene skyldes langvarig historisk murtvang og forbud mot bruk av tre i større konstruksjoner som følge av store bybranner i små trehus. De siste tiårene har forbudet mot bruk av tre i mindre og større konstruksjoner blitt hevet i flere land, og bruken av tre som bærende materiale har blitt mer og mer utbredt. På grunn av det langvarige forbudet mot bruk av tre som bærende materiale, har dimensjoneringsprinsipper og konseptuelle løsninger i trekonstruksjoner ikke blitt utviklet i samme grad som for stål og betongkonstruksjoner. I dag vokser industrien for trekonstruksjoner eksponentielt, og dimensjoneringsprinsipper og konsepter utvikles i et svært høyt tempo.

En av hovedutfordringene i trekonstruksjoner er å tilfredsstille bruksgrensetilstanden med tanke på deformasjoner og akselerasjoner. For å bidra til å løse denne utfordringen, tar denne masteroppgaven for seg den dynamiske responsen til halvstive trekonstruksjoner under dynamiske vindlaster. Eurokodene bruker en forenklet metode kalt *vindkastmetoden* (engelsk: *gust factor approach*) for å estimere vindlaster og dynamisk respons av konstruksjoner. I denne masteroppgaven blir vindkastmetoden og en teoretisk *generalisert vindlastmetode* (engelsk: *generalized wind load*) i tidsdomenet brukt til å estimere vindlaster og dynamisk respons av konstruksjoner. På grunn av forenklinger som er gjort i vindkastmetoden, sammenliknes den med den generaliserte vindlastmetoden.

Basert på vindkastmetoden og den generaliserte vindlastmetoden i tidsdomenet skapes en stor database av den dynamiske responsen til halvstive plane rammer i tre med forskjellige stivhets-, dempings- og masseegenskaper. Trerammene utsettes for ulike vindlaster i form av referansevindhastigheten. Til sammen er mer enn 1 million forskjellige trerammer simulert for forskjellige vindlaster. Dette har resultert i en database som inneholder mer enn 12 millioner simuleringer totalt. Databasen er visualisert i form av histogrammer, og noen generelle observasjoner gjøres. Ikkelineære empiriske uttrykk foreslås for akselerasjonene, deformasjonene og for de naturlige frekvensene, og forskjellene mellom vindkastmetoden og den generaliserte vindlastmetoden i tidsdomenet undersøkes.

I denne masteroppgaven fremsettes og valideres en hypotese om en sigmoidisk oppførsel mellom den naturlige frekvensen og rotasjonsstivheten til knutepunkter. Basert på den observerte oppførselen blir en *frekvensreduksjonsfaktor* (engelsk: *frequency reduction factor*) formulert, og en *stivhetsindeks for randbetingelsene* (engelsk: *support rigidity index*) til konstruksjonen definert. Stivhetsindeksen for randbetingelsene tar høyde for rotasjonsstivheten til knutepunktene i søylene mot fundamentet. Ved bruk av frekvensreduksjonsfaktoren kan den naturlige frekvensen til halvstive rammer estimeres med en gjennomsnittlig feil på mindre enn 5% innenfor grensene til de simulerte rammene.

Effekten av jevnt og ujevnt fordelt masse i konstruksjonen undersøkes, og resultatene diskuteres for både vindkastmetoden og den generaliserte vindlastmetoden. En forskjell i resultatene mellom de to metodene oppdages i forbindelse med ujevnt fordelt masse i konstruksjonen, og effekten av fordelingen av masse presenteres. For en ujevnt fordelt masse, vil ekstra masse plassert på toppen av konstruksjonen være best med tanke på dynamisk respons for vindlaster. Ved en slik plassering av ekstra masse kan akselerasjonene bli redusert signifikant dersom tilstrekkelige mengder masse blir brukt.



# Contents

1	Notation .....	1
2	Introduction .....	7
3	Theory .....	9
3.1	Finite element analysis .....	9
3.2	Random vibrations .....	11
3.3	Wind characteristics .....	12
3.4	The gust factor approach .....	14
3.4.1	Bluff body aerodynamics .....	14
3.4.2	Aerodynamic admittance functions .....	15
3.4.3	Mechanical admittance function .....	16
3.4.4	Wind spectrum .....	17
3.4.5	Response spectrum .....	17
3.4.6	Resonant and background response .....	18
3.4.7	Peak response .....	19
3.4.8	Structural factor .....	20
3.5	Generalized wind load .....	21
3.5.1	Modal analysis .....	21
3.5.2	Fluctuating wind force spectrum .....	22
3.6	Spectral representation .....	23
3.6.1	Discrete Fourier transform .....	23
3.6.2	Spectral representation .....	24
3.7	Numerical integration .....	25
3.8	Wind loading model .....	27
4	Method .....	31
4.1	Structural system .....	32
4.2	Reference frame .....	33
4.3	Parameters .....	34
4.4	Simulations .....	38
4.5	Post-processing .....	39
4.5.1	Displacements .....	40
4.5.2	Accelerations .....	40
4.6	Mode shapes .....	41

5	Results and discussion .....	43
5.1	Reference frame.....	43
5.2	Simulations.....	55
5.2.1	Natural frequency.....	55
5.2.2	Mode shape parameter .....	58
5.2.3	Accelerations.....	59
5.2.4	Displacements .....	62
5.3	Nonlinear regression.....	65
5.3.1	Natural frequency.....	65
5.3.2	Frequency reduction factor .....	68
5.3.3	Accelerations.....	71
5.3.4	Displacements .....	74
5.4	Serviceability requirements in ISO 10137-2007 .....	78
5.5	Mass and height factor .....	80
5.5.1	Uniform mass distribution.....	80
5.5.2	Nonuniform mass distribution .....	82
6	Limitations and future work.....	91
6.1	Limitations.....	91
6.1.1	Structural model.....	91
6.1.2	Wind engineering .....	93
6.1.3	Proposed nonlinear expressions .....	94
6.1.4	Mass distribution .....	95
6.2	Future work.....	95
7	Conclusion.....	97
	References.....	99
	Appendices .....	101



# 1 Notation

## Roman symbols

$A$	Cross sectional area; windward face area; spatial coordinate
$A_{N,h}$	Normalized acceleration
$A_{N,m}$	Normalized acceleration
$dA$	Infinitesimal increment of $A$
$A_B$	Background response
$A_R$	Resonant response
$\mathbf{A}$	Vector of constants
$b$	Windward width
$b_b$	Beam width
$b_c$	Column width
$B$	Resonant response
$c$	Structural damping coefficient
$c_d$	Dynamic component
$c_e$	Exposure factor
$c_f$	Force coefficient
$c_i$	Exponent
$c_{\text{prob}}$	Probability factor
$c_s$	Size component
$c_s c_d$	Structural factor
$coh_{v_k v_l}$	Coherence function of $v_k$ and $v_l$
$\mathbf{c}$	Damping matrix
$C_D$	Drag coefficient
$C_y$	Horizontal decay coefficient
$C_z$	Vertical decay coefficient
$\mathbf{C}$	Modal damping matrix
$d$	Building depth
$\mathbf{D}_{(n_{\text{DOFs}} \times 1)}$	Displacement vector
$\mathbf{D}_c$	Condensed degrees of freedom
$\mathbf{D}_r$	Retained degrees of freedom
DOFs	Degrees of freedom
$E$	Modulus of elasticity
$E[x(t)]$	Expected value of $x(t)$
$EI_b$	Beam stiffness
$EI_c$	Column stiffness
$f$	Frequency
$f_1$	First natural frequency
$f_L$	Normalized frequency
$f_n$	Natural frequency
$f_{n,\text{pred}}$	Predicted natural frequency
$f_{n,\infty}$	Natural frequency of a rigid frame
$F$	Wind force
$F_p$	Peak wind load
$\bar{F}$	Mean wind force

$\hat{F}$	Turbulent wind force
$\mathbf{F}$	Modal force vector
$\mathcal{F}$	Fourier transform
$G$	Modulus of shear; gust factor
GF	Gust factor approach
GWL	Generalized wind load
$h$	Building height
$h_b$	Beam height
$h_c$	Column height
$H(\omega)$	Mechanical admittance function
$H^*(\omega)$	Complex conjugate of the mechanical admittance function
$\mathbf{H}^H$	Hermitian transpose of the mechanical admittance matrix
$I$	Second moment of area
$I_u$	Turbulence intensity
IDR	Inter-story drift
$k$	Structural stiffness
$k^{\text{eff}}$	Effective stiffness
$k_p$	Peak factor for the response
$k_r$	Terrain factor
$k_s$	Support rigidity index
$k_v$	Peak velocity factor
$k_{x,\text{sup}}$	Horizontal support stiffness
$k_{x,z,\text{sup}}$	Lateral support stiffness
$k_{z,\text{sup}}$	Vertical support stiffness
$k_\theta$	Rotational connection stiffness
$k_{\theta,\text{adj}}$	Adjusted connection stiffness
$k_{\theta,\text{sup}}$	Rotational support stiffness
$K_x$	Non-dimensional coefficient
$\mathbf{k}$	Stiffness matrix
$\mathbf{k}_{e(6 \times 6)}^c$	Stiffness matrix, column
$\mathbf{k}_{e(6 \times 6)}^b$	Stiffness matrix, beam
$\mathbf{K}$	Modal stiffness matrix
$\bar{\mathbf{K}}$	Augmented stiffness matrix
$\mathbf{K}^{\text{eff}}$	Effective stiffness matrix
$\mathbf{K}_{\text{cc}}$	Condensed stiffness matrix
$\mathbf{K}_{\text{cr}}$	Condensed, retained stiffness matrix
$\mathbf{K}_{\text{rr}}$	Retained stiffness matrix
$\mathbf{K}_{\text{rc}}$	Retained, condensed stiffness matrix
$L_b$	Beam length
$L_c$	Column length
$L_e$	Element length
$L_u$	Turbulence length scale
$m$	Mean value; structural mass
$m_x$	Mean value of $x$
$m_y$	Mean value of $y$
$M_n$	Normalized modal mass per unit length
$\mathbf{m}$	Mass matrix

<b>M</b>	Modal mass matrix
$n_{\text{bay}}$	Number of bays
$n_{\text{DOFs}}$	Number of degrees of freedom
$n_{\text{floor}}$	Number of floors
$n_p$	Number of parameters
$N$	Number of nodes; number of signals
$p(t)$	External force
$p(x)$	Probability density function of $x$
$p^{\text{eff}}$	Effective excitation force
$p_L$	Line load
$p_p$	Equivalent static wind pressure
$p_s$	Surface load
$p_0$	Unit static force
<b>p</b>	Excitation force vector
$P_0$	Non-dimensional quantity
$P_1$	Non-dimensional quantity
$P(x)$	Probability of $x$
$P(\omega)$	Fourier transform of $p(t)$
<b>p</b> <sup>eff</sup>	Effective excitation force vector
$q$	Velocity pressure
$q_p$	Peak velocity pressure
$R$	Resonant response
$R_e$	Reynold's number
$R_{\hat{F}}$	Autocorrelation function of $\hat{F}$
$R_h(\eta_h)$	Aerodynamic admittance function
$R_b(\eta_b)$	Aerodynamic admittance function
$R_{\hat{u}}$	Autocorrelation function of $\hat{u}$
$R_{xx}$	Autocorrelation function of $x(t)$ and $x(t)$
$R_{xy}$	Autocorrelation function of $x(t)$ and $y(t)$
$R_{yx}$	Autocorrelation function of $y(t)$ and $x(t)$
$R_{yy}$	Autocorrelation function of $y(t)$ and $y(t)$
$R^2$	Pearson $R^2$ ; $R^2$
<b>R</b> <sub>xy</sub>	Autocorrelation matrix of $x(t)$ and $y(t)$
<b>R</b>	Augmented nodal force vector
<b>R</b> <sub>c</sub>	Condensed nodal force vector
<b>R</b> <sub>r</sub>	Retained nodal force vector
$s$	Frame spacing
$S_{\hat{F}}$	Cross-spectral density of $\hat{F}$
$S_L$	Normalized cross-spectral density of the Kaimal wind spectrum
$S_u$	Cross-spectral density of $u$
$S_u^n$	Normalized cross-spectral density of $u$
$S_{\hat{u}}$	Cross-spectral density of $\hat{u}$
$S_{xx}$	Cross-spectral density of $x(t)$ and $x(t)$
$S_{\dot{x}\dot{x}}$	Cross-spectral density of $\dot{x}(t)$ and $\dot{x}(t)$
$S_{xy}$	Cross-spectral density of $x(t)$ and $y(t)$
$S_{yx}$	Cross-spectral density of $y(t)$ and $x(t)$
$S_{yy}$	Cross-spectral density of $x(t)$ and $y(t)$

$\tilde{S}_k$	Smoothed continuous spectrum
$\mathbf{S}_{xy}$	Cross-spectral density matrix for $x(t)$ and $y(t)$
$t$	Time
$dt$	Infinitesimal increment of $t$
$\Delta t$	Increment of $t$
$T$	Period; averaging time
$T_L$	Non-dimensional averaging time
$u$	Wind velocity
$u_p$	Peak wind velocity
$u_*$	Friction velocity
$\bar{u}$	Mean wind velocity
$\hat{u}$	Turbulent wind velocity
$v_b$	Basic wind velocity
$v_m$	Mean wind velocity
$x$	Response displacement; spatial coordinate
$dx$	Infinitesimal increment of $x$
$x_i$	Parameter
$x_p$	Peak response displacement
$x_{p,GF}$	Peak response displacement for the gust factor approach
$x_{p,GWL}$	95% fractile of the response displacement for the generalized wind load
$x(t)$	Random process
$(x_{st})_0$	Static displacement
$\bar{x}$	Static displacement response
$\dot{x}(t)$	Response velocity
$\ddot{x}(t)$	Response acceleration
$\ddot{x}_{p,GF}$	95% fractile of the response acceleration for the gust factor approach
$\ddot{x}_{p,GWL}$	95% fractile of the response acceleration for the generalized wind load
$\mathbf{x}$	Response displacement vector; random process
$\dot{\mathbf{x}}$	Response velocity vector
$\ddot{\mathbf{x}}$	Response acceleration vector
$X(\omega)$	Fourier transform of $x(t)$
$\mathbf{X}$	Lower triangular Cholesky decomposition of $\mathbf{S}_{xx}$
$\mathbf{X}^*$	Hermitian transpose of $\mathbf{X}$
$y$	spatial coordinate
$y_{\text{pred}}$	Predicted value
$dy$	Infinitesimal increment of $y$
$y(t)$	Random process
$z$	Distance to surface; spatial coordinate
$dz$	Infinitesimal increment of $z$
$z_{\text{min}}$	Minimum distance
$z_{\text{max}}$	Maximum distance
$z_s$	Reference height
$z_0$	Roughness length

## Greek symbols

$\beta$	Integration constant, Newmark integration
$\gamma$	Integration constant, Newmark integration
$\delta$	Logarithmic decrement
$\varepsilon$	Percent bias
$\bar{\varepsilon}$	Average error
$\zeta$	Mode shape parameter
$\eta$	Frequency reduction factor
$\eta_h$	Height factor
$\eta_m$	Mass factor
$\boldsymbol{\eta}(t)$	Modal displacement coordinate
$\dot{\boldsymbol{\eta}}(t)$	Modal response velocity coordinate
$\ddot{\boldsymbol{\eta}}(t)$	Modal response acceleration coordinate
$\theta$	Rotational degree of freedom
$\kappa$	Shear correction factor
$\lambda$	Scalar
$\mu$	Mass per unit height
$\nu$	Up-crossing frequency
$\xi$	Damping ratio
$\Pi$	Product
$\rho$	Correlation coefficient
$\rho_a$	Air density
$\rho_e$	Equivalent density
$\rho_{xy}$	Correlation coefficient of $x$ and $y$
$\sigma$	Standard deviation
$\sigma_u$	Standard deviation of $u$
$\sigma_x$	Standard deviation of $x$
$\sigma_{\dot{x}}$	Standard deviation of $\dot{x}$
$\sigma_{\ddot{x}}$	Standard deviation of $\ddot{x}$
$\sigma_y$	Standard deviation of $y$
$\sigma^2$	Variance
$\ddot{\sigma}_{GF}$	Standard deviation of the response acceleration for the gust factor approach
$\ddot{\sigma}_{GWL}$	Standard deviation of the response acceleration for the generalized wind load
$\Sigma$	Sum
$\tau$	Time-shift
$d\tau$	Infinitesimal increment of $\tau$
$\phi$	Vibration mode; phase angle
$\Phi$	Modal matrix
$\chi$	Aerodynamic admittance function
$\chi_{\phi_i}$	Modal aerodynamic admittance function
$\omega$	Angular frequency
$\Delta\omega$	Increment of $\omega$
$\omega_n$	Angular natural frequency
$\omega_{\max}$	Maximum angular natural frequency
$\Omega_{cr}$	Critical sampling frequency



## 2 Introduction

Traditional building materials such as concrete and steel have been used in the construction of tall buildings for many decades. The dynamic response of such structures is well known, and the design principles are well developed. However, concrete and steel, timber structures are both lighter and more flexible than comparable structures in concrete and steel. Due to the lightness and flexibility of timber structures, they are superior with respect to seismic design and in the design of foundations. However, it also brings with it challenges with respect to the serviceability limit state, especially for vibrations.

The low density of timber structures makes them prone to the transmission of vibrations. Such challenges include the transmission of sounds through timber decks, and wind-induced vibrations. To deal with sound transmission in timber decks, solutions have been proposed and are readily available. However, wind-induced vibrations is another challenge entirely to be overcome.

In engineering, connections and corners are often regarded as either pinned or rigid. However, the actual behavior of connections is neither pinned nor rigid, but semi-rigid. For steel and concrete structures, connections with an almost rigid behavior exist and are widely used in the design of such structures. In timber structures, one of the main challenges is the design of semi-rigid connections. Today, most of the connections in timber structures are pinned or very flexible. The flexibility of the connections has forced structural engineers to use extensive bracing systems and shear walls to provide lateral stiffness to the structure. This reduces the flexibility for architects in their design of timber structures. The result is often massive beams running diagonally through rooms as in the record-breaking projects Mjøstårnet and Treet in Norway.

The development of a semi-rigid or moment-resisting connection has therefore become one of the main areas of research in timber engineering. When a semi-rigid connection is developed and adopted in industry, it will remove a chokepoint for the design of tall timber structures. This will allow for a more efficient use of timber materials, taller structures, and better serviceability. Several new tall timber structures have been envisioned in the future, one of them being 350 m tall skyscraper proposed by the Tsukaba Research Institute for the Japanese timber producer Sumitomo Forestry (2018). In their concept, a hybrid steel and timber frame with steel bracing will be used. To enable such a structure, semi-rigid connections are a necessity for structural efficiency.

Today, semi-rigid timber frames are a novelty in its own. Most of the existing semi-rigid timber frames are on laboratory scale. One such system is the semi-rigid frame system developed by the Norwegian University of Science and Technology as part of the research project Woodsol. The semi-rigid frame system developed in Woodsol uses threaded rods at an angle to the grain to achieve a rotational stiffness in the connections. The angle is dependent on the length of the rods. A composite glued laminated timber and laminated veneer lumber timber deck has also been developed as part of Woodsol, of which the static and dynamic properties have been investigated numerically and physically on a full-scale prototype. The connection stiffnesses, frame spacing, and beam stiffnesses in this master thesis are based on the Woodsol system (Stamatopoulos, 2018).

Most analyses to date involve a limited number of structures and frames for the assessment of semi-rigid connections with respect to the static and dynamic response. In this thesis, the dynamic response of semi-rigid tall timber structures will be analyzed quantitatively by simulating more than 1 million timber frames subjected to different wind loads. In total, more than 12 million

simulations are performed and will be the basis for the analysis of the dynamic response. In the simulations, the effect of beam and column stiffnesses, number of bays, number of floors, support conditions, surface load, and connection stiffness on the dynamic response of the structure will be assessed.

Through the simulation of the dynamic response of several million frames, the general trends and behavior of such tall timber structures can be observed and assessed quantitatively. The importance of the different parameters can be assessed quantitatively, and requirements of the different parameters to fulfill the serviceability limit state can be identified. From the large database, empirical expressions are developed for the accelerations, displacements, and natural frequencies. A frequency reduction factor is developed, showing the effect of the connection stiffness on the natural frequency. The effect of uniform and nonuniform mass distributions in the structure is investigated, and its effect on the dynamic response is assessed quantitatively and qualitatively. This work has the potential to greatly simplify engineering procedures, make the design process more graspable, and enable the design and construction of taller timber structures in a wider range than what is possible today.

In short, the work in this thesis is on the dynamic response of moment-resisting timber frames subjected to wind loads. The computation of the dynamic response is based on the well-known gust factor approach proposed by Davenport (1961a), and the generalized wind load outlined in Kareem (1986) in the time-domain. For the gust factor approach, the detailed computations follow the Eurocodes (NS-EN 1991-1-4:2005), but only for turbulent loading and the dynamic response. For the generalized wind loading<sup>1</sup>, the computations are based on the simulation of a wind force time series generated from the wind spectrum in the Eurocodes (NS-EN 1991-1-4:2005 Annex B). From the wind force time series, the dynamic response is computed.

This thesis consists of five parts. First, the theoretical foundation for the work is presented. This includes a brief description of the finite element approach, an introduction to random vibrations theory, a description of wind characteristics, derivation of the gust factor approach, derivation of the generalized wind load, a description on the generation of time series, and the derivation of a numerical integration scheme. Second, the method of analysis, parameters, simulations, and post-processing are described. Third, the results are presented and discussed. This includes results and discussions of a reference frame for which a parameter study is conducted, simulations of the frames, nonlinear regressions of the natural frequency, a frequency reduction factor, the response accelerations and displacements, ISO 10137 serviceability requirements, and the effect of uniform and nonuniform mass distributions. Fourth, limitations are discussed and important topics for future work are identified. Fifth and last, a conclusion of the work in this thesis is presented.

---

<sup>1</sup> For the remainder of this thesis, the *time-domain generalized wind load* is referred to as the *generalized wind load*.



### 3 Theory

In this chapter, the basic theoretical concepts in this thesis and their mathematical descriptions are described and derived. First, the finite element formulations of the stiffness matrix and mass matrix are described. Second, some important concepts in random vibrations theory are introduced. Third, a conceptual description of wind characteristics is introduced. Fourth, the gust factor approach for spectral or frequency-domain description of structural response from wind excitation is derived. Fifth, the generalized wind load method for time-domain analysis is derived. Sixth, a spectral representation method for the generation of time-series from a spectral density is derived. Seventh, an overview of three different wind loading models are presented.

#### 3.1 Finite element analysis

In this thesis, cubic 6DOF Timoshenko beam elements are used to formulate the columns. The local stiffness matrix for the columns can be expressed as:

$$\mathbf{k}_{e(6 \times 6)}^c = \begin{bmatrix} \frac{EA}{L_e} & 0 & 0 & -\frac{EA}{L_e} & 0 & 0 \\ 0 & \frac{12EI}{(1+\alpha)L_e^3} & -\frac{6EI}{(1+\alpha)L_e^2} & 0 & -\frac{12EI}{(1+\alpha)L_e^3} & \frac{6EI}{(1+\alpha)L_e^2} \\ 0 & -\frac{6EI}{(1+\alpha)L_e^2} & \frac{(4+\alpha)EI}{(1+\alpha)L_e} & 0 & \frac{6EI}{(1+\alpha)L_e^2} & \frac{(2-\alpha)EI}{(1+\alpha)L_e} \\ -\frac{EA}{L_e} & 0 & 0 & \frac{EA}{L_e} & 0 & 0 \\ 0 & -\frac{12EI}{(1+\alpha)L_e^3} & \frac{6EI}{(1+\alpha)L_e^2} & 0 & \frac{12EI}{(1+\alpha)L_e^3} & -\frac{6EI}{(1+\alpha)L_e^2} \\ 0 & -\frac{6EI}{(1+\alpha)L_e^2} & \frac{(2-\alpha)EI}{(1+\alpha)L_e} & 0 & \frac{6EI}{(1+\alpha)L_e^2} & \frac{(4+\alpha)EI}{(1+\alpha)L_e} \end{bmatrix}, \quad \alpha = \kappa \frac{12EI}{GAL_e^2},$$

where  $L_e$  is the element length,  $E$  is the elastic modulus,  $A$  is the cross-sectional area,  $I$  is the second moment of area,  $G$  is the shear modulus, and  $\kappa$  is the shear coefficient or shear correction factor. For rectangular cross sections,  $\kappa$  is 6/5.

For the beams, cubic 6DOF Euler-Bernoulli beam elements with rotational springs at the ends are used. The local stiffness matrix can be expressed as (Lui & Lopes, 1997):

$$\mathbf{k}_{e(6 \times 6)}^b = \frac{EI}{L_e} \begin{bmatrix} \frac{A}{I} & 0 & 0 & -\frac{A}{I} & 0 & 0 \\ 0 & 2\frac{S_{ii} + S_{jj}}{L_e^2} & \frac{S_{ii} + S_{ij}}{L_e} & 0 & -2\frac{S_{ii} + S_{ij}}{L_e^2} & \frac{S_{ii} + S_{ij}}{L_e} \\ 0 & \frac{S_{ii} + S_{ij}}{L_e} & S_{ii} & 0 & -\frac{S_{ii} + S_{ij}}{L_e} & S_{ij} \\ -\frac{A}{I} & 0 & 0 & \frac{A}{I} & 0 & 0 \\ 0 & -2\frac{S_{ii} + S_{ij}}{L_e^2} & -\frac{S_{ii} + S_{ij}}{L_e} & 0 & 2\frac{S_{ii} + S_{ij}}{L_e^2} & -\frac{S_{ii} + S_{ij}}{L_e} \\ 0 & \frac{S_{ii} + S_{ij}}{L_e} & S_{ij} & 0 & -\frac{S_{ii} + S_{ij}}{L_e} & S_{ii} \end{bmatrix},$$

$$S_{ii} = \left(4 + \frac{12EI}{L_e k_\theta}\right) \frac{1}{R^*}, \quad S_{ij} = \frac{2}{R^*}, \quad R^* = \left(1 + \frac{4EI}{L_e k_\theta}\right)^2 - \left(2 \frac{EI}{L_e k_\theta}\right)^2$$

where  $k_\theta$  is the rotational beam-to-column stiffness, and the indexes  $i$  and  $j$  denote the different beam nodes.

By implementing the beam-to-column stiffness in the beam element, the columns are modelled as continuous and the beams as discontinuous elements. Due to existing measurements of the stiffness of a timber slab element based on Euler-Bernoulli beam theory, the beam elements are formulated as Euler-Bernoulli beams.

In the global stiffness matrix, each node has three DOFs  $u$ ,  $v$ , and  $\theta$ . Thus, the total number of DOFs  $n_{\text{DOFs}}$  for the uncondensed global stiffness matrix can be found from the following expression:

$$n_{\text{DOFs}} = 3 \cdot N = 3 \cdot (n_{\text{floor}} + 1)(n_{\text{bay}} + 1),$$

where  $n_{\text{floor}}$  is the number of floors,  $n_{\text{bay}}$  is the number of bays, and  $N$  is the number of nodes. For the reference frame with ten floors and two bays, the uncondensed global stiffness matrix containing all DOFs is thus a  $99 \times 99$  size matrix.

By arranging the global DOFs such that the displacement vector can be expressed as:

$$\mathbf{D}_{(n_{\text{DOFs}} \times 1)} = [u_1 \ u_2 \ \dots \ u_N \ v_1 \ v_2 \ \dots \ v_N \ \theta_1 \ \theta_2 \ \dots \ \theta_N]^T,$$

static condensation can readily be applied to eliminate rotational and vertical DOFs to retain only the horizontal DOFs.  $u_i$  are the horizontal DOFs,  $v_i$  are the vertical DOFs,  $\theta_i$  are the rotational DOFs, and  $i = 1, 2, \dots, N$  is the individual DOF number in the respective directions.

The general algorithm for static condensation is the following:

1. Order the DOFs such that the retained and condensed DOFs are arranged together and establish the stiffness matrix in the following format:

$$\begin{bmatrix} \mathbf{K}_{rr} & \mathbf{K}_{rc} \\ \mathbf{K}_{cc} & \mathbf{K}_{cr} \end{bmatrix} \begin{bmatrix} \mathbf{D}_r \\ \mathbf{D}_c \end{bmatrix} = \begin{bmatrix} \mathbf{R}_r \\ \mathbf{R}_c \end{bmatrix},$$

where the subscript  $r$  denotes retained, and the subscript  $c$  denotes condensed.

2. Establish the system of equations:

$$\mathbf{K}_{rr} \mathbf{D}_r + \mathbf{K}_{rc} \mathbf{D}_c = \mathbf{R}_r \quad (3.1)$$

$$\mathbf{K}_{cc} \mathbf{D}_r + \mathbf{K}_{cr} \mathbf{D}_c = \mathbf{R}_c. \quad (3.2)$$

3. Obtain the condensed stiffness matrix  $\bar{\mathbf{K}}$ :

$$\begin{aligned} (\mathbf{K}_{rr} - \mathbf{K}_{rc} \mathbf{K}_{cc}^{-1} \mathbf{K}_{cr}) \mathbf{D}_r &= \mathbf{R}_r - \mathbf{K}_{rc} \mathbf{K}_{cc}^{-1} \mathbf{R}_c \\ \bar{\mathbf{K}} \mathbf{D}_r &= \bar{\mathbf{R}}, \quad \bar{\mathbf{K}} = \mathbf{K}_{rr} - \mathbf{K}_{rc} \mathbf{K}_{cc}^{-1} \mathbf{K}_{cr}, \quad \bar{\mathbf{R}} = \mathbf{R}_r - \mathbf{K}_{rc} \mathbf{K}_{cc}^{-1} \mathbf{R}_c. \end{aligned} \quad (3.3)$$

Cubic shape functions are used to formulate the local consistent mass matrix as:

$$\mathbf{m}_{e(6 \times 6)} = \frac{\rho_e A L_e}{420} \begin{bmatrix} 140 & 0 & 0 & 70 & 0 & 0 \\ 0 & 156 & 22L_e & 0 & 54 & -13L_e \\ 0 & 22L_e & 4L_e^2 & 0 & 13L_e & -3L_e^2 \\ 70 & 0 & 0 & 140 & 0 & 0 \\ 0 & 54 & 13L_e & 0 & 156 & -22L_e \\ 0 & -13L_e & -3L_e^2 & 0 & -22L_e & 4L_e^2 \end{bmatrix},$$

where  $\rho_e$  is the equivalent density which accounts for column mass, beam mass, and static live loads. The global mass matrix is assembled and condensed in the same manner as the global stiffness matrix.

### 3.2 Random vibrations

A random process  $x(t)$  with length  $T$  can be characterized by statistical quantities such as the mean value  $m$  and the variance  $\sigma^2$ . The probability of the random process taking a value within a specified interval  $dx = x_2 - x_1$  at time  $t$  can be expressed as:

$$P(x_1 \leq x(t) \leq x_2) = \int_{x_1}^{x_2} p(x)dx, \quad p(x)dx = \frac{\sum dt}{T}, \quad (3.4)$$

where  $dt$  is an infinitesimal time increment,  $p(x)dx$  is the time fraction where the process  $x(t)$  is in the interval  $x_1$  to  $x_2$ , and  $p(x)$  is the probability density function. The mean value  $m$  and variance  $\sigma^2$  are defined as:

$$m = E[x(t)] = \int_t x(t)dt, \quad \sigma^2 = E[(x(t) - m)^2] = \int_t (x - m)p(x)dt.$$

**Equation 3.4** is mathematically correct only if the length  $T$  of the random process  $x(t)$  is infinite. However, if it is assumed that the statistical properties of the random process can be represented by the time history  $x(t)$  with a finite length  $T$ , then the finite time history  $x(t)$  can be used to calculate the properties of the random signal  $x(t)$  with infinite length. A random process whose statistical properties does not change with absolute time, is called a stationary process.

If a random process is recorded infinitely many times, the ensemble of recordings will together represent the random process completely. If each of the random signals in the ensemble are stationary and the statistical properties measured across the ensemble are stationary with respect to time as well, then the process is called ergodic.

The autocorrelation functions  $R_{xx}(\tau)$  and  $R_{yy}(\tau)$  for the random processes  $x(t)$  and  $y(t)$ , and the cross-correlation functions  $R_{xy}(\tau)$  and  $R_{yx}(\tau)$  are defined as:

$$\begin{aligned} R_{xx}(\tau) &= E[x(t)x(t + \tau)], & R_{xy}(\tau) &= E[x(t - \tau)y(t)] \\ R_{yx}(\tau) &= E[y(t - \tau)x(t)], & R_{yy}(\tau) &= E[y(t)y(t + \tau)] \end{aligned}$$

$$\mathbf{R}_{xy}(\tau) = \begin{bmatrix} R_{xx}(\tau) & R_{xy}(\tau) \\ R_{yx}(\tau) & R_{yy}(\tau) \end{bmatrix}, \quad (3.5)$$

where  $\tau$  is a time-shift. If the processes are stationary, then the cross-correlation functions  $R_{xy}(\tau)$  and  $R_{yx}(\tau)$  are the same, and the autocorrelation function and cross-correlation functions are only functions of the time-shift  $\tau$ .

The correlation coefficient  $\rho_{xy}$  of the random processes  $x(t)$  and  $y(t)$  is defined as:

$$\rho_{xy} = \frac{E[(x - m_x)(y - m_y)]}{\sigma_x \sigma_y}.$$

If the correlation coefficient  $\rho_{xy}$  between the two random processes  $x(t)$  and  $y(t)$  is zero, there is no correlation between the two random processes. If the correlation coefficient  $\rho_{xy}$  between the

two random processes  $x(t)$  and  $y(t)$  is  $\pm 1$ , there is perfect correlation between the two random processes. If the random processes  $x(t)$  and  $y(t)$  are stationary such that they are independent of time, then:

$$\rho_{xx} = \frac{R_x(\tau) - m_x^2}{\sigma_x^2}.$$

The Fourier transform of  $x(t)$  in complex form can be expressed as:

$$X(\omega) = \frac{1}{2\pi} \int_{-\infty}^{\infty} x(t)e^{-i\omega t} dt, \quad (3.6)$$

where  $e^{-i\omega t} = e^{i\theta} = \cos \theta + i \sin \theta$  is Euler's formula,  $\omega = 2\pi f$  is the angular frequency, and  $f$  is the frequency. By taking the Fourier transform of the cross-correlation matrix  $\mathbf{R}_{xy}(\tau)$  in **Equation 3.5**, the cross-spectral density matrix  $\mathbf{S}_{xy}(\omega)$  can be obtained:

$$\mathbf{S}_{xy}(\omega) = \frac{1}{2\pi} \int_{-\infty}^{\infty} \mathbf{R}_{xy}(\tau)e^{-i\omega\tau} d\tau = \begin{bmatrix} S_{xx}(\omega) & S_{xy}(\omega) \\ S_{yx}(\omega) & S_{yy}(\omega) \end{bmatrix}, \quad (3.7a)$$

$$\mathbf{R}_{xy}(\tau) = \int_{-\infty}^{\infty} \mathbf{S}_{xy}(\omega)e^{i\omega\tau} d\omega = \begin{bmatrix} R_{xx}(\tau) & R_{xy}(\tau) \\ R_{yx}(\tau) & R_{yy}(\tau) \end{bmatrix}. \quad (3.7b)$$

The equation pair in **Equation 3.7** are known as the Wiener-Khinchin theorem. **Equation 3.7a** describes the power distribution of the process at each frequency  $\omega$ . The random process can be considered as narrow-banded if the power distribution is concentrated around one single peak. **Equation 3.7b** shows the autocorrelation function  $\mathbf{R}_{xy}(\tau)$  in terms of the inverse Fourier transform of the cross-spectral density  $\mathbf{S}_{xy}(\omega)$ . The inverse Fourier transform of  $X(\omega)$  can be expressed as:

$$x(t) = \int_{-\infty}^{\infty} X(\omega)e^{i\omega t} d\omega.$$

If the time-shift in the autocorrelation function  $R_{xx}(\tau)$  is zero, then the inverse Fourier transform of the auto-spectral density  $S_x(\omega)$  becomes the variance for a zero-mean process:

$$R_{xx}(\tau = 0) = \int_{-\infty}^{\infty} S_x(\omega)d\omega = E[x^2(t)] = \sigma_x^2. \quad (3.8)$$

### 3.3 Wind characteristics

Wind is a natural phenomenon which occur due to pressure differences in the atmosphere caused by the energy influx from the sun. The behavior of wind can be characterized by its vertical distance from a horizontal surface, where only the lowermost part closest to the Earth's surface is relevant to structural engineering. This lowermost part is called the atmospheric boundary layer (ABL). The winds in the atmospheric boundary layer are affected by the surface roughness, surface shape or terrain, and distance to the surface.

In the atmospheric boundary layer, wind can be characterized by a mean wind velocity component and a turbulent component, both as functions of distance to the surface. In the lowermost part of the atmospheric boundary layer, the wind velocity is dominated by turbulence. For turbulence, an important length scale is the surface roughness. In the uppermost part of the atmospheric boundary

layer, the wind velocity is less affected by turbulence. In the uppermost part, an important length scale is the distance to the surface.

The mean wind velocity  $v_m(z)$  is often described either by a logarithmic law or an empirical power law. In the Eurocodes (NS-EN 1991-1-4:2005 Section 4.3), the following logarithmic law is adopted:

$$\frac{v_m(z)}{v_b} = k_r \ln\left(\frac{z}{z_0}\right), \quad z_{\min} \leq z \leq z_{\max}, \quad (3.9)$$

where  $v_b = u_*$  is the friction velocity or the basic wind velocity,  $k_r$  is a terrain factor,  $z$  is the distance to the surface or elevation, and  $z_0$  is the roughness length. The roughness length can be interpreted as the size of a characteristic vortex caused by fluid-surface shear stresses (Dyrbye & Hansen, 1997). From **Equation 3.9**, observe that the mean wind velocity is zero when the elevation  $z$  is equal to the roughness length  $z_0$ . The derivation of **Equation 3.9** can be viewed in Simiu and Yeo (2019).

Wind turbulence can be considered as a random or stochastic process which can only be described by statistical means. It is common to assume that turbulence is a stationary process within the averaging time or observation period. The averaging time is often 10 minutes, such as in the Eurocodes (NS-EN 1991-1-4:2005 Section 4.2), but other averaging times are also used, such as 3 seconds in the American ASCE standard (Simiu & Yeo, 2019). The effect of the averaging time was initially described by Van der Hoven (1957), who generated a power spectral density curve for wind velocities spanning periods from 4 seconds to 60 days. A reproduction of the Van der Hoven spectrum from his initial paper is shown in **Figure 1**.

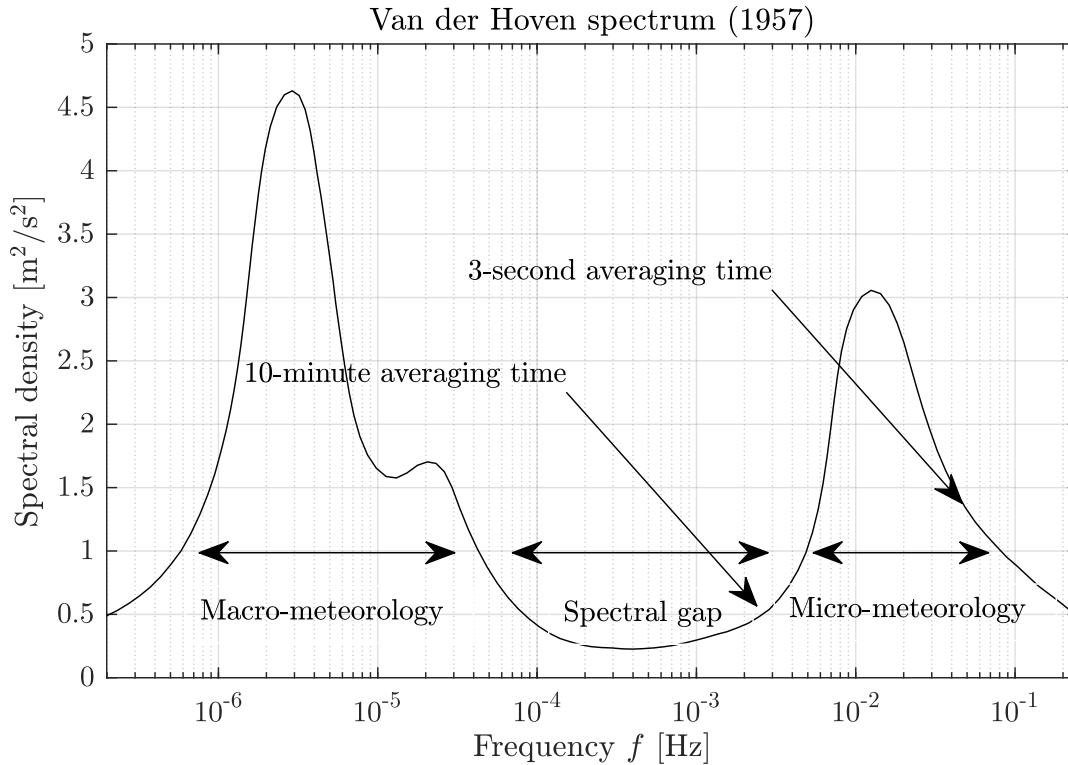


Figure 1 A reproduction of the horizontal wind velocity spectrum at Brookhaven National Library at about 100 m height (Van der Hoven, 1957).

In **Figure 1**, macro-meteorology describes larger weather patterns with a period of some days. The highest peak around the period of 100 hours denotes the power content in the larger weather patterns. Between the periods of 10 minutes and a few hours, there is a spectral gap with almost zero power. The next peak with a period of about 1 minute denotes the power content of micro-meteorology with high-frequency content. A more detailed description of **Figure 1** can be found in Van der Hoven (1957). In wind engineering, it is often micro-meteorology that is of interest. In micro-meteorology, high frequency turbulent winds take precedence over slower low frequency fluctuations. Observe that a 3-second averaging time results in a higher power content in the wind. Thus, the use of the equations and values in different wind standards cannot be used interchangeably due to the different averaging time calibrations.

### 3.4 The gust factor approach

Common practice in structural engineering is to perform spectral analysis of turbulent wind velocities with an averaging period of 10 minutes. Through aerodynamic admittance functions and mechanical admittance functions, the spectral density of the response can be obtained. The aerodynamic admittance of a structure describes the ability of a structure to capture the wind pressure, whereas the mechanical admittance of a structure describes the dynamic behavior of a structure. From the spectral analysis of the response, the variance of relevant response parameters can be found from **Equation 3.8**. By multiplying the standard deviation of the relevant response parameter with a peak response factor, the peak response can be obtained. This approach is called the gust factor approach and was first proposed by Davenport (1961a). The gust factor approach is the method used in the Eurocodes and is derived in the following sections.

#### 3.4.1 Bluff body aerodynamics

Consider an object with an area  $A$  and drag coefficient  $C_D(R_e)$  moving through a fluid with density  $\rho_a$  and velocity  $u(t)$ , then the drag force  $F(t)$  on the object can be expressed as:

$$F(t) = \frac{1}{2} \rho_a A u^2(t) C_D(R_e), \quad (3.10)$$

where  $R_e$  is Reynolds number, and  $t$  is the time. It can be assumed that the drag coefficient  $C_D$  is constant if the fluid is of turbulent character and the object has sharp corners (Delany & Sorensen, 1953). This is a reasonable assumption for most buildings in structural engineering.

In **Section 3.3**, wind is described as fluid which could be decomposed into a mean wind velocity component  $\bar{u}(t)$  and a turbulent component  $\hat{u}(t)$ :

$$u(t) = \bar{u} + \hat{u}(t). \quad (3.11)$$

By substituting **Equation 3.11** into **Equation 3.10** and expanding the squared term, the following expression is obtained:

$$F(t) = \frac{1}{2} \rho_a A C_D [\bar{u}^2 + 2\bar{u}\hat{u}(t) + \hat{u}(t)^2],$$

where the turbulent component  $\hat{u}(t)$  is a random process and the mean component  $\bar{u}$  is a constant. When considering the dynamic response, it is only the dynamic or turbulent component  $\hat{F}(t)$  which is of interest:

$$\hat{F}(t) = \frac{1}{2} \rho_a A C_D [2\bar{u}\hat{u}(t) + \hat{u}(t)^2].$$

By neglecting the second order term, the following linear approximation to the turbulent drag force is obtained:

$$\hat{F}(t) = \rho_a AC_D \bar{u} \hat{u}(t). \quad (3.12)$$

The spectral density of the turbulent force  $S_{\hat{F}}(\omega)$  can be obtained by taking the Fourier transform of the autocorrelation function  $R_{\hat{F}}(\tau)$  in **Equation 3.5** by using **Equation 3.7**:

$$S_{\hat{F}}(\omega) = \frac{1}{2\pi} \int_{-\infty}^{\infty} R_{\hat{F}}(\tau) e^{-i\omega\tau} d\tau = \frac{1}{2\pi} \int_{-\infty}^{\infty} E[\hat{F}(t) \cdot \hat{F}(t + \tau)] e^{-i\omega\tau} d\tau. \quad (3.13)$$

By substituting **Equation 3.12** into **Equation 3.13**, the following expression is obtained:

$$\begin{aligned} S_{\hat{F}}(\omega) &= \frac{1}{2\pi} \int_{-\infty}^{\infty} (\rho_a AC_D \bar{u})^2 E[\hat{u}(t) \cdot \hat{u}(t + \tau)] e^{-i\omega\tau} d\tau \\ \Rightarrow S_{\hat{F}}(\omega) &= (\rho_a AC_D \bar{u})^2 \frac{1}{2\pi} \int_{-\infty}^{\infty} R_{\hat{u}}(\tau) e^{-i\omega\tau} d\tau = (\rho_a AC_D \bar{u})^2 S_{\hat{u}}(\omega). \end{aligned} \quad (3.14)$$

By substituting the static component  $\bar{F} = \frac{1}{2} \rho AC_D \bar{u}^2$  into **Equation 3.14**, the spectral density of the turbulent force<sup>2</sup>  $S_{\hat{F}}(\omega)$  can be expressed as:

$$S_{\hat{F}}(\omega) = \frac{4\bar{F}^2}{\bar{u}^2} S_u(\omega). \quad (3.15)$$

### 3.4.2 Aerodynamic admittance functions

**Equation 3.15** expresses the force spectrum on an object if the object is smaller than some characteristic length of a wind gust or vortex  $L_u$ . However, when the characteristic length of a wind gust  $L_u$  is smaller than a characteristic length of the object, the wind pressure is not perfectly correlated over the entire surface. Thus, when the correlation coefficient is smaller than unity  $\rho < 1$ , it becomes apparent that the object is unable to capture all the gusts. To account for the lack of correlation, an aerodynamic admittance function  $\chi^2$  is introduced to **Equation 3.15**:

$$S_{\hat{F}}(\omega) = \frac{4\bar{F}^2}{\bar{u}^2} S_u(\omega) \chi^2(\omega). \quad (3.16)$$

An aerodynamic admittance function  $\chi^2$  should be a function of a characteristic length of the object  $\sqrt{A}$ , and a wind gust length  $L_u = \bar{u}/f$ . Since the wind gust length is a function of the mean wind velocity  $\bar{u}$  and the frequency  $f$ , the aerodynamic admittance function  $\chi^2$  becomes:

$$\chi^2 = \chi^2(\sqrt{A}, \bar{u}, f). \quad (3.17)$$

Several aerodynamic admittance functions have been proposed (van Oosterhout, 1996). Some of the most common aerodynamic admittance functions are shown in **Table 1**.

---

<sup>2</sup> For the remainder of this thesis, the turbulent parts will be denoted without hats ( $x, \ddot{x}, u, \ddot{u}, F$ ).

<b>Vickery</b>	$\chi(f, \bar{u}, \sqrt{A}) = \frac{1}{1 + \left(\frac{2f\sqrt{A}}{\bar{u}}\right)^{\frac{4}{3}}}$
<b>Eurocodes</b>	$\chi^2(f, \bar{u}, \sqrt{A}) = R_h(\eta_h)R_b(\eta_b)$
<b>Generalized wind load</b>	$\chi_{\phi_i}^2(f, \bar{u}, \sqrt{A}) = \frac{1}{A^2} \int_A \int_A \frac{\bar{u}_{m,k} \bar{u}_{m,l}}{\bar{u}_{m,z_s}^2} \phi_i(y_k, z_k) \phi_i(y_l, z_l) \text{coh}_{v_k v_l} dy_k dy_l dz_k dz_l$

Table 1 Common aerodynamic admittance functions. In this thesis, the aerodynamic admittance function used in the Eurocodes and the generalized wind load is used.

### 3.4.3 Mechanical admittance function

Consider a single degree of freedom system (SDOF) consisting of a mass  $m$  attached to a spring with stiffness  $k$ , a damper with damping coefficient  $c$ , and an external force  $p(t)$ . Then, the equation of motion can be formulated as:

$$m\ddot{x}(t) + c\dot{x}(t) + kx(t) = p(t), \quad (3.17)$$

where  $\ddot{x}(t)$  is the acceleration response,  $\dot{x}(t)$  is the velocity response, and  $x(t)$  is the displacement response. If a Fourier transform is applied to both sides of **Equation 3.17**, the following equation is obtained:

$$\begin{aligned} \mathcal{F}(m\ddot{x}(t) + c\dot{x}(t) + kx(t))(\omega) &= \mathcal{F}(p(t))(\omega) \\ m\ddot{X}(\omega) + c\dot{X}(\omega) + kX(\omega) &= P(\omega). \end{aligned} \quad (3.18)$$

The Fourier transform of the acceleration  $\ddot{x}(t)$ , velocity  $\dot{x}(t)$ , and displacement  $x(t)$  can be expressed as:

$$\begin{aligned} x(t) &= \int_{-\infty}^{\infty} X(\omega) e^{i\omega t} d\omega \therefore \mathcal{F}(x(t))(\omega) = X(\omega), \\ \dot{x}(t) &= \frac{d}{dt} \int_{-\infty}^{\infty} X(\omega) e^{i\omega t} d\omega = i\omega x(t) \therefore \dot{X}(\omega) = i\omega X(\omega), \\ \ddot{x}(t) &= \frac{d^2}{dt^2} \int_{-\infty}^{\infty} X(\omega) e^{i\omega t} d\omega = -\omega^2 x(t) \therefore \ddot{X}(\omega) = -\omega^2 X(\omega). \end{aligned}$$

By substituting these expressions into **Equation 3.18** and rearranging, the mechanical admittance function can be expressed as:

$$H(\omega) = \frac{X(\omega)}{P(\omega)} = \frac{1}{-\omega^2 m + i\omega c + k} = \frac{1}{k} \frac{1}{\left[1 - \left(\frac{\omega}{\omega_n}\right)^2\right] + i \left[2\xi \left(\frac{\omega}{\omega_n}\right)\right]} \quad (3.19)$$

where  $\omega$  is the angular excitation frequency,  $c = \xi m \omega_n / 2$  is the damping coefficient,  $\omega_n$  is the natural angular frequency, and  $\xi = c / 2m \omega_n$  is the damping ratio. The mechanical admittance function is often called the frequency response function. The absolute value of the frequency response function in **Equation 3.19** can be expressed as:



$$\frac{|H(\omega)|}{(x_{st})_0} = \frac{1}{\sqrt{\left[1 - \left(\frac{\omega}{\omega_n}\right)^2\right]^2 + \left[2\xi\left(\frac{\omega}{\omega_n}\right)\right]^2}}, \quad (3.20)$$

where  $(x_{st})_0 \equiv p_0/k = 1/k$  is the static displacement of a unit force.

**Equation 3.20** can now be used to express the displacement response in the frequency domain as:

$$X(\omega) = H(\omega)P(\omega), \quad (3.21)$$

where  $P(\omega)$  is the Fourier transform of the external force.

### 3.4.4 Wind spectrum

The spectral density for a given time series can be found by using **Equation 3.7**. If there are wind series measurements available, a specific spectrum can be found by using this methodology. However, in many cases, a wind series is not readily available and not practical to obtain. Thus, Kaimal, Wyngaard, Izumi, and Coté (1972) formulated a spectral density for wind velocities based on wind data. In NS-EN 1991-1-4:2005, the following modified Kaimal spectrum (Solari, 1993a) is used:

$$S_u^n(z, f) = \frac{f \cdot S_u(z, f)}{\sigma_u^2} = \frac{6.8 f_L(z, f)}{(1 + 10.2 f_L(z, f))^{\frac{5}{3}}}, \quad f_L(z, f) = \frac{f \cdot L_u(z)}{\bar{u}(z)}, \quad (3.22)$$

where  $S_u^n(z, f)$  is the normalized spectral density,  $S_u(z, f)$  is the one-sided spectral density,  $f_L(z, f)$  is a non-dimensional frequency, and  $L_u(z)$  is a turbulent length scale.

### 3.4.5 Response spectrum

The response spectrum can be obtained in the same manner as in **Section 3.4.1**, where results from **Section 3.4.2** and **Section 3.4.3** are used. By taking the Fourier transform of the autocorrelation function  $R_{xx}(\tau) = E[x(t)x(t + \tau)]$ , the following expression is obtained:

$$S_{xx}(\omega) = \frac{1}{2\pi} \int_{-\infty}^{\infty} R_{xx}(\tau) e^{-i\omega\tau} d\tau = H^*(\omega) S_{PP}(\omega) H(\omega) = |H(\omega)|^2 S_{PP}(\omega), \quad (3.23)$$

where  $S_{PP}(\omega)$  is the force spectrum in **Equation 3.16**. The asterisk superscript \* denotes the complex conjugate. By substituting **Equation 3.16** into **Equation 3.23**, the response spectrum  $S_{xx}(\omega)$  for an SDOF system can be expressed as:

$$S_{xx}(\omega) = \frac{4\bar{F}^2}{\bar{u}^2} |H(\omega)|^2 S_u(\omega) \chi^2(\omega). \quad (3.24)$$

For an external force which amplitude is unity, the response spectrum  $S_{xx}(\omega)$  in **Equation 3.24** becomes:

$$S_{xx}(\omega) = \frac{4\bar{F}^2}{k^2 \bar{u}^2} |H(\omega)|^2 S_u(\omega) \chi^2(\omega). \quad (3.25)$$

For an MDOF system, **Equation 3.24** becomes:

$$S_{xx}(\omega) = \frac{4\bar{F}^2}{\bar{u}^2} \mathbf{H}(\omega) \mathbf{S}_{uu}(\omega) \mathbf{H}^H(\omega) \boldsymbol{\chi}^T(\omega) \boldsymbol{\chi}(\omega),$$

where  $\mathbf{H}^H(\omega)$  is the Hermitian transpose. A Hermitian transpose is the complex conjugate transpose of a matrix.

### 3.4.6 Resonant and background response

In **Section 3.2**, the variance of a random process was derived in **Equation 3.8** from a spectral density. By applying the result to the spectral density of the displacement response in **Equation 3.24**, the variance of the displacement response can be expressed as:

$$\sigma_x^2 = \int_{-\infty}^{\infty} S_{xx}(\omega) d\omega. \quad (3.26)$$

Since the angular frequency can only take positive values, the spectrum is one-sided. Thus, the integration will go from zero to positive infinity:

$$\sigma_x^2 = \int_0^{\infty} S_{xx}(\omega) d\omega = \frac{4\bar{F}^2}{k^2\bar{u}^2} \int_0^{\infty} |H(\omega)|^2 S_{uu}(\omega) \chi^2(\omega) d\omega. \quad (3.27)$$

If the static displacement response  $\bar{x} = \bar{F}/k$  and a normalized spectrum  $S_{uu}^n(\omega) = S_{uu}(\omega)/\sigma_u^2$  is substituted into **Equation 3.27**, then the following dimensionless relationship is obtained:

$$\frac{\sigma_x^2}{\sigma_u^2} = 4 \frac{\bar{x}^2}{\bar{u}^2} \int_0^{\infty} |H(\omega)|^2 S_{uu}^n(\omega) \chi^2(\omega) d\omega. \quad (3.28)$$

The integral in **Equation 3.28** can be approximated as a two-component integral consisting of a static and a dynamic component or a background and resonant response if the response is considered as a narrow-banded process. If the response is indeed narrow-banded, **Equation 3.28** can be approximated by:

$$\frac{\sigma_x^2}{\sigma_u^2} = 4 \frac{\bar{x}^2}{\bar{u}^2} [A_B + A_R], \quad (3.29)$$

$$A_B \approx \int_0^{\infty} S_{uu}^n(\omega) \chi^2(\omega) d\omega \quad (3.30)$$

$$A_R \approx \chi^2(\omega_n) S_{uu}^n(\omega_n) \int_0^{\infty} |H(\omega)|^2 d\omega \quad (3.31)$$

where  $A_B$  is the background response, and  $A_R$  is the resonant response. In the background response  $A_B$  in **Equation 3.30**, the mechanical admittance is assumed to be unity. In the resonant response  $A_R$ , the aerodynamic admittance  $\chi(\omega)$  and normalized wind velocity spectrum  $S_{uu}^n(\omega)$  is assumed to take the value at the natural angular frequency  $\omega_n$  of the system.

The analytical solution to the integral of the squared mechanical admittance  $|H(\omega)|^2$  in **Equation 3.31** is:

$$\int_0^{\infty} |H(\omega)|^2 d\omega = \frac{\pi \omega_n}{4 \xi}. \quad (3.32)$$

By substituting the result in **Equation 3.32** into **Equation 3.31**, the resonant response can be expressed as:

$$A_R \approx R^2 = \frac{\pi \omega_n}{4 \xi} \chi^2(\omega_n) S_{uu}^n(\omega_n) = \frac{\pi^2 \omega_n S_{uu}(\omega_n)}{2\delta \sigma_u^2} \chi^2(\omega_n), \quad (3.33)$$

where the latter expression is how the resonant response  $A_R$  is expressed in NS-EN 1991-1-4:2005 Annex B. In **Equation 3.33**,  $\delta = 2\pi\xi$  is the logarithmic decrement and  $\xi$  is the damping ratio.

If the results from **Equation 3.30** and **Equation 2.33** are substituted into **Equation 3.29** and rearranged, the following expression for the dimensionless response can be written as:

$$\frac{\sigma_x^2}{\bar{x}^2} = 4 \frac{\sigma_u^2}{\bar{u}^2} [A_B + A_R] = 4 \frac{\sigma_u^2}{\bar{u}^2} \left[ \int_0^\infty \frac{S_{uu}(\omega)}{\sigma_u^2} \chi^2(\omega) d\omega + \frac{\pi^2 \omega_n S_{uu}(\omega_n)}{2\delta \sigma_u^2} \chi^2(\omega_n) \right]. \quad (3.34)$$

**Equation 3.34** is the original expression formulated by Davenport (1961a). For winds characterized by high intensity turbulence, the contribution from the second order term that was neglected in **Equation 3.11** becomes non-negligible. Thus, the following correction to **Equation 3.34** was introduced by Vickery (1972) for the background response:

$$A_B \approx (1 + k)^2 \int_0^\infty S_{uu}^n(\omega) \chi^2(\omega) d\omega, \quad k = \frac{gr\sqrt{A_B}}{4}. \quad (3.35)$$

By substituting the modified Kaimal spectrum in **Equation 3.22** into **Equation 3.30**, the background response  $A_B$  can be expressed as (Solari, 1993a):

$$A_B \approx B^2 = \frac{1}{1 + 0.9 \left( \frac{b+h}{L_u(z_s)} \right)^{0.63}}, \quad (3.36)$$

where  $b$  is the windward width of the object,  $h$  is the height of the object, and  $L(z_s)$  is the turbulent length scale at reference height  $z_s = 0.6h \geq z_{min}$  for a vertical object.

The resonant response  $R^2$  in **Equation 3.33** and the background response  $B^2$  in **Equation 3.36** are the expressions used in NS-EN 1991-1-4:2005 Annex B.

### 3.4.7 Peak response

The peak displacement response  $x_p$  may be approximated by:

$$x_p = \bar{x} + k_p \sigma_x, \quad (3.37)$$

where  $k_p$  is a peak response factor. By rearranging **Equation 3.37**, the gust factor  $G$  derived by Davenport (1961a) is formulated as:

$$\frac{x_p}{\bar{x}} = 1 + k_p \frac{\sigma_x}{\bar{x}} = G \therefore G = 1 + 2k_p \frac{\sigma_u}{\bar{u}} \sqrt{B^2 + R^2}, \quad (3.38)$$

where the peak response factor  $k_p$  is derived as:

$$k_p = \sqrt{2 \ln(\nu T)} + \frac{0.6}{\sqrt{2 \ln(\nu T)}} \approx \sqrt{1.175 + 2 \ln(\nu T)}. \quad (3.39)$$

In **Equation 2.39**,  $\nu$  is the zero up-crossing frequency, and  $T$  is the observation period. The derivation of the zero up-crossing frequency  $\nu$  can be found in Newland (1993), and can be expressed as:

$$v = \frac{1}{2\pi} \frac{\sigma_{\dot{x}}}{\sigma_x}, \quad (3.40)$$

where  $\sigma_{\dot{x}}$  is the standard deviation of the velocity response. By differentiating the response spectrum  $S_{xx}(\omega)$  in **Equation 3.23** with respect to the angular frequency  $\omega$ , the variance of the velocity response becomes:

$$\sigma_{\dot{x}}^2 = \int_0^\infty S_{\dot{x}\dot{x}}(\omega) d\omega = \int_0^\infty \frac{d}{d\omega} S_{xx}(\omega) d\omega = \int_0^\infty \omega^2 S_{xx}(\omega) d\omega. \quad (3.41)$$

By substituting **Equation 3.41** and **Equation 3.26** into **Equation 3.40**, and using the modified Kaimal spectrum in **Equation 3.22**, the zero up-crossing frequency  $v$  can be approximated by (Solari, 1993b):

$$v = f_1 \sqrt{\frac{R^2}{B^2 + R^2}}, \quad (3.42)$$

where  $f_1$  is the first natural frequency of the object.

### 3.4.8 Structural factor

The peak wind load on an object can be expressed as:

$$F_p = c_s c_d \cdot c_f q_p A_{\text{ref}} = p_p \cdot c_f A_{\text{ref}}, \quad p_p = c_s c_d \cdot c_f q_p \quad (3.43)$$

where  $c_s c_d$  is the structural factor,  $c_f$  is a force coefficient,  $q_p$  is the peak velocity pressure,  $A_{\text{ref}}$  is a reference area, and  $p_p$  is the equivalent static wind pressure. In this section, the structural factor is derived for a rectangular plan object.

The peak velocity pressure can be expressed as:

$$q_p = \frac{1}{2} \rho_a u_p^2, \quad (3.44)$$

where  $u_p$  is the peak wind velocity (Solari, 1993a):

$$u_p = \left(1 + 2k_v \frac{\sigma_u}{\bar{u}} \sqrt{P_0}\right) \bar{u} = c_e \bar{u} \quad (3.45)$$

In **Equation 3.45**,  $c_e$  is the exposure factor,  $k_v$  is the peak velocity factor which is a function of  $P_0$ , and  $P_0$  is a non-dimensional quantity dependent on the non-dimensional frequency  $f_L$  in **Equation 3.22** (Solari & Kareem, 1998). The peak velocity factor  $k_v$  can be expressed as:

$$k_v = \sqrt{1.175 + 2 \ln \left[ T_L \sqrt{\frac{P_1}{P_0}} \right]}, \quad T_L = \frac{T \cdot L_u(z)}{\bar{u}(z)}, \quad (3.46)$$

where  $T_L$  is the dimensionless averaging time,  $T$  is the averaging time, and  $P_1$  and  $P_0$  are defined as:

$$P_0 = \frac{1}{1 + 0.56 f_L^{-0.74}}, \quad \frac{P_1}{P_0} = \frac{1}{31.25 f_L^{-1.44}}.$$

The structural factor  $c_s c_d$  can be factorized into a size component  $c_s$  and a dynamic component  $c_d$ . The size component  $c_s$  reduces the load due to the lack of coherence of wind pressures on a surface caused by turbulence and can be regarded as a rigid or static component. The dynamic or flexible component  $c_d$  increases the load due to resonance between the structure and the turbulence.

The size factor  $c_s$  is the ratio between the background response in **Equation 3.38** and the exposure factor  $c_e$  in **Equation 3.45**:

$$c_s = \frac{1 + 2k_p \frac{\sigma_u}{\bar{u}} \sqrt{B^2}}{1 + 2k_v \frac{\sigma_u}{\bar{u}} \sqrt{P_0}}, \quad (3.47)$$

where  $P_0$  is a nondimensional parameter. The dynamic factor  $c_d$  is the ratio between the gust factor  $G$  with and without the resonant component:

$$c_d = \frac{1 + 2k_p \frac{\sigma_u}{\bar{u}} \sqrt{B^2 + R^2}}{1 + 2k_p \frac{\sigma_u}{\bar{u}} \sqrt{B^2}}. \quad (3.48)$$

Thus, the structural factor becomes:

$$c_s c_d = \frac{1 + 2k_p \frac{\sigma_u}{\bar{u}} \sqrt{B^2 + R^2}}{1 + 2k_v \frac{\sigma_u}{\bar{u}} \sqrt{P_0}}, \quad (3.49)$$

The recommended values of the peak response factor  $k_p$  is 3.5, the peak velocity factor  $k_v$  is 4.1, and the nondimensional parameter  $P_0$  is 0.723 (Solari & Kareem, 1998). By using these values, the factorized structural factor  $c_s c_d$  in **Equation 3.49** is consistent with NS-EN 1991-1-4:2005 Section 6. The factorized structural factor  $c_s c_d$  can thus be expressed as:

$$c_s = \frac{1 + 7 \frac{\sigma_u}{\bar{u}} \sqrt{B^2}}{1 + 7 \frac{\sigma_u}{\bar{u}}}, \quad c_d = \frac{1 + 2k_p \frac{\sigma_u}{\bar{u}} \sqrt{B^2 + R^2}}{1 + 7 \frac{\sigma_u}{\bar{u}} \sqrt{B^2}}. \quad (3.50)$$

### 3.5 Generalized wind load

#### 3.5.1 Modal analysis

The equation of motion for an SDOF system in **Equation 2.16** can readily be expanded to an MDOF system:

$$\mathbf{m}\ddot{\mathbf{x}}(A, t) + \mathbf{c}\dot{\mathbf{x}}(A, t) + \mathbf{k}\mathbf{x}(A, t) = \mathbf{p}(A, t), \quad (3.51)$$

where  $A$  is spatial coordinate. By assuming that the response displacement  $\mathbf{x}(z, t)$  can be factorized into a time-dependent part  $\boldsymbol{\eta}(t)$  and a spatially dependent part  $\boldsymbol{\phi}(A)$ , **Equation 3.51** can be reformulated as:

$$\mathbf{M}\ddot{\boldsymbol{\eta}}(t) + \mathbf{C}\dot{\boldsymbol{\eta}}(t) + \mathbf{K}\boldsymbol{\eta}(t) = \mathbf{F}(t), \quad (3.52)$$

where  $\mathbf{M}$  is the modal mass,  $\mathbf{C}$  is the modal damping,  $\mathbf{K}$  is the modal stiffness, and  $\mathbf{F}$  is the modal force:

$$\mathbf{M} = \boldsymbol{\phi}^T \mathbf{m} \boldsymbol{\phi}, \quad \mathbf{C} = \boldsymbol{\phi}^T \mathbf{c} \boldsymbol{\phi}, \quad \mathbf{K} = \boldsymbol{\phi}^T \mathbf{k} \boldsymbol{\phi}, \quad \mathbf{F}(t) = \int_A \boldsymbol{\phi}^T \mathbf{p}(A, t) dA.$$

By assuming a solution of the form  $\mathbf{x}(t) = \mathbf{A}e^{\lambda t}$  in **Equation 3.52**, where  $\mathbf{A}$  is a vector of constants and  $\lambda$  is a scalar, the following eigenvalue problem can be formulated:

$$(\mathbf{m}\lambda^2 + \mathbf{c}\lambda + \mathbf{k})\boldsymbol{\phi}(A)\boldsymbol{\eta}(t) = \mathbf{0}. \quad (3.53)$$

For lightly damped systems with a damping ratio  $\xi = c/2m\omega_n$  of less than 20%, the damping term can be neglected in the eigenvalue problem. Thus, by assuming a harmonic solution, the eigenvalue problem becomes:

$$(\mathbf{k} - \lambda\mathbf{m})\boldsymbol{\phi}(A)\boldsymbol{\eta}(t) = \mathbf{0}, \quad (3.54)$$

where  $\lambda = \omega_n^2$  is the angular natural frequency squared.  $\boldsymbol{\phi}(A)$  is the modal matrix containing all the modal shapes.

### 3.5.2 Fluctuating wind force spectrum

The cross-spectral density of the fluctuating modal force can be evaluated as in **Section 3.4.1**. The force component  $p(t)$  per unit area in **Equation 3.12** and **Equation 3.10** can be expressed as **Equation 2.55** for an arbitrary spatial coordinate  $k$ :

$$p_k = \rho_a C_{D,k} \bar{u}_k u_k(t), \quad (3.55a)$$

$$\bar{p}_k = \frac{1}{2} \rho_a C_{D,k} \bar{u}_k^2. \quad (3.55b)$$

By substituting **Equation 3.55** into the modal force  $F_k(t)$ , the following expression can be obtained:

$$F_k(t) = \int_A \boldsymbol{\phi}_k(A) \rho_a C_{D,k} \bar{u}_k u_k(t) dA_k, \quad (3.56a)$$

$$\bar{F}_k = \int_h \int_b \frac{1}{2} \rho C_D \bar{u}^2 \boldsymbol{\phi}_k dy dz = \frac{1}{2} \rho C_{D,r} \bar{u}_r^2 A \frac{1}{A} \int_h \int_b \frac{C_D}{C_{D,r}} \left( \frac{\bar{u}}{\bar{u}_r} \right)^2 \boldsymbol{\phi}_k dy dz = \frac{1}{2} \rho C_{D,r} \bar{u}_r^2 A \bar{J}, \quad (3.56b)$$

where the last double integral in **Equation 3.56b** can be defined as the mean aerodynamic transfer  $\bar{J}$ .

The cross-spectral density of the modal force for two different spatial coordinates  $S_{F_k F_l}(\omega)$  can be expressed as:

$$S_{F_k F_l}(\omega) = \rho_a^2 \int_A \int_A \boldsymbol{\phi}_k \boldsymbol{\phi}_l C_{D,k} C_{D,l} \bar{u}_k \bar{u}_l S_{u_k u_l}(\omega) dA_k dA_l, \quad (3.57)$$

where the cross-spectral density of the fluctuating wind  $S_{u_k u_l}(\omega)$  can be expressed as:

$$S_{u_k u_l}(\omega) = coh_{u_k u_l} \sqrt{S_{u_k}(\omega) S_{u_l}(\omega)}. \quad (3.58)$$

$S_{u_k}(\omega)$  is the one-sided spectral density in **Equation 3.22** and  $coh_{u_k u_l}$  is a coherence function. A widely used coherence function  $coh_{u_k u_l}$  is of exponential form and was proposed by Davenport (1961a):

$$coh_{u_k u_l} = e^{-\frac{2f}{\bar{u}_k + \bar{u}_l} \sqrt{C_z^2(z_k - z_l) + C_y^2(y_k - y_l)}}, \quad (3.59)$$

where  $C_z$  is a vertical decay coefficient,  $C_y$  is a horizontal decay coefficient, and  $z_k$  and  $y_k$  are spatial coordinates for a plane surface perpendicular to the wind direction  $x_k$ . By substituting the cross-spectral density  $S_{u_k u_l}(\omega)$  in **Equation 3.58** into the cross-spectral density of the modal force  $S_{F_k F_l}(\omega)$  in **Equation 3.57**, the following expression can be obtained:

$$S_{F_k F_l}(\omega) = \rho_a^2 \int_A \int_A \phi_{i,k} \phi_{i,l} C_{D,k} C_{D,l} \bar{u}_k \bar{u}_l \text{coh}_{u_k u_l} \sqrt{S_{u_k}(\omega) S_{u_l}(\omega)} dA_k dA_l. \quad (3.60)$$

**Equation 3.60** can be rewritten as:

$$S_{F_k F_l}(\omega) = (\rho_a C_{D,r} \bar{u}_r A)^2 \sqrt{S_{u_k}(\omega) S_{u_l}(\omega)} \chi_{\phi_i}^2(\omega), \quad (3.61)$$

where subscript  $r$  denotes reference, and  $\chi_{\phi_i}^2(\omega)$  is the aerodynamic admittance function for mode  $i$ :

$$\chi_{\phi_i}^2(\omega) = \frac{1}{A^2} \int_A \int_A \frac{C_{D,k} C_{D,l} \bar{u}_k \bar{u}_l}{C_{D,r}^2 \bar{u}_r^2} \phi_{i,k} \phi_{i,l} \text{coh}_{v_k v_l} dA_k dA_l. \quad (3.62)$$

In the Eurocodes, the decay coefficients  $C_z$  and  $C_y$  take the value of 11.5. A good approximation to the squared term in **Equation 3.61** is a spectral density of the fluctuating wind velocity at a reference height  $\sqrt{S_{u_k}(\omega) S_{u_l}(\omega)} = S_{u_r}(\omega)$ . The reference height with subscript  $r$  is often chosen to be around  $0.607h$ , where  $h$  is the object height.

From **Equation 3.61**, a force time series can be generated based on the force spectrum. The generated time series can be used as input in the modal equation of motion in **Equation 3.51** to obtain the dynamic response.

### 3.6 Spectral representation

The spectral representation method simulates a time series from a cross-spectral density matrix  $\mathbf{S}_{xy}(\omega)$  based on the complex valued Euler's formula  $e^{i\phi_k}$  with a random phase angle  $\phi_k$ . This enables the generation of a random time series from a specified spectral density. The new random time series inherit the same statistical properties as the original time series from which the spectral density was generated. The method was initially proposed by Shinozuka (1971) and Shinozuka and Deodatis (1991).

#### 3.6.1 Discrete Fourier transform

The discrete Fourier transform DFT of a discrete random signal  $x$  is defined as:

$$X(\omega_k) = X_k = \frac{1}{N} \sum_{n=0}^{N-1} x_n e^{-i\left(\frac{2\pi}{N}\right)kn}, \quad x_n = x(t_n), \quad (3.63)$$

where  $n \in [0, N - 1]$  and  $k \in [0, N - 1]$ . Similarly, the inverse discrete Fourier transform IDFT is defined as:

$$x(t_n) = x_n = \frac{1}{N} \sum_{k=0}^{N-1} X_k e^{i\frac{2\pi}{N}kn}. \quad (3.64)$$

If the discrete random signal  $x$  is a continuous function instead, **Equation 3.63** and **Equation 3.64** become the continuous Fourier transform and continuous inverse Fourier transform in **Section 3.2**.

### 3.6.2 Spectral representation

Assume that a spectral density can be written as:

$$\mathbf{S}_{xx}(\omega) = \mathbf{X}\mathbf{X}^*, \quad (3.65)$$

where  $\mathbf{X}$  is the lower triangular Cholesky decomposition of the spectral density  $\mathbf{S}_{xx}(\omega)$ , and the asterisk  $*$  superscript denotes the Hermitian transpose. Suppose that  $\mathbf{X}$  is the DFT of the random process  $\mathbf{x}$ , and that it can be expressed as:

$$\mathbf{X}_k = |\mathbf{X}_k|e^{i\phi_k}, \quad (3.66)$$

where  $\phi_k$  is a random phase angle, then the following expression is obtained by substituting **Equation 2.66** into **Equation 2.65**:

$$|\mathbf{X}_k|e^{i\phi_k}|\mathbf{X}_k|e^{-i\phi_k} = |\mathbf{X}_k||\mathbf{X}_k| = \mathbf{S}_{xxk}. \quad (2.67)$$

By substituting **Equation 2.67** back into **Equation 2.66**, the decomposition  $\mathbf{X}_k$  can be expressed as:

$$\mathbf{X}_k = \sqrt{\mathbf{S}_{xxk}}e^{i\phi_k}. \quad (3.68)$$

From **Equation 3.68**, a random process in the time domain can be constructed with an arbitrary stochastic distribution. However, from **Equation 2.69**, observe that the contributions from each frequency  $k$  are summed. By virtue of the central limit theorem, the random process in the time domain  $x_n$  will converge to a Gaussian process if the number  $N - 1$  is large. Thus, the phase angle  $\phi_k$  should inherit a random number between 0 and  $2\pi$ .

A smoothed continuous spectrum  $\tilde{S}_k$  can be estimated by:

$$\tilde{S}_k \approx \frac{2\pi}{N\Delta t}S_k = \Delta\omega S_k. \quad (3.69)$$

By substituting the smoothed spectrum  $\tilde{S}_k$  in **Equation 2.69** into **Equation 2.68**, and supposing that the spectrum is one-sided, the following expression is obtained:

$$\mathbf{X}_k = \sqrt{2\Delta\omega\tilde{\mathbf{S}}_{xxk}}e^{i\phi_k}. \quad (3.70)$$

The factor two comes from preserving the variance. By taking the IDFT in **Equation 3.64** of **Equation 2.70**, the random process  $x_n$  becomes:

$$x_n = \frac{1}{N} \sum_{k=0}^{N-1} \sqrt{2\Delta\omega\tilde{\mathbf{S}}_{xxk}} e^{i\phi_k} e^{i\omega_k n}, \quad (3.71)$$

where the smoothed spectrum  $\tilde{\mathbf{S}}_{xxk}$  is a specified spectrum. The square of the smoothed spectrum can be expressed in the same manner as in **Equation 3.66**. **Equation 3.71** is a complex valued process, in which only the real values are of interest. Thus, **Equation 3.71** can finally be rewritten as:



$$x(t_n) = \mathcal{R}e \left\{ \frac{1}{N} \sum_{k=0}^{N-1} \sqrt{2\Delta\omega \mathbf{\tilde{S}}_{xxk}} e^{i\phi_k} e^{i\omega_k n} \right\}. \quad (3.72)$$

The stochastic properties of the simulated time series in **Equation 3.72** can be verified by calculating the spectral density of the simulated time series. The simulated spectrum can be compared with the reference spectrum.

**Figure 2** shows a simulation of the turbulent wind load by using the generalized wind load method and spectral representation to generate a time-series. For comparison, the gust factor approach is also shown. Due to the stochastic nature of the simulations, the peaks of the generalized wind load will vary from simulation to simulation, sometimes exceeding the value given by the gust factor approach. However, the gust factor approach serves as a good indication of the maximum values of the turbulent wind load.

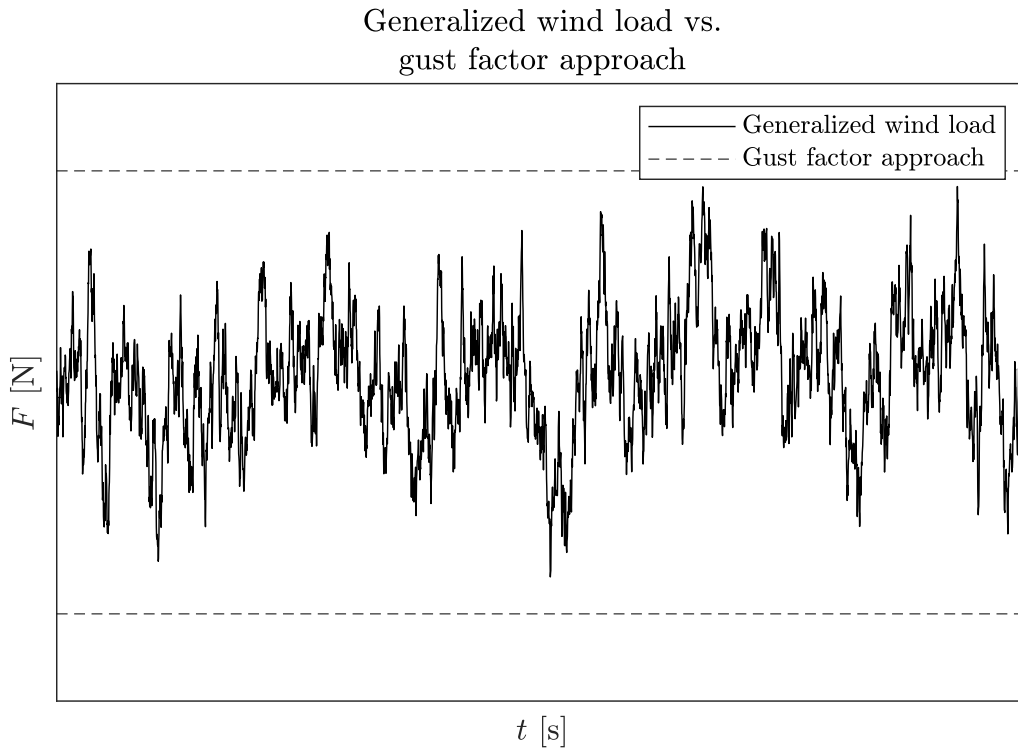


Figure 2 A simulation of the turbulent wind load with the generalized wind load method (black solid line), and the gust factor approach (black dashed line).

### 3.7 Numerical integration

To solve the equation of motion in **Equation 3.51**, a numerical integration scheme is required. In this thesis, an implicit Newmark integration scheme is chosen to address this problem. Newmark integration is based on the following approximations:

$$\dot{x}_{n+1} = \dot{x}_n + \Delta t[\gamma\ddot{x}_{n+1} + (1 - \gamma)\ddot{x}_n], \quad (3.73)$$

$$x_{n+1} = x_n + \Delta t\dot{x}_n + \frac{\Delta t^2}{2}[2\beta\ddot{x}_{n+1} + (1 - 2\beta)\ddot{x}_n], \quad (3.74)$$

where  $n$  is the time step,  $x$  is the response displacement,  $\dot{x}$  is the response velocity,  $\ddot{x}$  is the response acceleration,  $\Delta t$  is the time increment, and  $\beta$  and  $\gamma$  are integration constants. From **Equation 3.73** and **Equation 3.74**, the following expressions can be obtained for the response acceleration and velocity:

$$\ddot{x}_{n+1} = \frac{1}{\beta\Delta t^2}(x_{n+1} - x_n - \Delta t\dot{u}_n) - \left(\frac{1}{2\beta} - 1\right)\ddot{x}_n, \quad (3.75)$$

$$\dot{x}_{n+1} = \frac{\gamma}{\beta\Delta t}(x_{n+1} - x_n) - \left(\frac{\gamma}{\beta} - 1\right)\dot{x}_n - \Delta t\left(\frac{\gamma}{2\beta} - 1\right)\ddot{x}_n. \quad (2.76)$$

By substituting **Equation 3.75** and **Equation 3.76** into the equation of motion in **Equation 3.51** at time instant  $t_{n+1}$ :

$$m\ddot{x}_{n+1} + c\dot{x}_{n+1} + kx_{n+1} = p_{n+1},$$

then the following expression can be obtained:

$$\begin{aligned} \left(\frac{m}{\beta\Delta t^2} + \frac{\gamma c}{\beta\Delta t} + k\right)x_{n+1} = p_{n+1} + m\left[\frac{1}{\beta\Delta t^2}x_n + \frac{1}{\beta\Delta t}\dot{x}_n + \left(\frac{1}{2\beta} - 1\right)\ddot{x}_n\right] + \dots \\ c\left[\frac{\gamma}{\beta\Delta t}x_n + \left(\frac{\gamma}{\beta} - 1\right)\dot{x}_n + \Delta t\left(\frac{\gamma}{2\beta} - 1\right)\ddot{x}_n\right]. \end{aligned} \quad (3.77)$$

By rearranging **Equation 3.77**, the following expression for the response displacement can be obtained:

$$x_{n+1} = \frac{p_{n+1}^{\text{eff}}}{k^{\text{eff}}}, \quad (3.78)$$

where

$$k^{\text{eff}} = \frac{m}{\beta\Delta t^2} + \frac{\gamma c}{\beta\Delta t} + k, \quad (3.79)$$

$$\begin{aligned} p_{n+1}^{\text{eff}} = p_{n+1} + m\left[\frac{1}{\beta\Delta t^2}x_n + \frac{1}{\beta\Delta t}\dot{x}_n + \left(\frac{1}{2\beta} - 1\right)\ddot{x}_n\right] + \dots \\ c\left[\frac{\gamma}{\beta\Delta t}x_n + \left(\frac{\gamma}{\beta} - 1\right)\dot{x}_n + \Delta t\left(\frac{\gamma}{2\beta} - 1\right)\ddot{x}_n\right]. \end{aligned} \quad (3.80)$$

**Equation 3.78**, **Equation 3.79**, and **Equation 3.80** are valid for an SDOF system. For an MDOF system, the expressions become:

$$\mathbf{x}_{n+1} = [\mathbf{K}^{\text{eff}}]^{-1}\mathbf{P}_{n+1}^{\text{eff}}, \quad (3.81)$$

$$\mathbf{K}^{\text{eff}} = \frac{1}{\beta\Delta t^2}\mathbf{M} + \frac{\gamma}{\beta\Delta t}\mathbf{C} + \mathbf{K}, \quad (3.82)$$

$$\begin{aligned} \mathbf{P}_{n+1}^{\text{eff}} = \mathbf{P}_{n+1} + \mathbf{M}\left[\frac{1}{\beta\Delta t^2}\mathbf{x}_n + \frac{1}{\beta\Delta t}\dot{\mathbf{x}}_n + \left(\frac{1}{2\beta} - 1\right)\ddot{\mathbf{x}}_n\right] + \dots \\ \mathbf{C}\left[\frac{\gamma}{\beta\Delta t}\mathbf{x}_n + \left(\frac{\gamma}{\beta} - 1\right)\dot{\mathbf{x}}_n + \Delta t\left(\frac{\gamma}{2\beta} - 1\right)\ddot{\mathbf{x}}_n\right]. \end{aligned} \quad (3.83)$$

Newmark integration is unconditionally stable when:

$$2\beta \geq \gamma \geq \frac{1}{2},$$

and conditionally stable when:

$$\gamma \geq \frac{1}{2}, \quad \beta < \frac{\gamma}{2}.$$

When Newmark integration is conditionally stable, the time-increment must be smaller than:

$$\Delta t_{cr} \leq \frac{\Omega_{cr}}{\omega_{max}},$$

where  $\Omega_{cr}$  is the critical sampling frequency and  $\omega_{max}$  is the highest natural frequency of the eigenvalue problem in **Equation 3.53**. The critical sampling frequency  $\Omega_{cr}$  can be expressed as:

$$\Omega_{cr} = \frac{\xi \left( \gamma - \frac{1}{12} \right) + \sqrt{\frac{\gamma}{2} - \beta + \xi^2 \left( \gamma - \frac{1}{2} \right)^2}}{\frac{\gamma}{2} - \beta}.$$

The choice of the integration constants determines whether Newmark integration becomes an explicit or implicit method, and the amount of numerical or algorithmic damping. The results of the choice of integration constants are shown in **Table 2**. In this thesis, the average acceleration method is used which provide rapid computations.

Method	$\gamma$	$\beta$	Stability condition	Error
Average acceleration	$\frac{1}{2}$	$\frac{1}{4}$	Unconditional	$O(\Delta t^2)$
Linear acceleration	$\frac{1}{2}$	$\frac{1}{6}$	$\Omega_{cr} _{\xi=0} = 3.464$	$O(\Delta t^2)$
Numerically damped	$\geq \frac{1}{2}$	$\geq \frac{1}{4} \left( \gamma + \frac{1}{2} \right)^2$	Unconditional	$O(\Delta t)$

Table 2 Overview of the integration constants in Newmark integration, the stability conditions and error (Cook, Malkus, Plesha, & Witt, 2002).

### 3.8 Wind loading model

There are several different wind loading models. The wind loading models describe how the dynamic response of a structure is obtained, and how the wind is described. Wind loading models can roughly be divided into two categories.

The first category is frequency-domain analysis or spectral analysis. In spectral analysis, the wind is described in the frequency-domain in the form of a wind spectrum. The force spectrum is found by multiplying the wind spectrum with the aerodynamic admittance. The mechanical admittance can be found from structural parameters, and the response spectrum is found by multiplying the mechanical admittance with the force spectrum. By integrating the response spectrum over its frequency domain, the variance of the response displacement can be found. The variance of the response acceleration can be found by integrating the fourth moment of the response spectrum. This approach is illustrated in **Figure 3**.

The gust factor approach is based on spectral analysis, where the response spectrum is approximated. In the gust factor approach, the background factor approximates the steady-state response of the structure. In **Figure 3**, the steady-state response is the part of the curve without the

peak around the natural frequency. The resonant response factor approximates the peak in the response spectrum. Thus, the gust factor approach is a simplification of spectral analysis, assuming that the response is narrow banded. Due to the simplifications, some accuracy is also lost.

The second category is time-domain analysis based on wind measurements. In this approach, long-term measurements of the wind velocity are done in-situ, and the maximum ten-minute wind series is separated for further computations. Through analytical considerations of the geometry of the structure, a force time-series can be computed. By solving the equation of motion numerically for the force time-series, the response time-series can be obtained. From the response time-series, the variance, peak and other properties can be assessed. This approach is illustrated in **Figure 4**.

The measurements-based time-domain analysis is used in bridge engineering, tall structures engineering, and more. It is often used for critical structures for which the wind conditions are very local and of high importance. The analysis of the structural response is based on real in-situ measurements. This may result in higher accuracy but does also require more time due to the need to do in-situ measurements. In this method, air-elastic effects may be included readily based on analytical considerations of the air-elastic stiffness and damping. The wind series may also be reproduced in a wind tunnel to experimentally determine the air-elastic effects and the aerodynamic admittance.

The third category is a mix of spectral analysis and time-domain analysis. The wind is described in terms of a frequency-domain wind spectrum. From the wind spectrum, a time series can be generated which will inherit the statistical properties of the wind spectrum. From the time series, the force series and response series can be computed as in the second category of measurements-based time-domain analysis. There is also the possibility of generating a time series of the force from the force spectrum. To obtain the force spectrum, the wind spectrum and aerodynamic admittance are multiplied. From the force time-series, the response can be computed by solving the equation of motion numerically. This approach is illustrated in **Figure 5**.

The mixed wind loading model can be used if a wind series is unavailable. However, the mixed wind loading model is computationally expensive due to the need to generate time series and the numerical solution of the equation of motion. Yet, the mixed wind loading model is a compromise between pure spectral analysis and measurements-based time-domain analysis.

In a pure spectral analysis, the aerodynamic admittance is an empirical approximation. As such, it is accurate in the cases it was developed for. However, it may be inaccurate in other cases. Thus, the blind use of existing aerodynamic admittance function can lead to inaccurate results.

In the mixed wind loading model, the force series may be obtained through the aerodynamic admittance function, or through analytical considerations that are the same for the measurements-based time-domain wind loading model. This makes the mixed wind loading model the most flexible in use. However, the accuracy may be different from case to case, dependent on the individual choice of each structural engineer. For accuracy, the measurements-based wind loading model is superior. In any case, the highest accuracy requires cumbersome and often expensive wind tunnel testing of scale models.

In this thesis, a mixed wind loading model is used called the generalized wind load method. The generalized wind load method is based upon a wind spectrum, and a modal aerodynamic admittance function. From the force spectrum, a force series is generated, and the response is

solved numerically. The wind loading model in the Eurocodes is partly based on the gust factor approach, and partly based on the generalized wind loading model.

**Spectral analysis  
Frequency-domain**

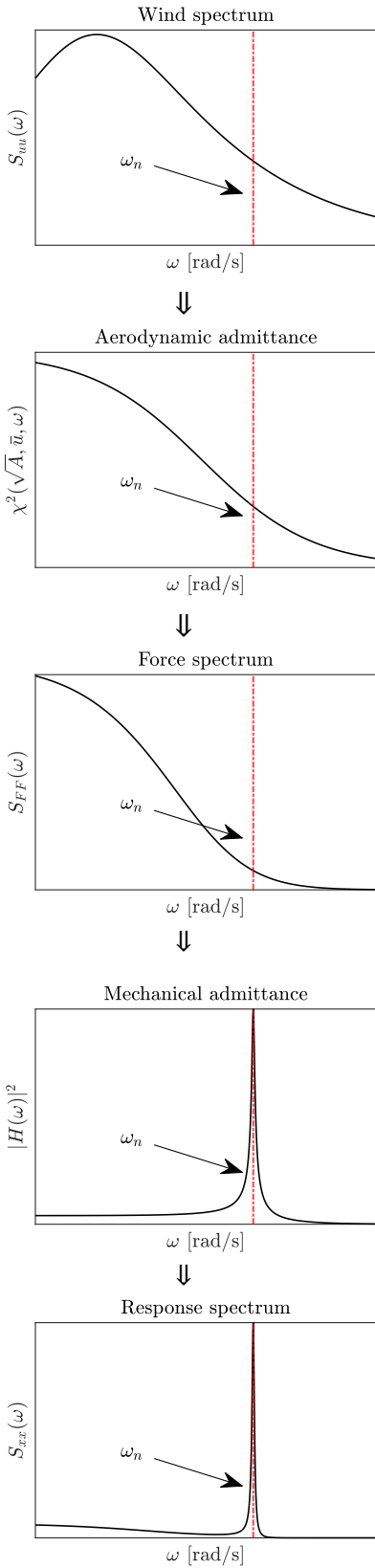


Figure 3 Frequency-domain spectral response analysis.

**Measurements based  
Time-domain**

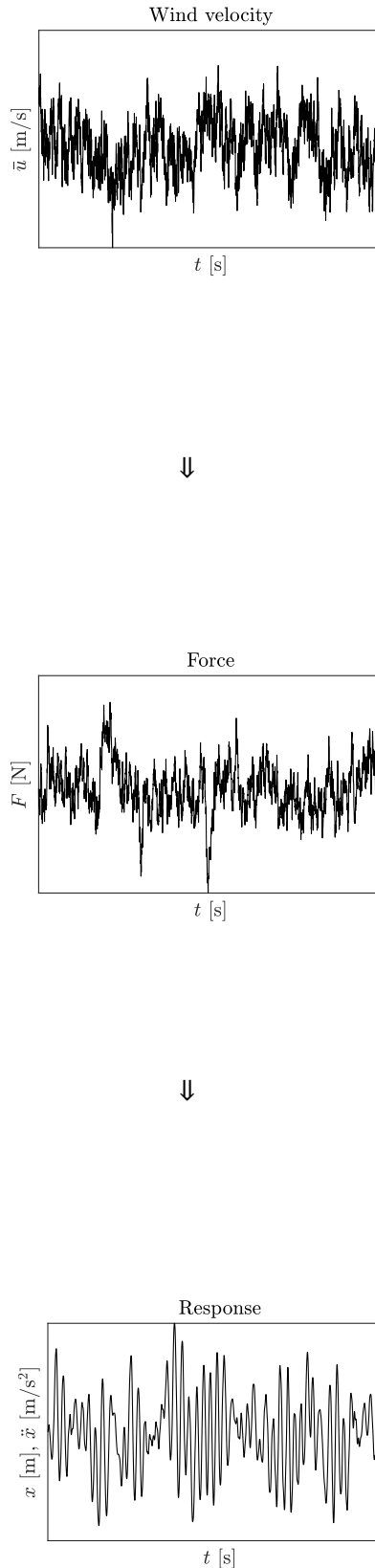


Figure 4 Time-domain measurement-based response analysis.

**Mixed method  
Time- & frequency domain**

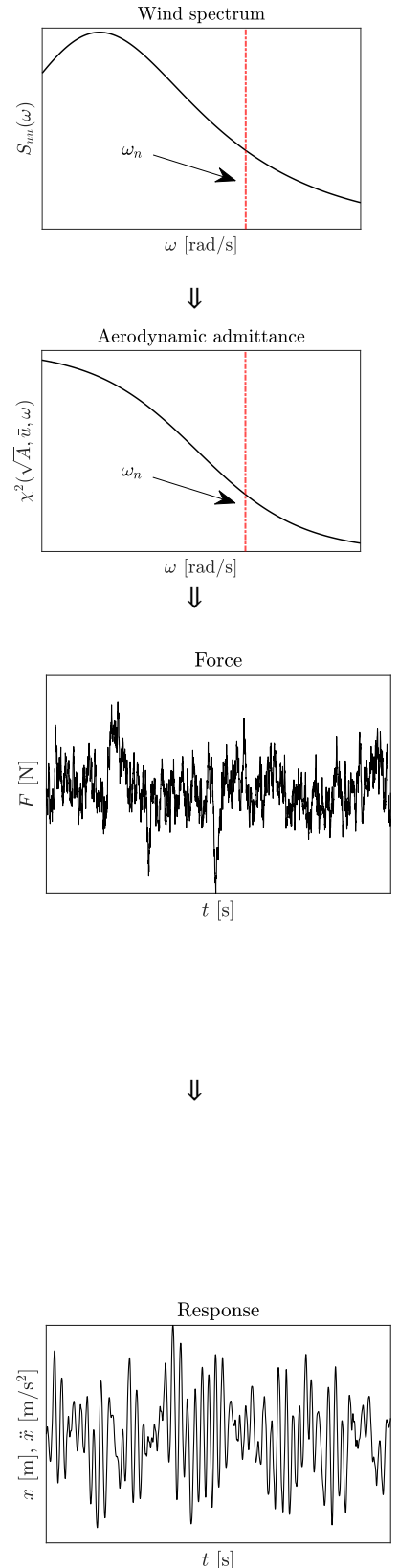


Figure 5 Time-domain wind spectrum-based response analysis.

## 4 Method

In this chapter, the method of analysis in this thesis and the mathematical description is presented. First, the structural system is described. Second, the variables and parameters in the reference frame are described. Third, the parameters and their range in the analyses are described. Fourth, the simulations<sup>3</sup> and their technical details are described. Fifth, the post-processing units of the simulations are described. In the following paragraphs, an overview of the method is provided.

In this thesis, time-domain and spectral or frequency-domain analysis of wind loads on parametrized timber frames are numerically analyzed and simulated in MATLAB based on the gust factor approach used in the Eurocodes (NS-EN 1991-1-4:2005) and the generalized wind load method described in literature. The serviceability of the parametrized frames subjected to different wind loads is assessed, and nonlinear expressions for the response accelerations and displacements are proposed based on the simulated results. A sigmoid behavior of the natural frequency with respect to the connection stiffness is proposed, and a frequency reduction factor is formulated.

A parametrized finite element model of a regular semi-rigid frame with consistent floor heights, bay lengths, frame spacings, column stiffnesses, beam stiffnesses, beam-to-column stiffnesses, support conditions, and modal damping ratios, is formulated in MATLAB. The beams are formulated using Euler-Bernoulli beam theory and the columns are formulated using Timoshenko beam theory. Rotational springs are added to the beam ends to control the beam-to-column rotational connection stiffness<sup>4</sup>. A reference frame with semi-rigid beam-to-column stiffnesses is used to study the effect of different parameters. The static and dynamic properties of the reference frame are validated against a model in Abaqus CAE.

Cubic beam elements with six degrees of freedom (DOF) are used for the element stiffness matrices of the columns and beams. The global stiffness matrix is reduced to include only horizontal DOFs by using static condensation to condense vertical and rotational DOFs. Consistent element mass matrices are used and reduced in the same way to include only horizontal DOFs. Mass-less columns and an equivalent density to include column mass, deck mass, and live loads are used in the beams.

Spatially coherent buffeting wind velocity time histories with a ten-minute averaging period are generated from a cross-spectral density matrix based on the spectral representation method formulated by Shinozuka (1971). The single-point power spectral density from NS-EN 1991-1-4:2005 Annex B.1 proposed by Kaimal et al. (1972) and a widely used exponential coherence function proposed by Davenport (1961b) are used to generate the cross-spectral density matrix. By using the cross-spectral density matrix of the buffeting wind velocity and the generalized wind load method outlined in Kareem (1986), the buffeting wind force cross-spectral density matrix is obtained. When following the same procedure by Shinozuka (1971), wind buffeting force time histories are generated. Modal analysis of buffeting force time histories is performed to calculate the acceleration and displacement response of the parametrized frames.

---

<sup>3</sup> For the remainder of this thesis, the *generalized wind load* is referred to as *simulations*.

<sup>4</sup> In this thesis, the beam-to-column rotational connection stiffness is referred to as *the beam-to-column rotational stiffness*, and *the connection stiffness*.

721 710 frames with different wind loads are simulated, resulting in a database consisting of more than 10.8 million simulations. More than 2.16 million unique combinations are simulated. Characteristics and trends of the data are investigated, and nonlinear expressions for some variables are proposed based on nonlinear regressions. The performance of the proposed expressions is compared with the expressions in the Eurocodes, and the serviceability criteria of the frames are investigated.

A sigmoid behavior of the natural frequency with respect to the beam-to-column rotational stiffness is hypothesized and validated. The natural frequencies for 24 300 frames with varying connection stiffnesses are computed, the natural frequencies are normalized and the connection stiffness adjusted, and an expression for the frequency reduction factor based on the normalized natural frequency and adjusted beam-to-column connection stiffness is formulated.

The effect of adding more mass to a specific floor of the structure is investigated. This is performed by simulating a structure consisting ten floors with different added masses, and different locations of the added masses. For this specific investigation, the gust factor accelerations and generalized wind load accelerations are computed for 194 400 frames, resulting in 972 000 simulations in total.

#### 4.1 Structural system

The structural system consists of several regular timber frames with spacing  $s$ , floors  $n_{\text{floor}}$ , bays  $n_{\text{bay}}$ , beam dimensions  $h_b \times b_b$ , beam length  $L_b$ , column dimensions  $h_c \times b_c$ , column length  $H$ , beam-to-column stiffness  $k_\theta$ , horizontal support stiffness  $k_{x,\text{sup}}$ , vertical support stiffness  $k_{z,\text{sup}}$ , rotational support stiffness  $k_{\theta,\text{sup}}$ , Rayleigh damping with damping ratio  $\xi$ , building width  $b$ , building depth  $d$ , building height  $h$ , and load  $p$ . The columns are considered mass-less, with all the mass distributed to the beams. The load  $p$ , including self-weight and live load, is converted into an equivalent density  $\rho_e$  in the beams. A planar illustration of the structural system can be viewed in **Figure 6**.



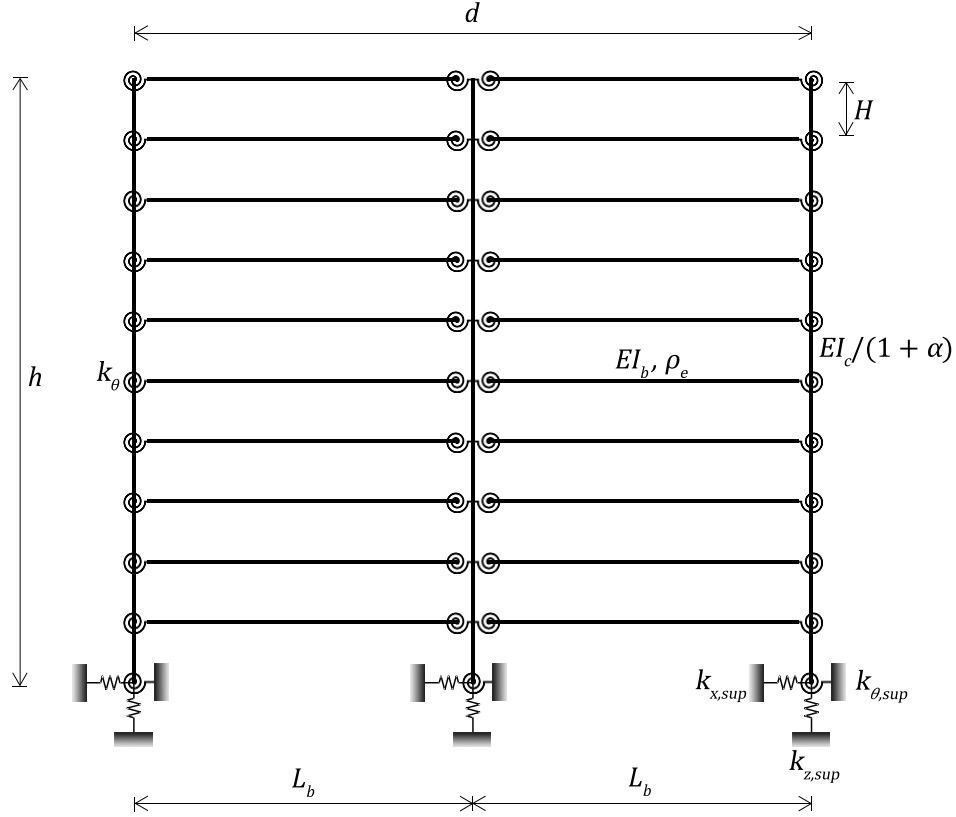


Figure 6 An arbitrary regular frame with floors  $n_{\text{floor}}$ , bays  $n_{\text{bay}}$ , beam stiffness  $EI_b$ , beam length  $L_b$ , column stiffness  $EI_c/(1 + \alpha)$ , column length  $H$ , beam-to-column stiffness  $k_\theta$ , horizontal support stiffness  $k_{x,\text{sup}}$ , vertical support stiffness  $k_{z,\text{sup}}$ , rotational support stiffness  $k_{\theta,\text{sup}}$ , building depth  $d$ , building height  $h$ , and equivalent beam density  $\rho_e$ .

## 4.2 Reference frame

The reference frame consists of 10 floors with floor height 3 m, 2 bays with beam length 8 m, pinned support conditions and a semi-rigid beam-to-column connection. The structural parameters of the reference frame can be found in **Table 3**.

Parameter	Symbol	Value
Number of floors	$n_{\text{floor}}$	10
Number of bays	$n_{\text{bay}}$	2
Elastic modulus	$E$	$13000 \times 10^6 \text{ N/mm}^2$
Beam dimensions	$h_b \times b_b$	$0.825 \text{ m} \times 0.28 \text{ m}$
Column dimensions	$h_c \times b_c$	$0.62 \text{ m} \times 0.28 \text{ m}$
Beam-to-column stiffness	$k_\theta$	$20 \times 10^3 \text{ Nm/rad}$
Horizontal support stiffness	$k_{x,\text{sup}}$	$10^{12} \text{ N/m}$
Vertical support stiffness	$k_{z,\text{sup}}$	$10^{12} \text{ N/m}$
Rotational support stiffness	$k_{\theta,\text{sup}}$	$1 \text{ Nm/rad}$
Damping ratio	$\xi$	2%
Beam length	$L_b$	8 m
Column length	$H$	3 m
Building depth	$d$	16 m
Building height	$h$	30 m
Building width	$b$	24 m
Frame spacing	$s$	2.4 m
Surface load	$p_s (\rho_e)$	$2600 \text{ N/m}^2 (636 \text{ kg/m})$

Table 3 Parameter names, symbols, and values in the reference frame. The parameters are illustrated in **Figure 6**.

The variables that will be analyzed are the maximum building displacement  $x_{max}$ , maximum acceleration  $\ddot{x}_{max}$ , and the fundamental frequency  $f_1$ . Since the loads in this thesis are in the serviceability limit state with a yearly return period, the inter-story drift is not considered. The inter-story drift should be considered in the ultimate limit state.

The variables inherit the values in **Table 4** for the reference frame. For completeness, the inter-story drifts for the single-year return period is also included in the table.

Fundamental frequency	Generalized wind load - acceleration	Gust factor - acceleration	Generalized wind load - inter-story drift	Gust factor - inter-story drift
0.5654 Hz	0.0551 m/s <sup>2</sup>	0.0536 m/s <sup>2</sup>	0.0022	0.0013

Table 4 Variables and their values for the reference frame. The variables are shown for both the generalized wind load, and gust factor approach. To account for the stochastic variation of the generated time series, a total of 50 simulations were performed to obtain the values in this table. The values should be accurate to the fifth decimal place.

### 4.3 Parameters

First, a parameter study is conducted. The parameter study is conducted to investigate the importance of the different parameters and to determine a reasonable range of values for the different parameters. **Table 5** shows the parameters and their range in the parameter study. In the parameter study, a total of 318 unique combinations were simulated. Each unique combination was simulated 30 times, resulting in 9540 simulations in total.

Name	Symbol	Value (start:end)
Number of floors	$n_{floor}$	5 : 12
Number of bays	$n_{bay}$	1 : 6
Beam dimensions	$h_b \times b_b$	0.5 m $\times$ 0.28 m : 1.0 m $\times$ 0.28 m
Column dimensions	$h_c \times b_c$	0.5 m $\times$ 0.28 m : 0.8 m $\times$ 0.28 m
Beam-to-column stiffness	$k_\theta$	$5 \times 10^6$ Nm/rad : $30 \times 10^6$ Nm/rad
Horizontal support stiffness	$k_{x,sup}$	$10^7$ N/m : $10^9$ N/m
Vertical support stiffness	$k_{z,sup}$	$10^7$ N/m : $10^9$ N/m
Rotational support stiffness	$k_{\theta,sup}$	$2.5 \times 10^3$ Nm/rad : $15 \times 10^3$ Nm/rad
Damping ratio	$\xi$	0.01:0.03
Beam length	$L_b$	6 m : 10 m
Column length	$H$	2.5 m : 5 m
Load	$p_s (\rho_e)$	1500 N/m <sup>2</sup> : 7000 N/m <sup>2</sup>

Table 5 Overview of the parameters in the parameter study. Each of the single parameters are varied individually.

Second, simulations are carried out for each floor with an adapted range of parameters. The adapted parameters are used to limit the total number of simulations and thus reducing the computing time. In the simulations, the damping ratio is kept constant at 2%. This is due to the intrinsic variability and uncertainty regarding this value. Measurements of the damping ratio in existing timber structures are around 2%. This limitation is discussed in **Section 6.1.1**. The horizontal and vertical stiffness are set as equal. This choice is made based on simple considerations of the foundation stiffness for three general soils. The rotational stiffness of the foundation is neglected as its own parameter and is to some extent represented through the vertical support stiffness. Each unique combination of parameters is simulated five times to include the effects of the stochastic variation of the generated time series.

**Table 6** shows the parameters and their range in the simulations. In the simulations, 721 710 different frames are simulated for three different wind loads. To account for the stochastic nature of the wind series simulations, the simulations are repeated five times for each combination. In total, this results in 10 825 650 simulations.

The effect of the connection stiffness is studied separately for a limited number of frames. **Table 7** shows the range of the parameters, where pinned, semi-rigid, and rigid support conditions are studied. For the connection stiffness, a range representing pinned to rigid connections are computed. A total of 24 300 frames are simulated for the effect of the connection stiffness.

The effect of the added mass is studied separately for a limited number of frames with ten floors. **Table 8** shows the range of the parameters, where the amount and location of the added mass are studied. A total of 194 400 frames are simulated for the effect of the added mass.

**Figure 7** shows a flowchart of the simulations in this thesis.

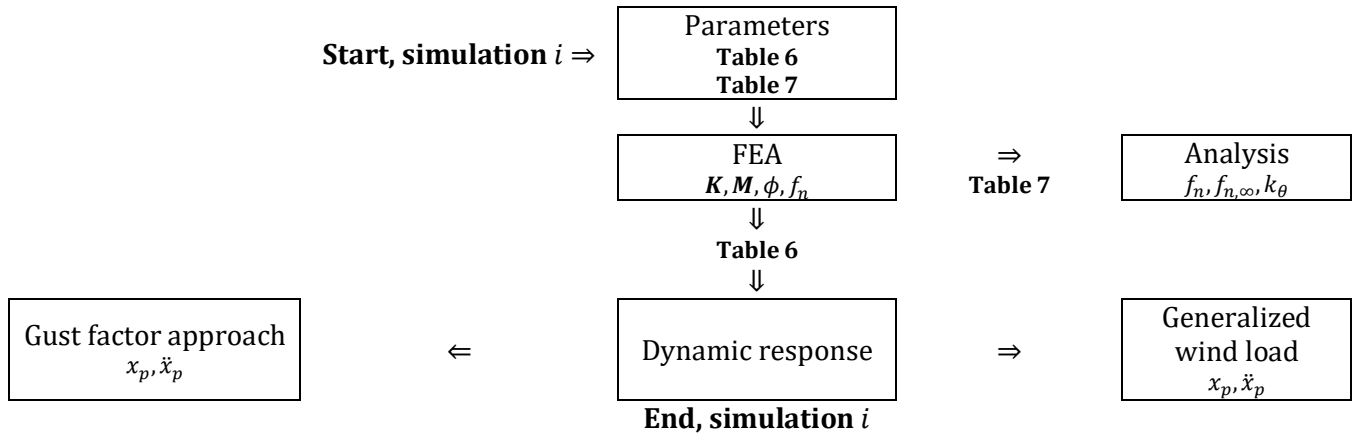


Figure 7 Flowchart of the method in this thesis.

Floors	Bays	Column height $b_c = 0.28$ m	Beam height $b_b = 0.28$ m	Beam-to-column stiffness	Translational support stiffness		Rotational support stiffness	Beam length	Floor height	Surface load	Line load	Wind velocity
					$k_{x,sup}$	$k_{z,sup}$						
$n_{floor}$	$n_{bay}$	$h_c$	$h_b$	$k_\theta$	$k_{x,sup}$	$k_{z,sup}$	$k_{\theta,sup}$	$L_b$	$H$	$p_s$	$p_L$	$v_{b,0}$
–	–	m	m	Nm/rad	N/m	N/m	Nm/rad	m	m	N/m <sup>2</sup>	kg/m	m/s
5	2	0.30	0.625 0.725 0.825	$10 \times 10^6$	$10^7$ $10^8$ $10^9$	1	$5 \times 10^6$ $10 \times 10^6$	6	3.0	1600	391	22
	3	0.38		$15 \times 10^6$								26
	4	0.46		$20 \times 10^6$								30
6	2	0.30		$10 \times 10^6$								22
	3	0.38		$15 \times 10^6$								26
	4	0.46		$20 \times 10^6$								30
7	2	0.30,0.38		$10 \times 10^6$								22
	3	0.46,0.54		$15 \times 10^6$								26
	4			$20 \times 10^6$								30
8	2	0.38,0.46		$10 \times 10^6$								22
	3	0.54,0.62		$15 \times 10^6$								26
	4			$20 \times 10^6$								30
9	2	0.46,0.54	$10 \times 10^6$	22								
	3	0.62,0.70	$15 \times 10^6$	26								
	4		$20 \times 10^6$	30								
10	2	0.54,0.62	$15 \times 10^6$	22								
	3	0.70,0.78	$20 \times 10^6$	26								
	4		$25 \times 10^6$	30								
11	2	0.62,0.70	$15 \times 10^6$	26								
	3	0.78,0.86	$20 \times 10^6$									
	4		$25 \times 10^6$									
12	2	0.70,0.78	$15 \times 10^6$	26								
	3	0.86,0.94	$20 \times 10^6$									
	4		$25 \times 10^6$									

Table 6 Overview of the parameters in the simulations. For each floor, combinations of all the parameter values are varied. The building width is kept constant at  $b = 24$  m, and the frame spacing at  $s = 2.4$  m. In total, 721 710 frames with different wind loads are simulated, resulting in more than 10.8 million simulations.

Floors	Bays	Column height	Beam height	Beam-to-column stiffness	Translational support stiffness		Rotational support stiffness	Beam length	Floor height	Surface load	Line load
		$b_c = 0.28 \text{ m}$	$b_b = 0.28 \text{ m}$		$k_\theta$	$k_{x,sup}$	$k_{z,sup}$				
$n_{floor}$	$n_{bay}$	$h_c$	$h_b$					$L_b$	$H$	$p_s$	$p_L$
–	–	m	m	Nm/rad	N/m	N/m	Nm/rad	m	m	N/m <sup>2</sup>	kg/m
5	2	0.30	0.625 0.725 0.825	$10^3 - 10^{11}$	$10^9$	1 $5 \times 10^6$ $10^{12}$	6 8 10	3.0 3.5 4.0	3000	734	
	3	0.38									
	4	0.46									
7	2	0.38									
	3	0.46									
	4	0.54									
9	2	0.46									
	3	0.54									
	4	0.62									

Table 7 Overview of the parameters in the analysis of the connection stiffness. In total, 24 300 frames are computed.

Floors	Bays	Column height	Beam height	Beam-to-column stiffness	Translational support stiffness		Rotational support stiffness	Beam length	Floor height	Surface load	Line load	Mass factor	Height factor
		$b_c = 0.28 \text{ m}$	$b_b = 0.28 \text{ m}$		$k_\theta$	$k_{x,sup}$	$k_{z,sup}$						
$n_{floor}$	$n_{bay}$	$h_c$	$h_b$					$L_b$	$H$	$p_s$	$p_L$	$\eta_m$	$\eta_h$
–	–	m	m	Nm/rad	N/m	N/m	Nm/rad	m	m	N/m <sup>2</sup>	kg/m	–	–
10	2	0.62	0.625 0.725 0.825	$15 \times 10^6$ $20 \times 10^6$ $25 \times 10^6$	$10^9$	1 $10 \times 10^6$	6 8 10	3.0 4.0	1600	391	1, 2 3, 4 5	0.3, 0.4 0.5, 0.6 0.7, 0.8 0.9, 1.0	
	3	0.70											
	4	0.78											

Table 8 Overview of the parameters in the analysis of the effect of the location and amount of added mass in one floor. In total, 194 400 frames are computed, resulting in 972 000 simulations in total.

#### 4.4 Simulations

The simulations are conducted in two stages. First, initial simulations are performed to determine the reasonable range of the parameters. Second, comprehensive simulations using the reasonable range of parameters from the first stage are performed.

**Table 9** shows the time required for each floor of simulation and per 100 000 of simulations per floor. The simulations involve about 10.8 million simulations in total. To calculate the computing time, 30 simulations are carried out and the average time per simulation is found from the total elapsed time. The computation times listed are for a computer with an Intel i7-5500U CPU 2.40 GHz duo-core processor with 8 GB RAM.

Floors	–	5	6	7	8	9	10	11	12
Time/sim	s	0.397	0.517	0.690	0.925	1.24	1.65	2.17	2.82
Time/(100 000 sim)	hours	11.0	14.4	19.2	25.7	34.4	45.8	60.3	78.3

Table 9 Time required for the simulations (Intel i7-5500U CPU 2.40 GHz duo-core, 8 GB RAM, 1 139 968 simulations). The results indicate an exponential trend.

**Figure 8** is a graphical interpretation of **Table 9**, including a two-term exponential curve fit. For computers with other computing capacities, the trend will shift upwards or downwards in computing time. From **Figure 8**, observe that each computation becomes exponentially more cumbersome and time consuming as the number of floors increases, with the simulations for the 12 floors being more than seven times as expensive as the simulations for the five floors.

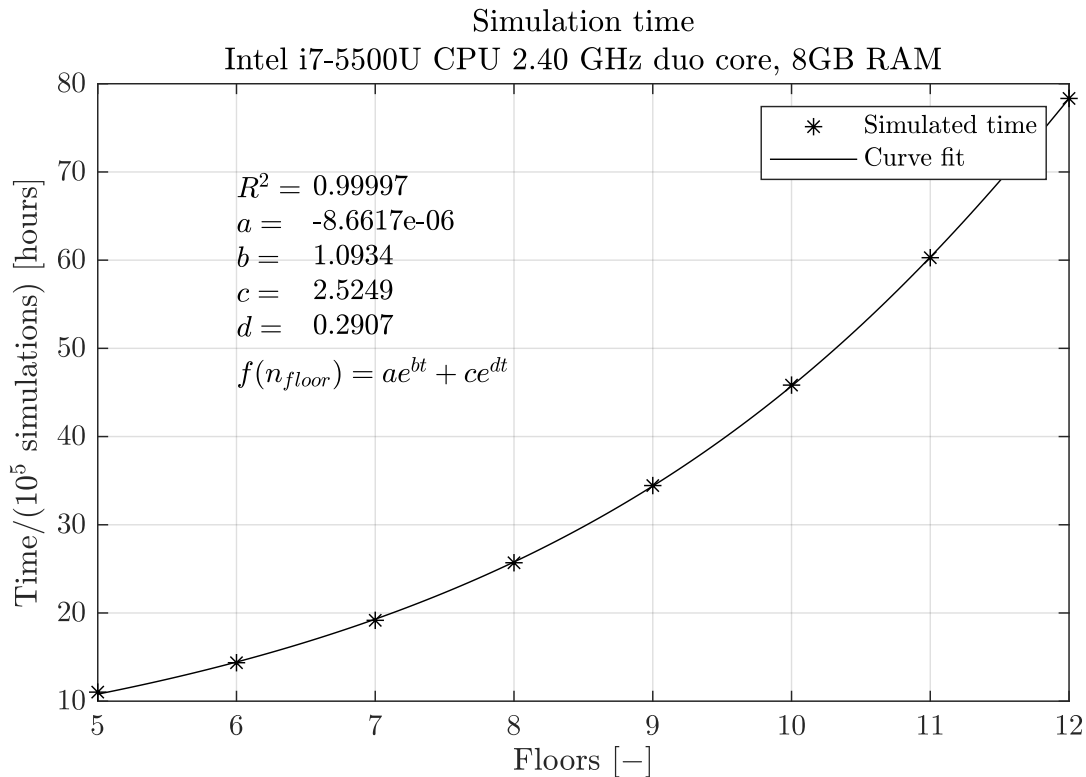


Figure 8 Simulation time per 100 000 simulations, including a two-term exponential curve fit. The simulation time is for a computer with Intel i7-5500U CPU 2.40 GHz duo core, and 8 GB RAM. Each point was simulated 30 times to account for stochastic variations in computing time.

The reason for the exponential trend is twofold. First, it is the need for solving the eigenvalue problem in **Equation 2.50**, repeated in **Equation 4.1** for convenience:

$$(\mathbf{k} - \lambda \mathbf{m})\boldsymbol{\phi}(A)\boldsymbol{\eta}(t) = \mathbf{0}. \quad (4.1)$$

As the number of floors increases, the rank of the stiffness matrix  $\mathbf{k}$  and mass matrix  $\mathbf{m}$  increases as well. The rank of the matrices is independent of the number of bays, beam stiffness, column stiffness and other parameters. Due to low damping ratio, the damping term becomes insignificant and is neglected in the solution of the eigenvalue problem. Second, the generation of time series and solving the equation of motion numerically becomes more cumbersome with an increasing number of floors. Each floor requires the generation of a unique time series from **Equation 2.68**, repeated in **Equation 4.2** for convenience:

$$x(t_n) = \mathcal{R}e \left\{ \frac{1}{N} \sum_{k=0}^{N-1} \sqrt{2\Delta\omega \tilde{\mathbf{s}}_{\mathbf{xxk}}} e^{i\phi_k} e^{i\omega_k t_n} \right\}. \quad (4.2)$$

Each time-series is solved independently through modal analysis before they are reassembled to find the total solution.

In this thesis, a total of five computers are used. The computer with the Intel i7 processor for which computing times are calculated, are used for writing the MATLAB routine, light simulations, and for post-processing most of the data. The simulations are mainly carried out by a computer with an Intel i5-9600K CPU 3.7 GHz hexa-core processor with 16 GB RAM. In parallel, lighter simulations are carried out by a computer with an Intel Xeon CPU E5-2697 v4 2.3 GHz 36-core processor with 128 GB RAM. A bulk of the simulations are also carried out by a computer with an Intel i7-7700 CPU 3.6 GHz quad-core processor with 32 GB RAM, and a computer with an Intel i7-3770K CPU 3.5 GHz quad-core processor with 16 GB RAM.

The simulations only account for the dynamic response. This means that all the different responses have zero average values. To make the simulations comparable to simulations such as the gust factor approach, only the dynamic response is calculated in the gust factor approach. This is achieved by setting the static, or size factor  $c_s$  in **Equation 3.47** as unity. To find the peak factor  $k_p$ , the up-crossing rate  $\nu$  in **Equation 3.42** is used with the background factor  $B$  as zero. Similarly, the peak dynamic displacement can be found by modifying the peak wind velocity in **Equation 3.45** to:

$$x_{p,GWL} = 2k_v \frac{\sigma_x}{\bar{x}} \sqrt{P_0} \cdot \bar{x}. \quad (4.3)$$

A return period of one year was chosen in this thesis to investigate the serviceability of the frames. The probability factor  $c_{\text{prob}}$  in NS-EN 1991-1-4:2005 inherits the value of 0.73 for a one-year return period, and unity for a fifty-year return period. Terrain category III is chosen for all the simulations, with a roughness length of 0.3 m.

#### 4.5 Post-processing

The output from the simulations are response accelerations, velocities, and displacements for each of the floors in the form of time series. As the simulations only account for dynamic responses with zero mean, it is appropriate to only consider the standard deviation of the responses. The standard deviation can be used to compute the appropriate response percentiles. This is also practical to minimize storage requirements. Thus, the standard deviation for each of the simulations are

calculated for the response accelerations and displacements. The response velocity is not of interest as it has no structural meaning or meaning towards serviceability.

The accelerations and displacements are evaluated by creating histograms and correlation plots. Histograms are created for the displacements, accelerations, mode shape parameters, and natural frequencies. Correlation plots are created for the accelerations and displacements of the gust factor approach with respect to the simulations. Intensity maps are created to compare the deviation between the gust factor approach and the generalized wind load, and to compare the serviceability requirements from wind-induced vibrations in ISO 10137. The deviation is measured in terms of percent bias.

A nonlinear least squares regression is performed for the dataset for the natural frequency, displacements, and accelerations for both the simulations and the gust factor approach. For the frequency reduction factor, a nonlinear least squares regression for the chosen algebraic sigmoid is performed for the adjusted connection stiffness.

#### 4.5.1 Displacements

To compare the response displacements between the gust factor approach and the simulations, the standard deviations from the simulations are multiplied with a factor  $2k_v\sqrt{P_0} = 7$  to obtain the peak displacements:

$$x_p = 2k_v\sqrt{P_0} \cdot \sigma_x. \quad (4.4)$$

The peak displacements from the simulations are compared to the peak displacements from the gust factor approach. For the gust factor approach, a unit value for the static component in the structural factor is used, and the dynamic component is only the turbulent part:

$$c_s c_d = c_d = \frac{2k_p \frac{\sigma_u}{\bar{u}} \sqrt{B^2 + R^2}}{7 \frac{\sigma_u}{\bar{u}} \sqrt{B^2}}. \quad (4.5)$$

Likewise, for the peak wind pressure, only the turbulent part is used:

$$q_p = c_e q_b = 7 \frac{\sigma_u}{\bar{u}} \left( \frac{1}{2} \rho_a v_m^2 \right). \quad (4.6)$$

#### 4.5.2 Accelerations

To compare the response accelerations between the gust factor approach and the simulations, the standard deviations from the simulations are multiplied with a factor 1.64, resembling the 95% percent fractile in a Gaussian process. The standard deviation from the gust factor approach is multiplied with the peak factor to obtain the 95% fractile:

$$\ddot{x}_{0.95,GWL} = 1.64 \times \ddot{\sigma}_{GWL}, \quad (4.7a)$$

$$\ddot{x}_{0.95,GF} = k_p \times \ddot{\sigma}_{GF}. \quad (4.7b)$$

The standard deviation from the gust factor approach  $\ddot{\sigma}_{GF}$  can be expressed as:

$$\ddot{\sigma}_{GF,i}(z) = \frac{\rho C_D b I_{u,r} \bar{u}_r^2}{m_i} R K_x \phi_i(z), \quad m_i = \frac{\int_h \mu(z) \phi_i^2(z) dz}{\int_h \phi_i^2(z) dz}, \quad K_x = \frac{\int_h \bar{u}^2(z) \phi_i(z) dz}{\bar{u}_r^2 \int_h \phi_i^2(z) dz}$$



where the subscript  $i$  denotes the vibration mode,  $m_i$  is the equivalent mass per unit height,  $R$  is square root of the background factor,  $I_{u,r} = \sigma_u/\bar{u}_r$  is the turbulence intensity at the reference height, and  $K_x$  is a non-dimensional coefficient. In the equivalent mass per unit height  $m_i$ ,  $\mu$  is the mass per unit height.

#### 4.6 Mode shapes

From the modal analysis of the frames, the fundamental mode shape  $\phi_1$  is extracted to be compared with the mode shapes given in NS-EN 1991-1-4:2005 Annex F. The mode shapes given in the Eurocodes are of the form:

$$\phi_1(z) = \left(\frac{z}{h}\right)^\zeta, \quad (4.8)$$

where  $z$  is a vertical coordinate,  $h$  is the building height, and  $\zeta$  is a mode shape parameter. Lower values of the mode shape parameter  $\zeta$  indicates soft buildings, whereas higher values indicate rigid buildings. From the modal analysis, the discrete points of the fundamental mode shapes are fitted to the same format of the Eurocodes using a built-in MATLAB function utilizing the Levenberg-Marquardt nonlinear least squares algorithm.



## 5 Results and discussion

In this chapter, the results of the simulations and computations in this thesis are presented and discussed. First, the results from the parameter study of the reference frame are presented and briefly discussed in the form of accelerations and displacements. Second, the results from the simulations are presented and discussed in the form of histograms, error maps, and correlation plots. Third, results from the nonlinear regression of the simulations with respect to natural frequencies, frequency reduction factor, accelerations, and displacements are presented and discussed. Fourth, results from the simulations are compared with serviceability requirements in ISO 10137-2007. Fifth, results from the gust factor simulations regarding the effect of mass location and amount are presented and discussed. Sixth, limitations of the results in this thesis are discussed.

### 5.1 Reference frame

In the following figures, each parameter in the reference frame is varied individually. The results show the sensitivity of the accelerations and displacements to the different parameters.

**Figure 9** shows the displacements and accelerations for varying floor heights. Observe that the displacements follow an exponential trend, and the accelerations a linear trend. In the displacements, the gust factor approach seems to trail the lower limit of the simulated generalized wind load. In the accelerations, the gust factor approach appears to start above the ensemble average of the simulated generalized wind load and ending below. The floor height is a more important parameter for the displacements than the accelerations.

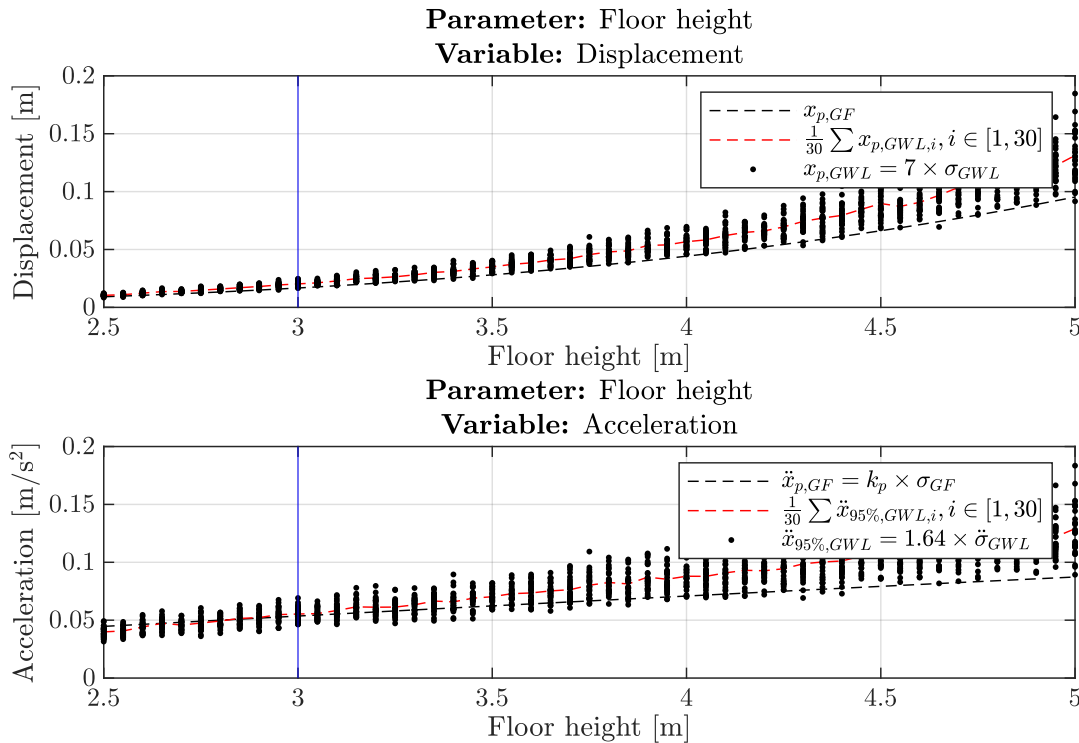


Figure 9 Displacements and accelerations for the gust factor approach (black dashed line) and generalized wind loading (dots). The simulations are for the reference frame with varying floor heights. The reference value for the parameter is shown in the blue solid line.

**Figure 10** shows the displacements and accelerations for varying floor numbers. Observe that the displacements follow an exponential trend, and the accelerations a linear trend. In the displacements, the gust factor approach seems to trail the lower limit of the simulated generalized wind load, with the two diverging for higher floor numbers. In the accelerations, the gust factor approach appears to start below the simulated generalized wind load and ending slightly above the ensemble average. The number of floors is similar in importance for the displacements and the accelerations.

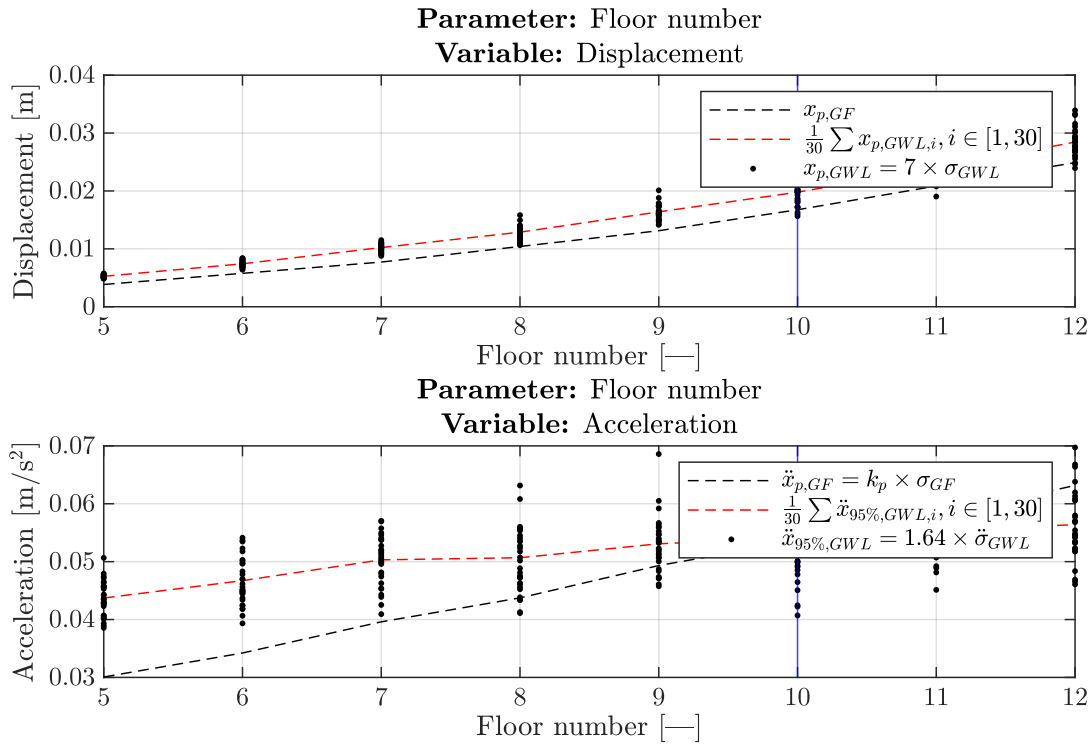


Figure 10 Displacements and accelerations for the gust factor approach (black dashed line) and generalized wind loading (dots). The simulations are for the reference frame with varying floor numbers. The reference value for the parameter is shown in the blue solid line.

**Figure 11** shows the displacements and accelerations for varying vertical loads. Observe that the displacements follow a weak linear trend, and the accelerations an inverse exponential trend. In the displacements, the gust factor approach seems to trail the lower limit of the simulated generalized wind load. In the accelerations, the gust factor approach appears to start slightly below the ensemble average of the simulated generalized wind load and ending slightly above. The load is a more important parameter for the accelerations than the displacements.

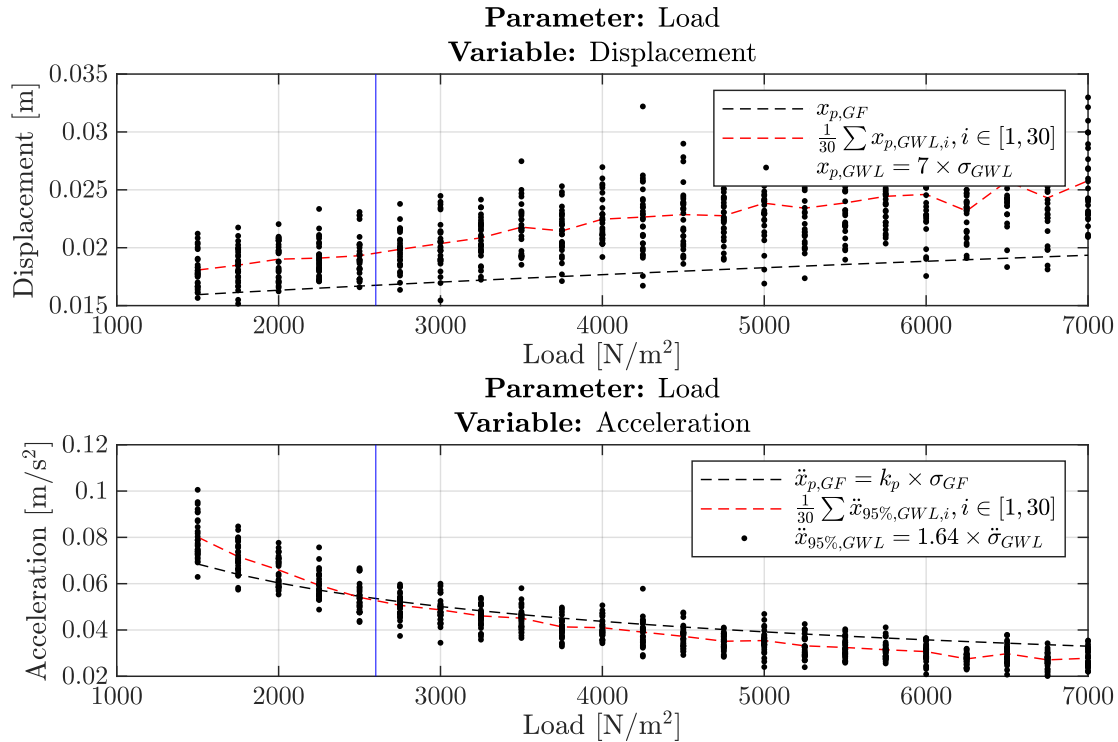


Figure 11 Displacements and accelerations for the gust factor approach (black dashed line) and generalized wind loading (dots). The simulations are for the reference frame with varying floor numbers. The reference value for the parameter is shown in the blue solid line.

**Figure 12** shows the displacements and accelerations for varying beam stiffnesses. Observe that the displacements follow an inverse exponential trend, and the accelerations a weak inverse exponential trend. In the displacements, the gust factor approach seems to trail the lower limit of the simulated generalized wind load. In the accelerations, the gust factor approach appears to follow the ensemble average of the simulated generalized wind load. The beam stiffness is a parameter that is equally important for both the displacements and accelerations.

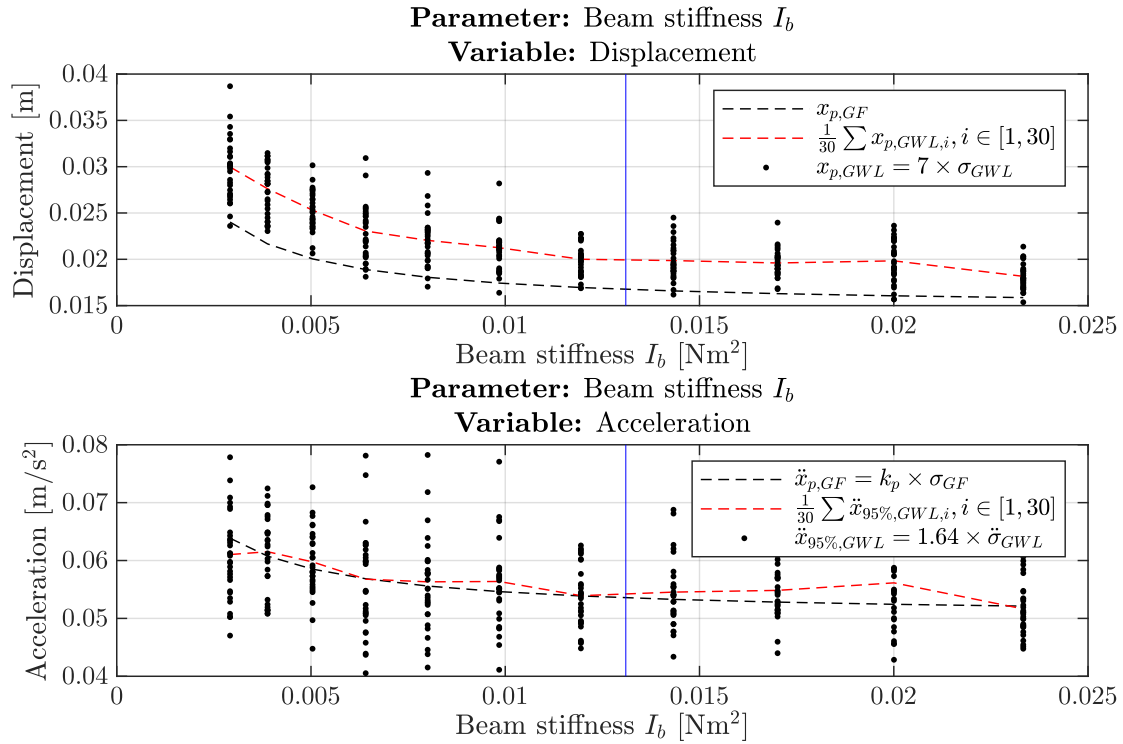


Figure 12 Displacements and accelerations for the gust factor approach (black dashed line) and generalized wind loading (dots). The simulations are for the reference frame with varying beam stiffnesses. The reference value for the parameter is shown in the blue solid line.

**Figure 13** shows the displacements and accelerations for varying column stiffnesses. Observe that the displacements follow an inverse exponential trend. The accelerations for the gust factor approach follow an inverse exponential trend, whilst the accelerations for the generalized wind load appear to follow a constant trend. In the displacements, the gust factor approach seems to trail the lower limit of the simulated generalized wind load. In the accelerations, the gust factor approach appears to start slightly above the ensemble average of the simulated generalized wind load and ending slightly below. The column stiffness is a more important parameter for the displacements than the accelerations.

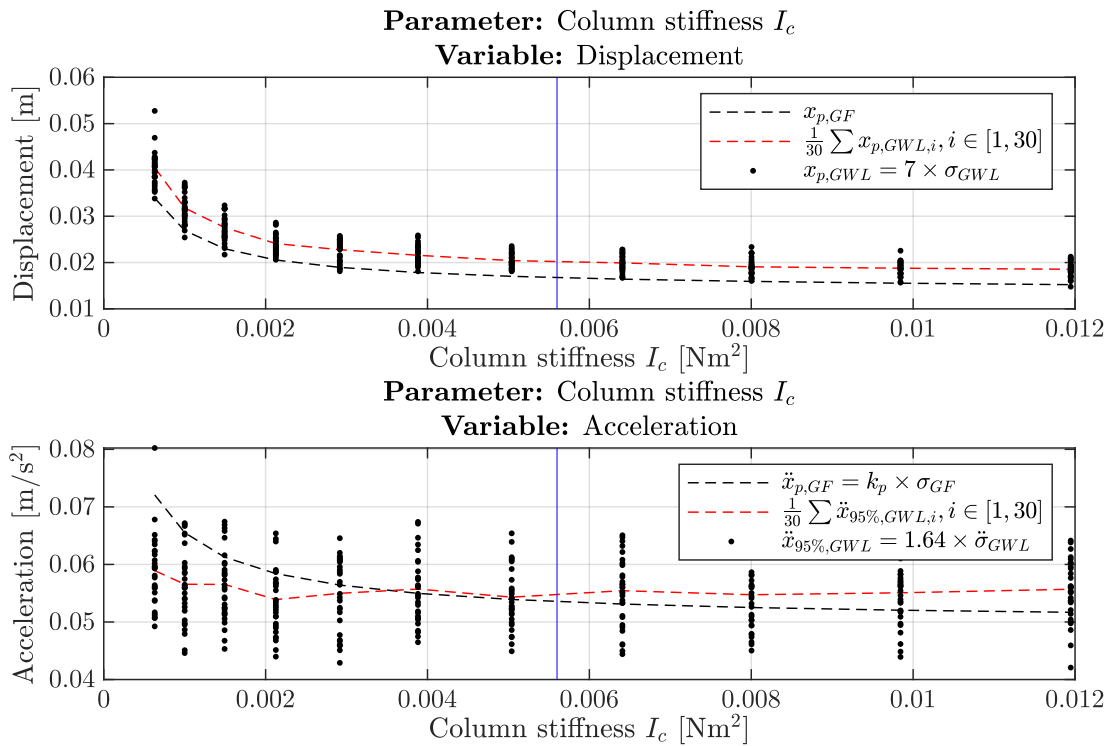


Figure 13 Displacements and accelerations for the gust factor approach (black dashed line) and generalized wind loading (dots). The simulations are for the reference frame with varying column stiffnesses. The reference value for the parameter is shown in the blue solid line.

**Figure 14** shows the displacements and accelerations for varying rotational beam-to-column stiffnesses. Observe that both the displacements and accelerations follow an inverse exponential trend. In the displacements, the gust factor approach seems to trail the lower limit of the simulated generalized wind load. In the accelerations, the gust factor approach appears to start above the ensemble average of the simulated generalized wind load and ending slightly below. The rotational stiffness is a more important parameter for the displacements than the accelerations.

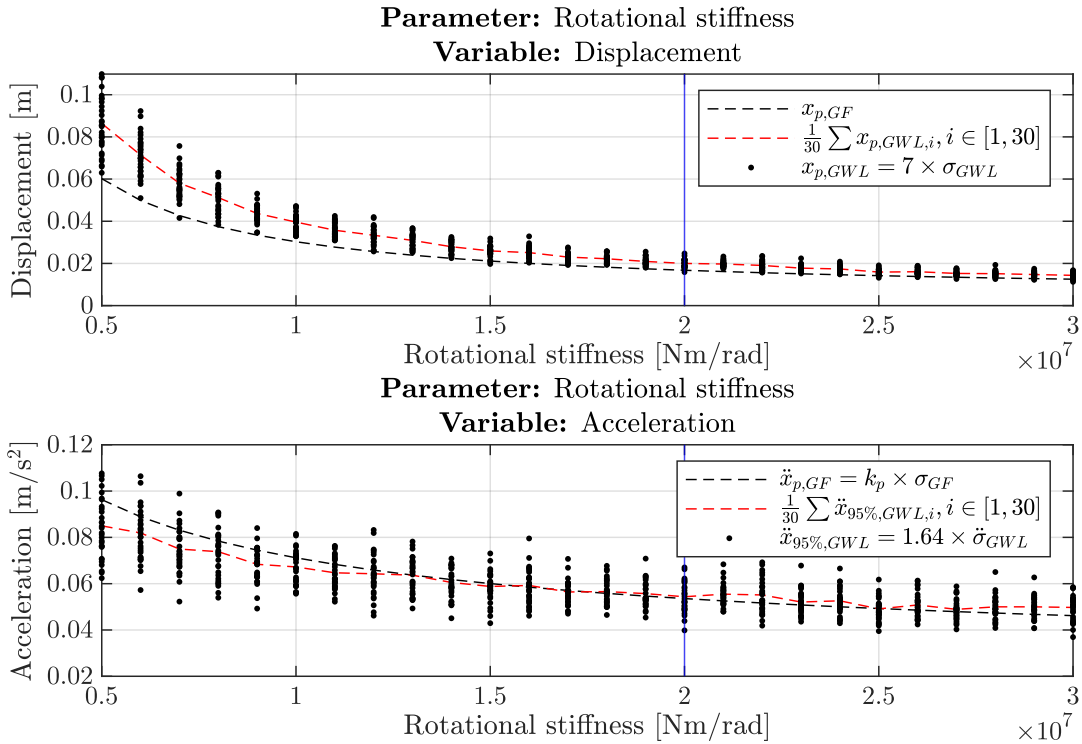


Figure 14 Displacements and accelerations for the gust factor approach (black dashed line) and generalized wind loading (dots). The simulations are for the reference frame with varying rotational beam-to-column stiffnesses. The reference value for the parameter is shown in the blue solid line.



**Figure 15** shows the displacements and accelerations for varying rotational support stiffnesses. Observe that the displacements follow a weak inverse exponential trend, and the accelerations a weak linear trend. In the displacements, the gust factor approach seems to trail the lower limit of the simulated generalized wind load. In the accelerations, the gust factor approach appears to be slightly below the ensemble average of the simulated generalized wind load. The rotational support stiffness is a more important parameter for the displacements than the accelerations.

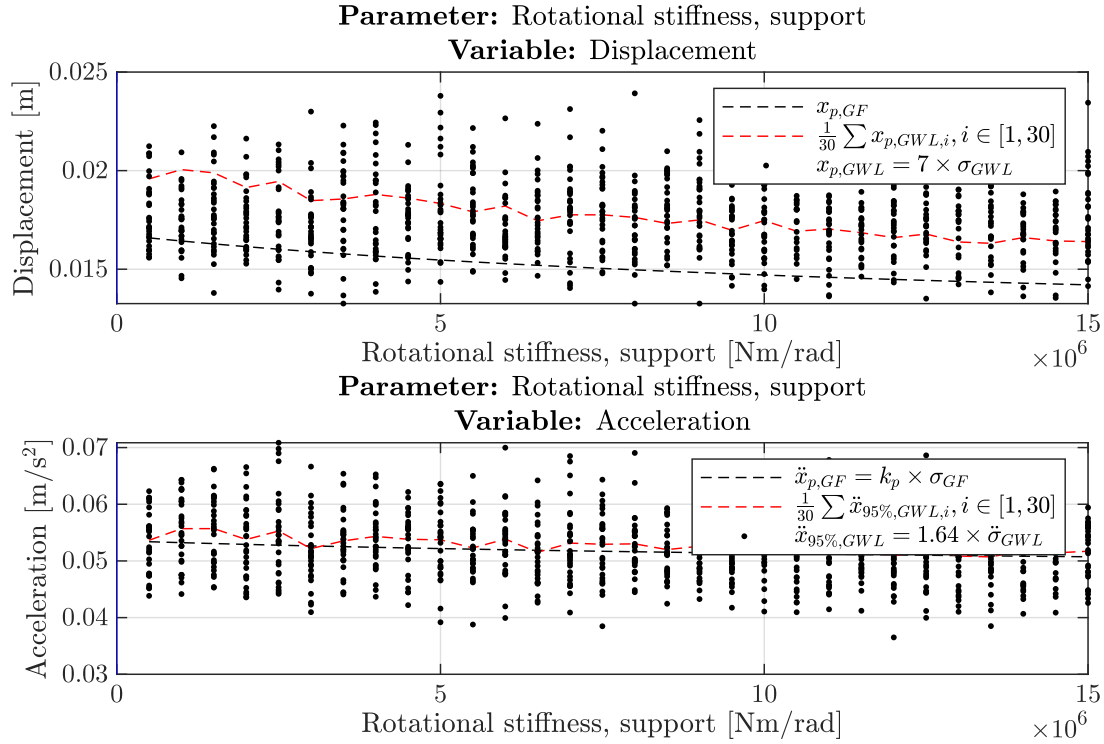


Figure 15 Displacements and accelerations for the gust factor approach (black dashed line) and generalized wind loading (dots). The simulations are for the reference frame with rotational support stiffnesses. The reference value for the parameter is shown in the blue solid line.

**Figure 16** shows the displacements and accelerations for varying horizontal support stiffnesses. Observe that the displacements follow a weak inverse exponential trend, and the accelerations a constant trend. In the displacements, the gust factor approach seems to trail the lower limit of the simulated generalized wind load. In the accelerations, the gust factor approach appears to be slightly above the ensemble average of the simulated generalized wind load. The horizontal support stiffness is a more important parameter for the displacements than the accelerations, but it is of small importance in general.

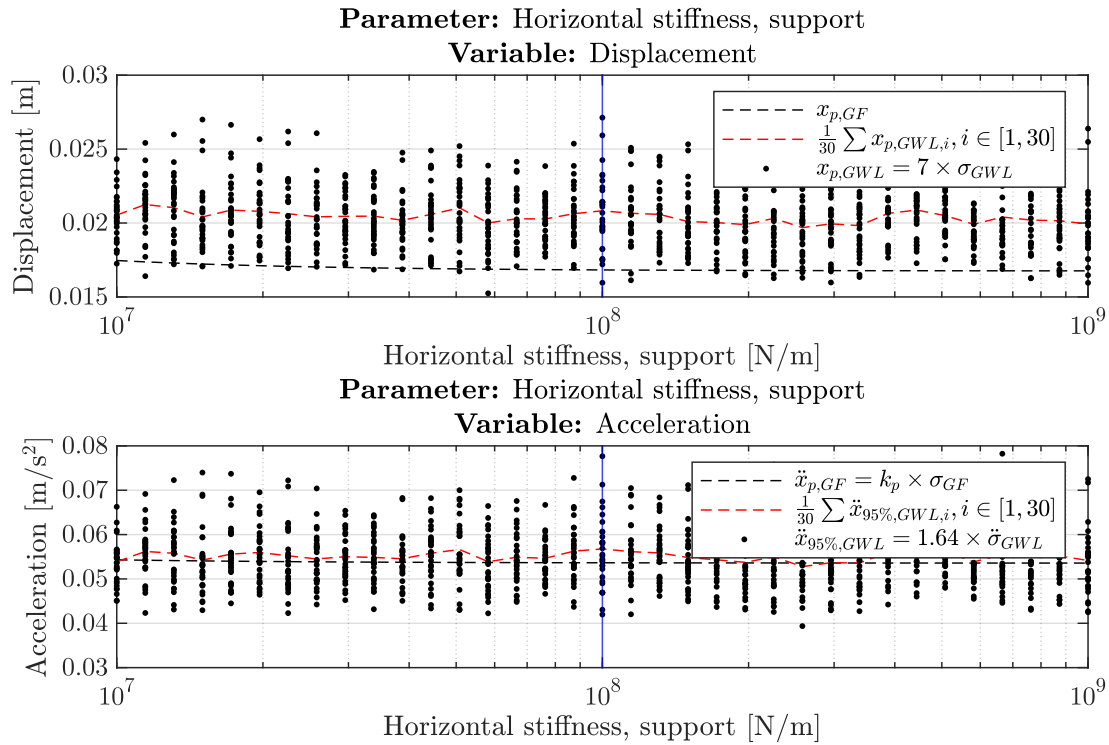


Figure 16 Displacements and accelerations for the gust factor approach (black dashed line) and generalized wind loading (dots). The simulations are for the reference frame with varying horizontal support stiffnesses. The reference value for the parameter is shown in the blue solid line.

**Figure 17** shows the displacements and accelerations for varying vertical support stiffnesses. Observe that the displacements and accelerations follow an inverse exponential trend. In the displacements, the gust factor approach seems to trail the lower limit of the simulated generalized wind load. In the accelerations, the gust factor approach appears to be slightly above the ensemble average of the simulated generalized wind load with convergence towards higher vertical support stiffnesses. The vertical support stiffness is a more important parameter for the displacements than the accelerations.

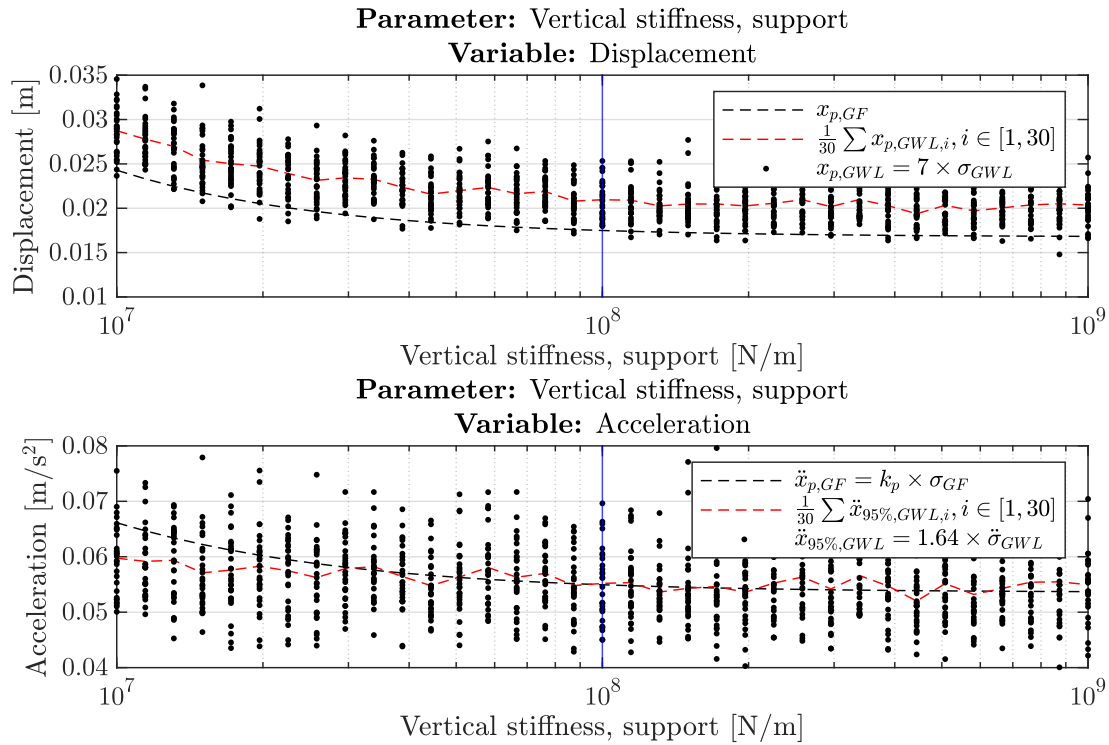


Figure 17 Displacements and accelerations for the gust factor approach (black dashed line) and generalized wind loading (dots). The simulations are for the reference frame with varying vertical support stiffnesses. The reference value for the parameter is shown in the blue solid line.

**Figure 18** shows the displacements and accelerations for varying number of bays. Observe that the displacements and accelerations follow an inverse exponential trend. In the displacements, the gust factor approach seems to trail the lower limit of the simulated generalized wind load, with convergence for higher number of bays. In the accelerations, the gust factor approach appears to start slightly below the ensemble average of the simulated generalized wind load and ending below. The number of bays is almost of equal importance for the displacements and the accelerations.

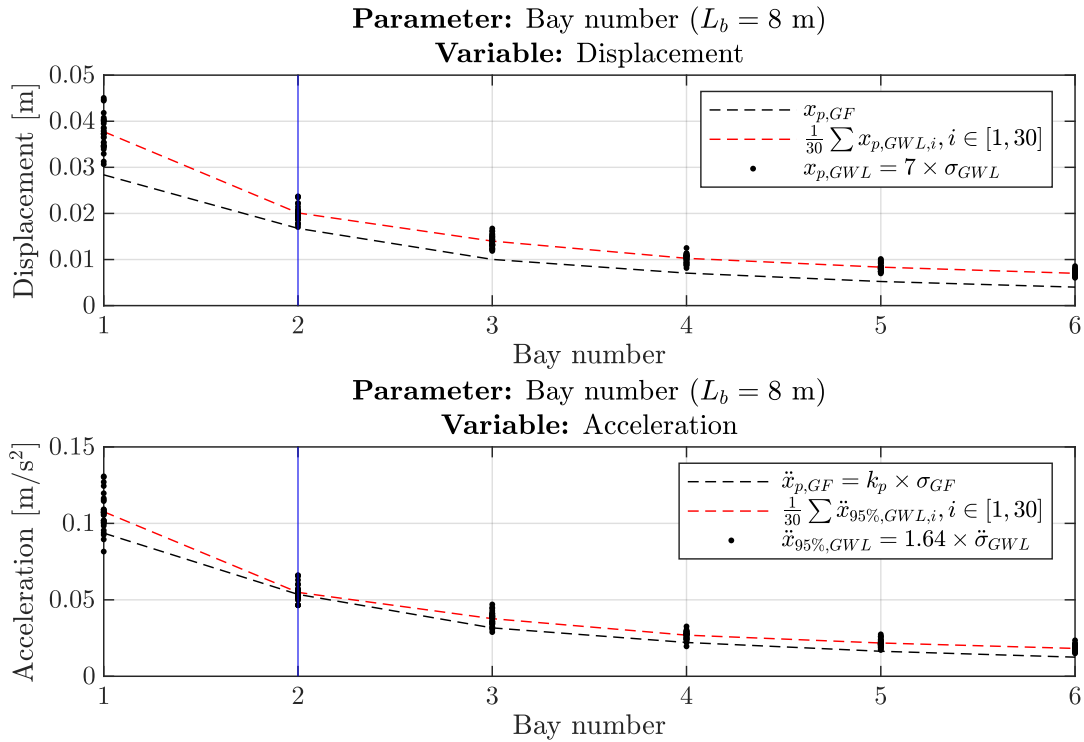


Figure 18 Displacements and accelerations for the gust factor approach (black dashed line) and generalized wind loading (dots). The simulations are for the reference frame with varying bay numbers. The reference value for the parameter is shown in the blue solid line.

**Figure 19** shows the displacements and accelerations for varying beam or bay lengths. Observe that both the displacements and accelerations follow a linear trend. In the displacements, the gust factor approach seems to trail the lower limit of the simulated generalized wind load. In the accelerations, the gust factor approach appears to start slightly below the ensemble average of the simulated generalized wind load with convergence for longer beam lengths. The beam length is a more important parameter for the accelerations than the displacements.

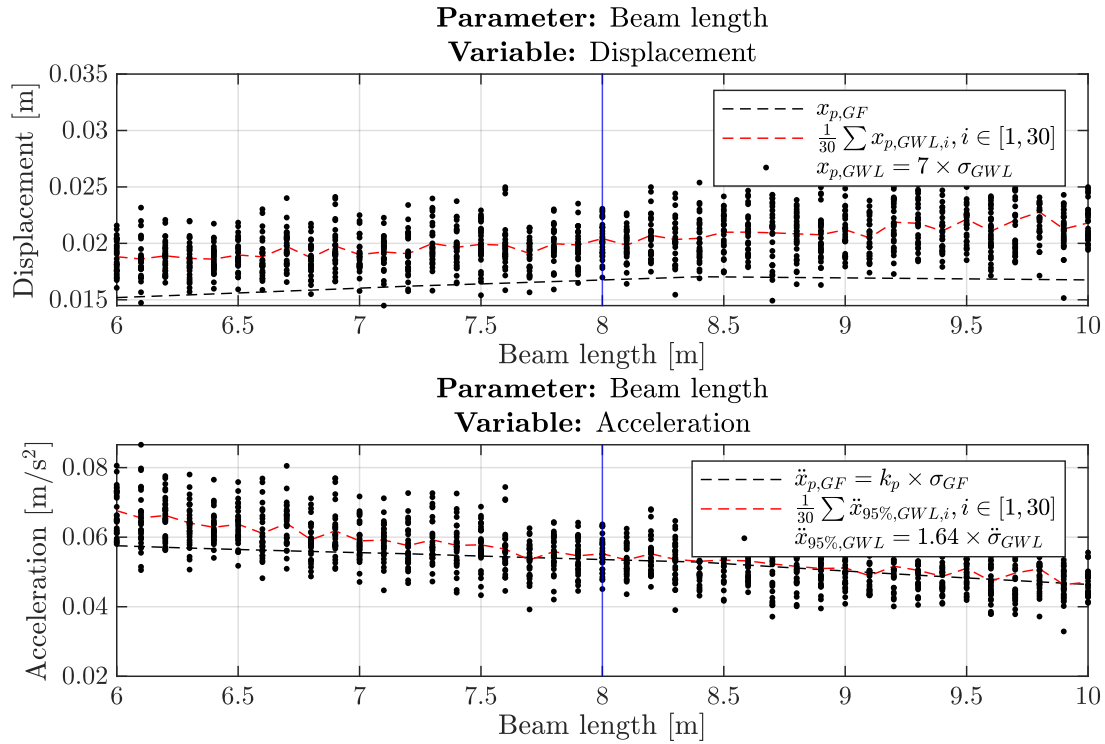


Figure 19 Displacements and accelerations for the gust factor approach (black dashed line) and generalized wind loading (dots). The simulations are for the reference frame with varying beam lengths. The reference value for the parameter is shown in the blue solid line.

**Figure 20** shows the displacements and accelerations for varying damping ratios. Observe that both the displacements and accelerations follow a weak inverse exponential trend, with the displacements almost following a negative linear trend. In the displacements, the gust factor approach seems to trail the lower limit of the simulated generalized wind load. In the accelerations, the gust factor approach appears to follow the ensemble average of the simulated generalized wind load. The damping ratio is a more important parameter for the accelerations than the displacements.

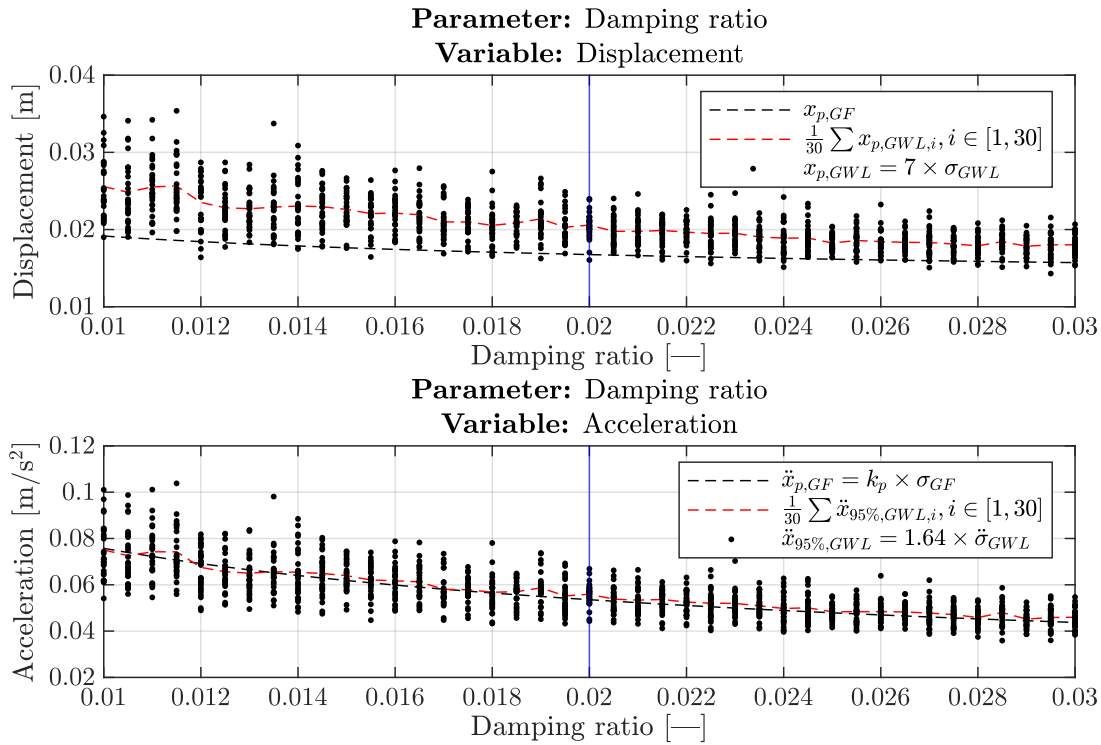


Figure 20 Displacements and accelerations for the gust factor approach (black dashed line) and generalized wind loading (dots). The simulations are for the reference frame with varying damping ratios. The reference value for the parameter is shown in the blue solid line.

**Table 10** shows a qualitative overview of the different trends, effects, significance, and flexibility of the different parameters in the parameter study. The parameters with the highest significance on the displacements are the floor height, floor number, rotational connection stiffness and number of bays. The parameters with the lowest significance on the displacements are the load, and horizontal support stiffness. The parameters with the highest significance on the accelerations are the floor height, floor number, load, rotational connection stiffness, number of bays and damping ratio. The parameters with the lowest significance on the accelerations are the rotational support stiffness, and horizontal support stiffness.

In **Table 10**, there is also a column called *parameter flexibility*. The parameter flexibility is a qualitative assessment of the ease or freedom of the structural engineer to change the values of the parameters based on architectural plans and physical in-situ conditions. As an example, it is more difficult to change the soil parameters than to change the column or beam stiffnesses. If architects have already envisioned and fixed the number of floors and floor height, it may not be within the

scope of the structural engineer to change these parameters. However, the connection stiffnesses or other structural parameters can be changed to cope with the parameters with low flexibility.

Parameter	Trend, displacements	Trend, accelerations	Displacements		Accelerations		Parameter flexibility
			Effect	Significance	Effect	Significance	
Floor height	Linear	Exponential	+	High	+	High	Low
Floor number	Exponential	Linear	+	High	+	High	Low
Load	Linear	Inverse exponential	+	Low	-	High	Medium
Beam stiffness	Inverse exponential	Inverse exponential	-	Medium	-	Medium	High
Column stiffness	Inverse exponential	Inverse exponential	-	Medium	-	Medium	High
Rotational stiffness	Inverse exponential	Inverse exponential	-	High	-	High	High
Rotational support stiffness	Inverse exponential	Linear	-	Medium	-	Low	Medium
Horizontal support stiffness	Inverse exponential	Constant	-	Low	-	None	Low
Vertical support stiffness	Inverse exponential	Inverse exponential	-	Medium	-	Medium	Low
Bay number	Inverse exponential	Inverse exponential	-	High	-	High	Medium
Beam length	Linear	Linear	+	Medium	-	Medium	Medium
Damping ratio	Inverse exponential	Inverse exponential	-	Medium	-	High	Low

*Table 10 Qualitative observations of the trends, effects, significance, and flexibility of the different parameters on the displacements and accelerations. In this context, flexibility denotes the freedom for the structural engineer to change the values of the parameters based on architectural plans and physical in-situ conditions. The effect is given in positive change (+), and negative change in the numerical values of the accelerations and displacements.*

In general, the gust factor approach results in smaller displacements than the generalized wind load. For some of the parameters, the gust factor approach results in a smaller acceleration than the generalized wind load. If compared with the generalized wind load, the gust factor approach may result in nonconservative design in some cases for the displacements, and nonconservative design in most cases for the accelerations.

## 5.2 Simulations

In this section, the data from the simulations are presented and overall observations are made. The data is visualized in terms of histograms, and the most suitable probability density functions are fitted to the data. For the accelerations and displacements, deviation maps showing the percent bias, and correlation plots between the gust factor approach and the generalized wind load are shown.

### 5.2.1 Natural frequency

**Figure 21** shows a histogram and a log-normal probability density function for the natural frequencies of all the simulated frames. Observe that the median of the natural frequencies  $f_n$  is around 0.4 Hz. Very few frames have a natural frequency above 1.0 Hz. For structures of the same size in concrete or steel, the natural frequency should be in the range between 1 Hz and 2 Hz. The median of the simulated natural frequencies is equivalent to structures in steel or concrete that are about 100 m tall according to the Eurocodes. The tallest case that is simulated in this thesis is 40 m.

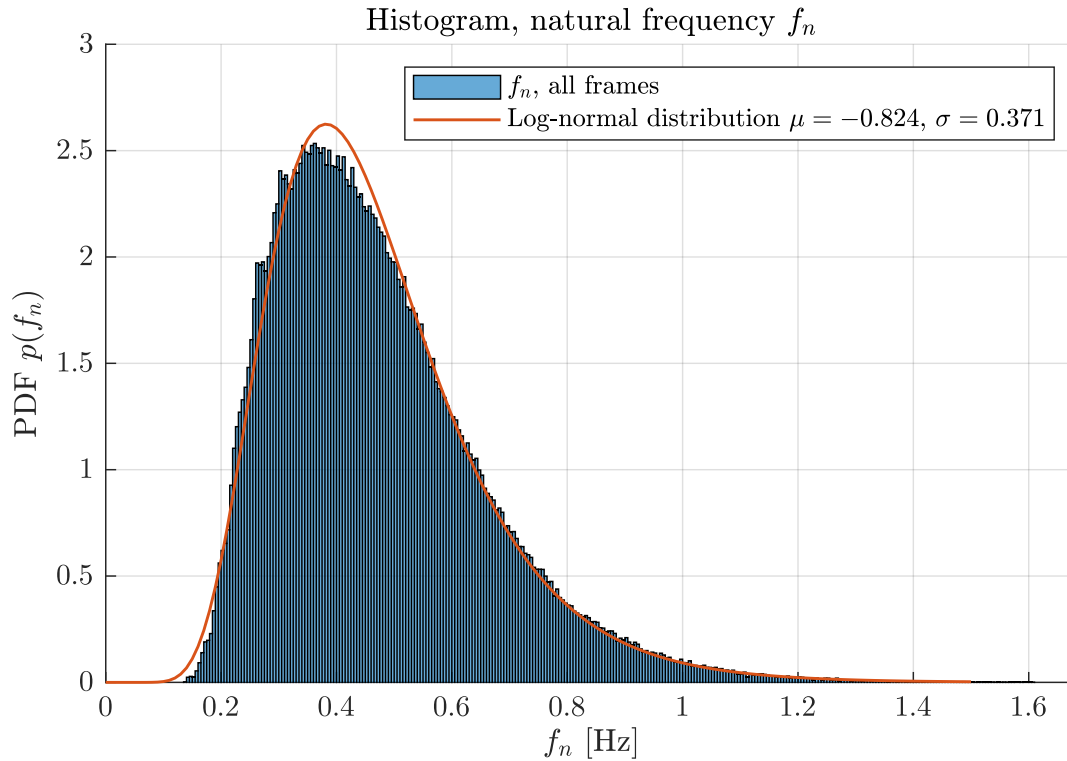


Figure 21 Histogram and log-normal probability density function for the natural frequencies of all the simulated frames.

**Figure 22** shows a histogram and a log-normal probability density function for the natural frequencies  $f_n$  of all the simulated frames, together with the non-dimensional power spectral density for turbulent winds from NS-EN 1991-1-4:2005 Annex B. Observe that the peak is concentrated at a natural frequency  $f_n$  of 0.44 Hz. The natural frequency  $f_n$  is a function of stiffness and mass. The log-normal distribution fit the simulations well.



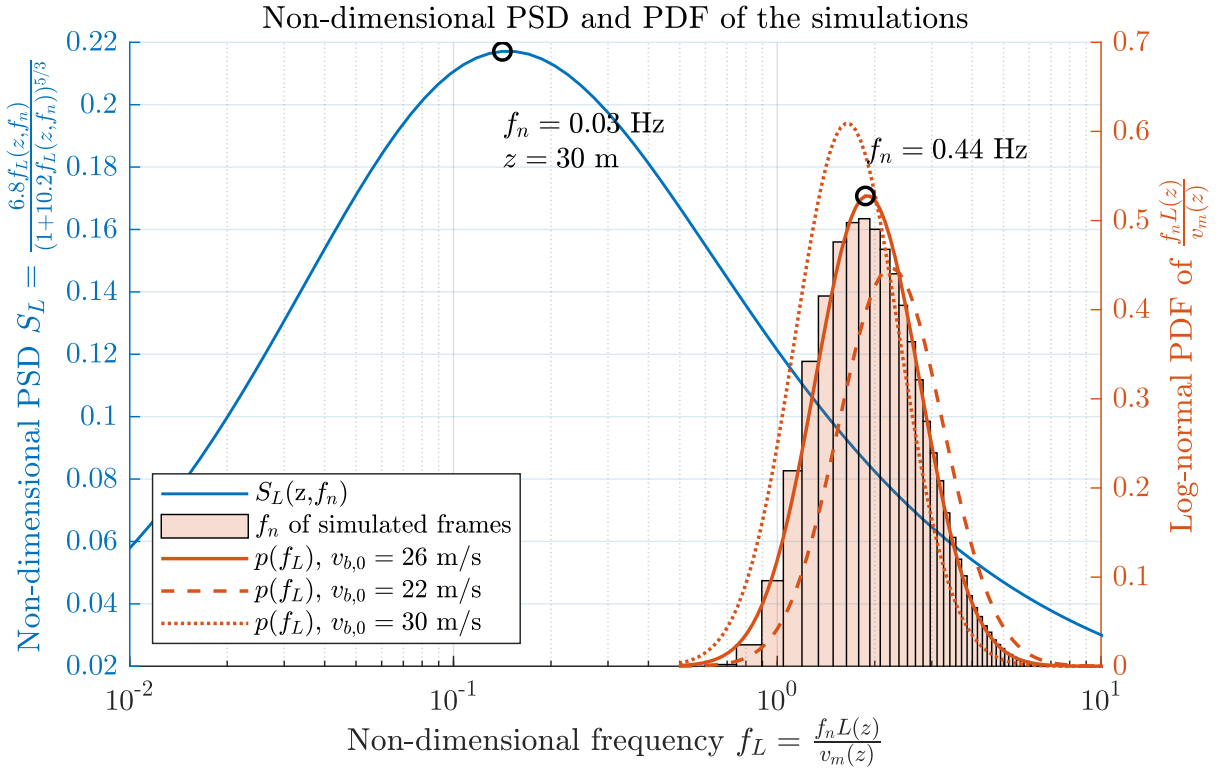


Figure 22 Histogram and log-normal probability density function for the natural frequencies of all the simulated frames (right), together with the non-dimensional power spectral density for turbulent winds from NS-EN 1991-1-4:2005 Annex B.

Observe that the peaks for the power spectral density and the probability density functions for different wind velocities occur at different frequencies. However, for larger wind velocities, the peak of the frames moves towards the peak of the power spectral density. According to the logarithmic law of the mean wind velocity in **Equation 3.9**, the wind velocity is zero at the ground surface. At the ground surface, the turbulence intensity  $I_u$  is infinite, and the turbulent length scale is zero. As the distance from the ground surface increases, the mean wind velocity increases, the turbulence intensity decreases, and the turbulent length scale increases.

As the turbulent length scale increases, the structure absorbs more of the wind gusts due to the increasing correlation between the structure size and the size of the turbulence eddies. This phenomenon explains the reason for why the peaks approach each other with higher mean wind velocities. However, most values of the basic wind velocity  $v_{b,0}$  are above 30 m/s. Even for the most intense tropical cyclones with basic wind velocities  $v_{b,0}$  of more than 60 m/s, the peaks for the simulated frames do not coincide with the peak of the wind spectrum.

As the peaks approach each other, the dynamic amplification increases. For an undamped system, the dynamic amplification will become infinite if the peaks coincide. This will result in infinitely large responses in the form of displacement, velocity, and acceleration. For the design of any structure, the natural frequencies must be separated as far away from the peak of the power spectral density as possible to avoid severe effects of dynamic amplification.

Some existing structures have a very low natural frequency which is very close to the peak in the shown spectrum in **Figure 22**. For a building with 100 floors, the natural frequency  $f_n$  is typically in

the range between 0.1 Hz and 0.125 Hz. For some super-tall structures, the natural frequency  $f_n$  is 0.05 Hz (Irwin, 2010). Timber structures will likely reach such ranges in the natural frequency  $f_n$  for much lower heights.

### 5.2.2 Mode shape parameter

**Figure 23** shows a histogram and a logistic probability density function for the mode shape parameter  $\zeta$  of all the simulated frames. The mode shape parameter is a function of stiffness and mass. The logistic distribution does not represent the median or the lower values of the mode shape parameter  $\zeta$  well. Observe that the peak is concentrated at a mode shape parameter of about 0.63.

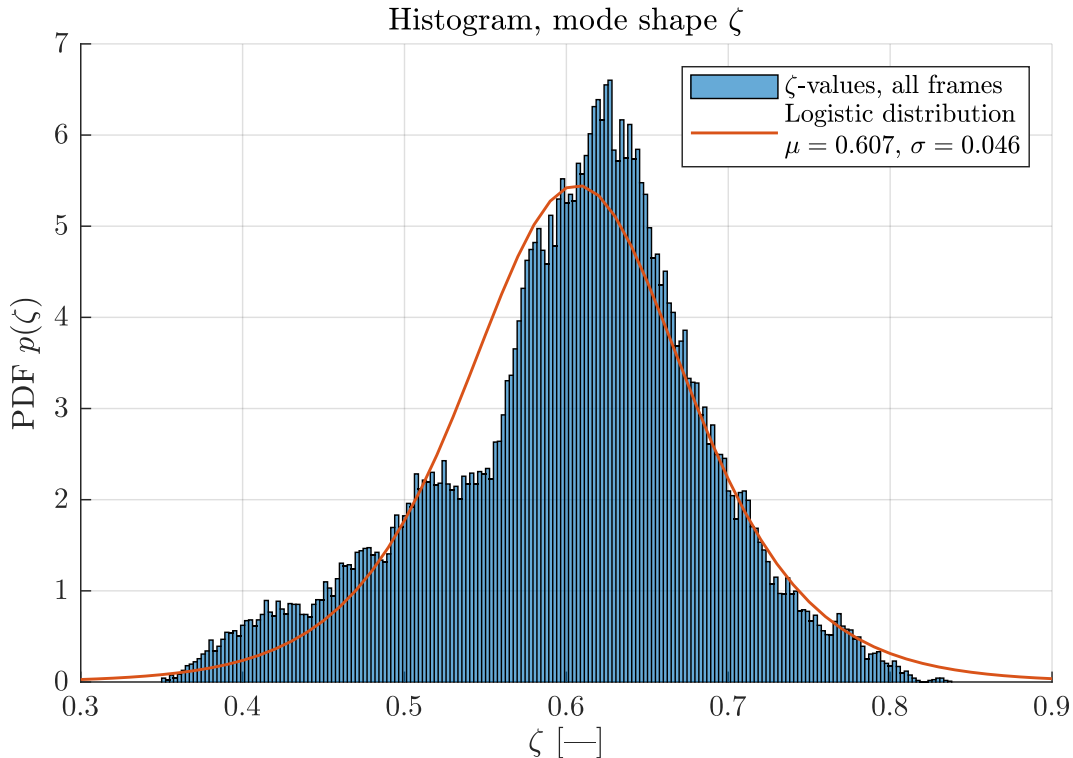


Figure 23 Histogram and logistic probability density function for the mode shapes of all the simulated frames.

**Table 11** shows the description by the Eurocodes of the mode shape parameter  $\zeta$ . Observe that more than half of all the simulated frames have a mode shape parameter that is softer than the softest value  $\zeta = 0.6$  given in the Eurocodes. None of the simulated frames have a mode shape parameter that is higher than  $\zeta = 0.9$ , indicating that the simulated frames are soft. The structural type is in good agreement with **Table 11**.

Mode shape parameter	Description	Stiffness
$\zeta = 0.6$	Slender structures with non load-sharing walling or cladding	Soft
$\zeta = 1.0$	Buildings with a central core plus peripheral columns or larger columns plus shear bracings	
$\zeta = 1.5$	Slender cantilever buildings and buildings supported by central reinforced concrete cores	↓
$\zeta = 2.0$	Towers and chimneys	Rigid
$\zeta = 2.5$	Lattice steel towers	

Table 11 Description of the mode shape parameter  $\zeta$  by NS-EN 1991-1-4:2005 Annex F.

The stiffness of the frames can be increased quite easily through the introduction of bracings, load-sharing walls, and a central core. However, these types of structures are outside the scope of this thesis and should be subject for future investigations into this topic.

### 5.2.3 Accelerations

**Figure 24** shows a histogram and a log-normal probability density function for the response accelerations of all the simulated frames for the gust factor approach and the simulations of the generalized wind load. Observe that the gust factor approach results in lower accelerations than the generalized wind load. The generalized wind load has a heavier tail. The log-normal distributions fit the simulations well.

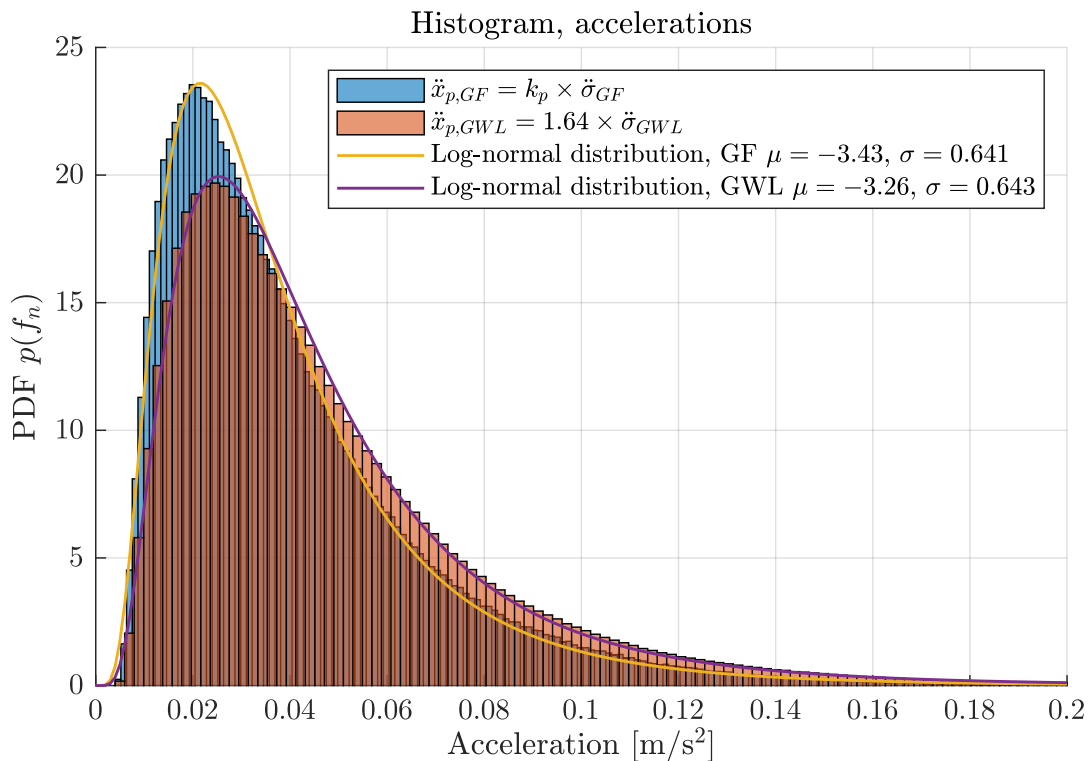


Figure 24 Histograms and log-normal probability density functions for the accelerations of all the simulated frames.

**Figure 25** shows a deviation map of the response accelerations between the gust factor approach and the generalized wind load, where darker colors indicate higher concentrations of simulated frames. Observe that the highest concentration is between a natural frequency  $f_n$  of 0.3 Hz and 0.5 Hz with a percent bias between +15% and -25%. Observe that higher natural frequencies result in a larger spread in the percent bias. The largest deviations are for the lightest and most flexible frames.

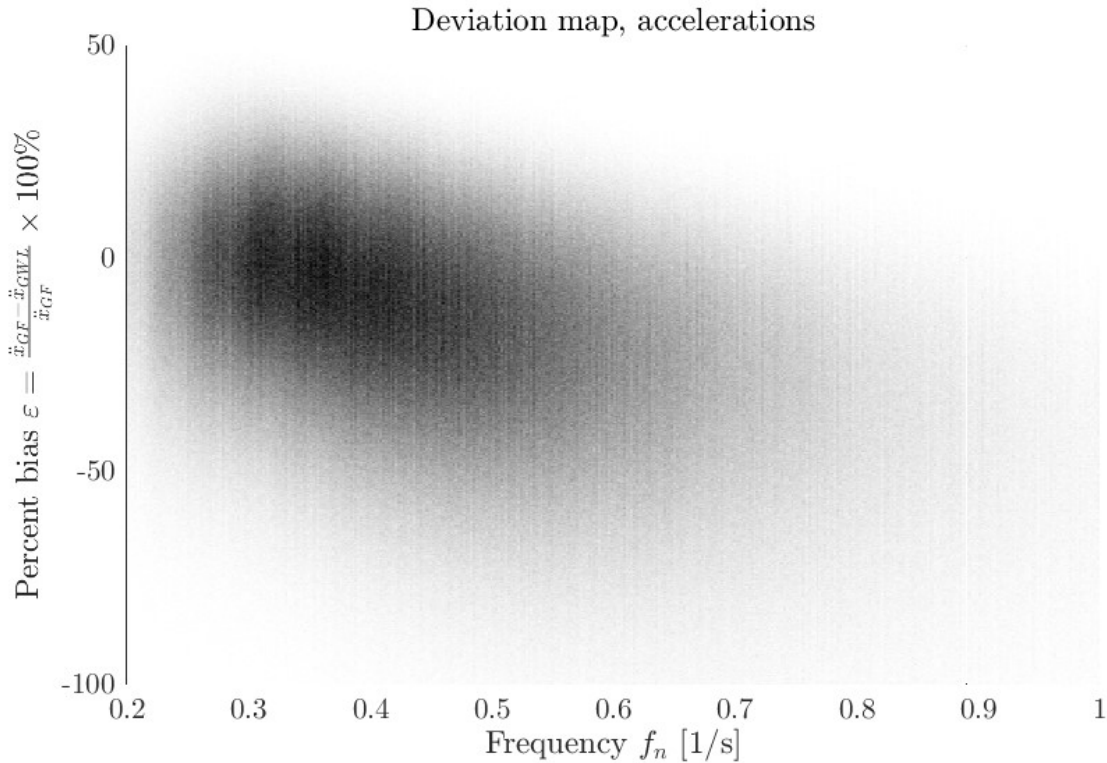


Figure 25 Deviation map of the accelerations of the gust factor approach and the generalized wind load. Darker colors indicate higher concentrations of frames.

**Figure 26** shows a histogram of the deviation between the response accelerations of the gust factor approach and the generalized wind load for different surface loads  $p_s$ . The surface loads  $p_s$  are synonymous with the weight of the structure. For a surface load  $p_s$  of  $1600 \text{ N/m}^2$ , the deviation between the gust factor approach and the generalized wind load is the largest, where the gust factor approach is clearly nonconservative compared with the generalized wind load. This is the lightest case in this thesis and is equivalent to a quasi-static load combination with a self-weight of  $1 \text{ kN/m}^2$  and a live load of  $2 \text{ kN/m}^2$ . This is also the absolute lightest case for the Woodsol deck system.

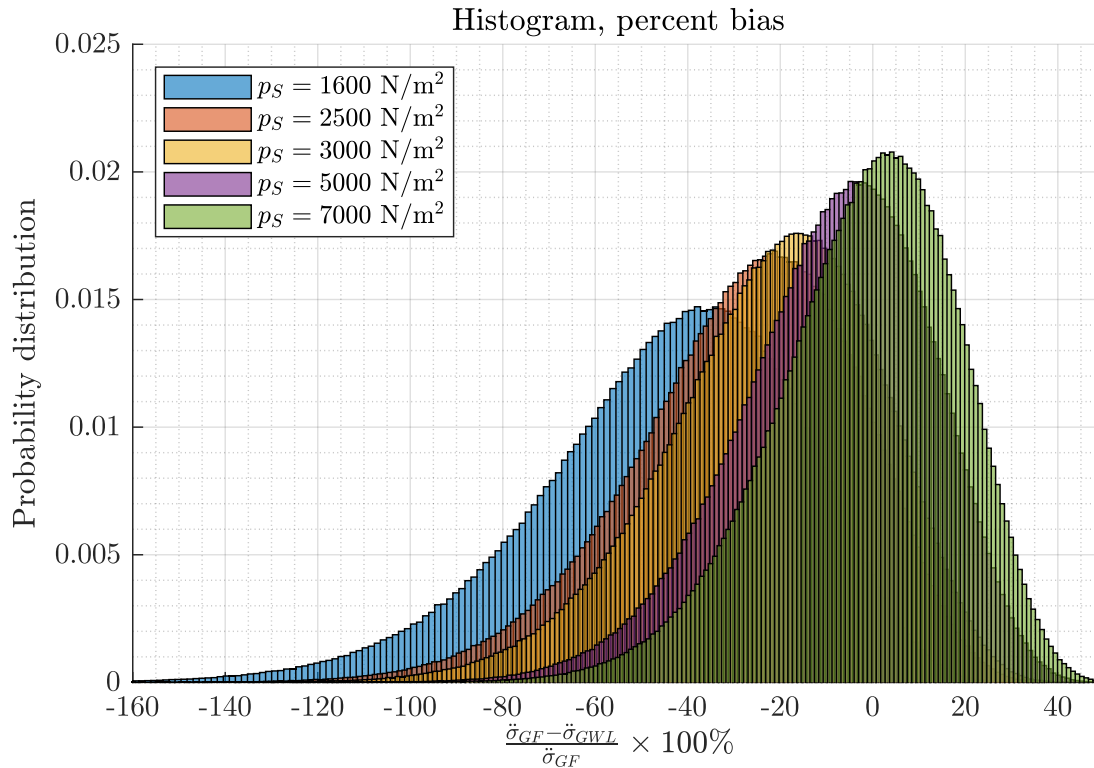


Figure 26 Histogram of the percent bias between response accelerations of the gust factor approach and the generalized wind load for different surface loads.

As the masses increase, the deviations between the gust factor approach and the generalized wind load decrease and the tails become less prominent. The heaviest surface load  $p_S$  of  $7000 \text{ N/m}^2$  has the median of the deviations which is the closest to zero. The quasi-static load combination is more typical for a concrete structure. The surface load  $p_S$  of  $7000 \text{ N/m}^2$  is equivalent to a concrete slab of about  $260 \text{ mm}$ . For this case, the gust factor approach results in mostly conservative accelerations compared with the generalized wind load. In Mjøstårnet, the upper seven floors were built with  $300 \text{ mm}$  concrete slabs (Abrahamsen, 2017), or a quasi-static load combination of  $8100 \text{ N/m}^2$ .

**Figure 27** shows a correlation plot of the response accelerations between the gust factor approach and the generalized wind load. Observe that the Pearson  $R^2$  is  $0.934$ , and that the purple dashed least squares line is above the red line with a unit slope. The figure shows that the generalized wind load generally results in larger accelerations.

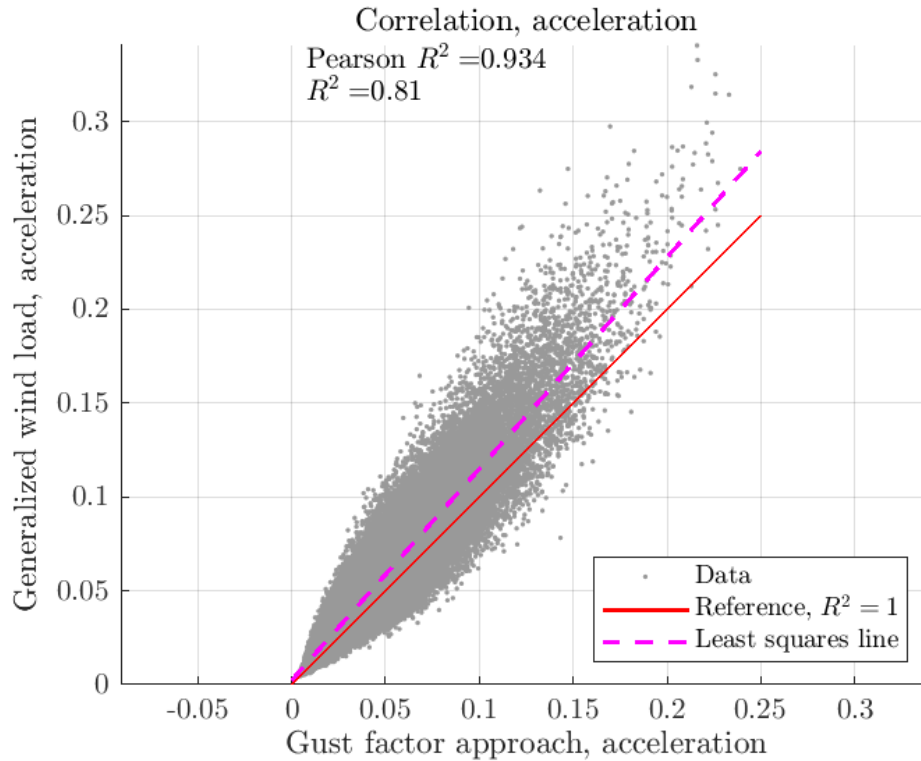


Figure 27 Correlation plot of the response accelerations between the gust factor approach and the generalized wind load. The purple line is the least-squares line of the data. The red line is the reference line for a perfect fit.

#### 5.2.4 Displacements

**Figure 28** shows a histogram and a logistic probability density function for response displacements of all the simulated frames. Observe that the gust factor approach results in smaller displacements than the generalized wind load. The log-normal distributions fit the simulations well. Observe that the generalized wind load has a heavier tail than the gust factor approach.

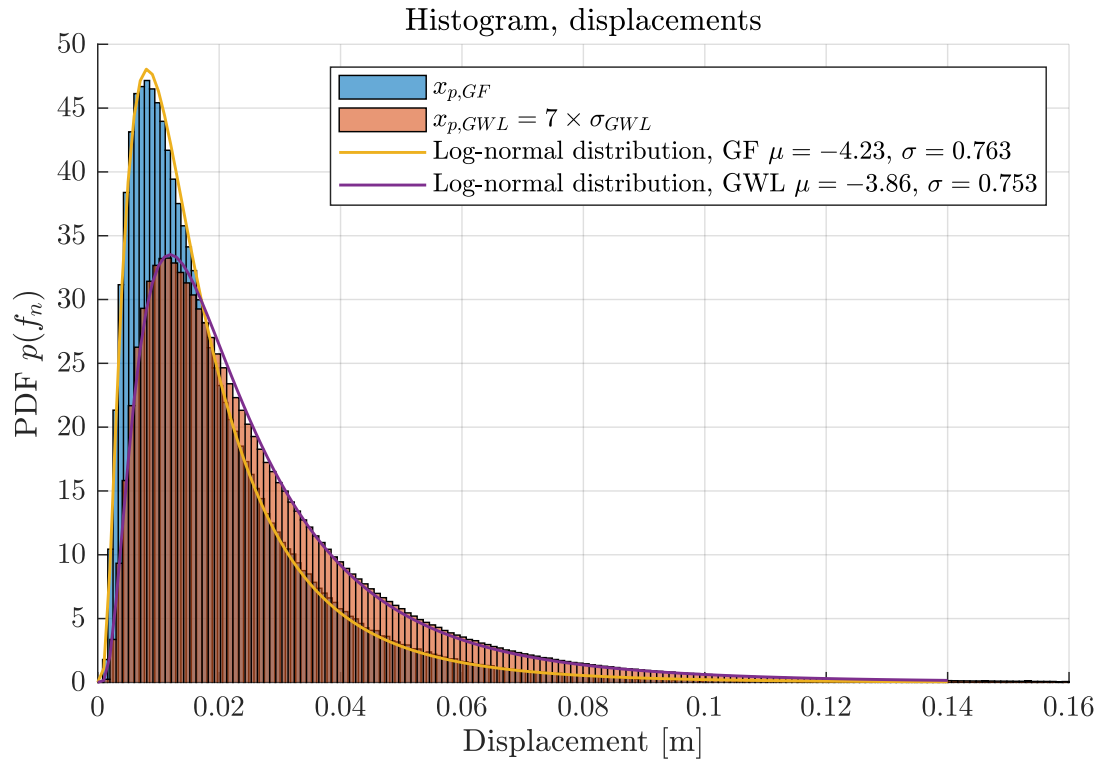


Figure 28 Histograms and log-normal probability density functions for the displacements of all the simulated frames.

**Figure 29** shows a deviation map of the response displacements between the gust factor approach and the generalized wind load, where darker colors indicate higher concentrations of simulated frames. Observe that the highest concentration is between the natural frequencies  $f_n$  of 0.3 Hz and 0.6 Hz with a percent bias from around  $-60\%$  to around  $-20\%$ . The deviation map shows that most of the gust factor displacements are smaller than the displacements in the generalized wind load, resulting in nonconservative displacements. Observe that the trend of the deviations flattens out for larger natural frequencies  $f_n$  at a percent bias of around  $-30\%$ . The deviations for the displacements are larger than the deviations for the accelerations.

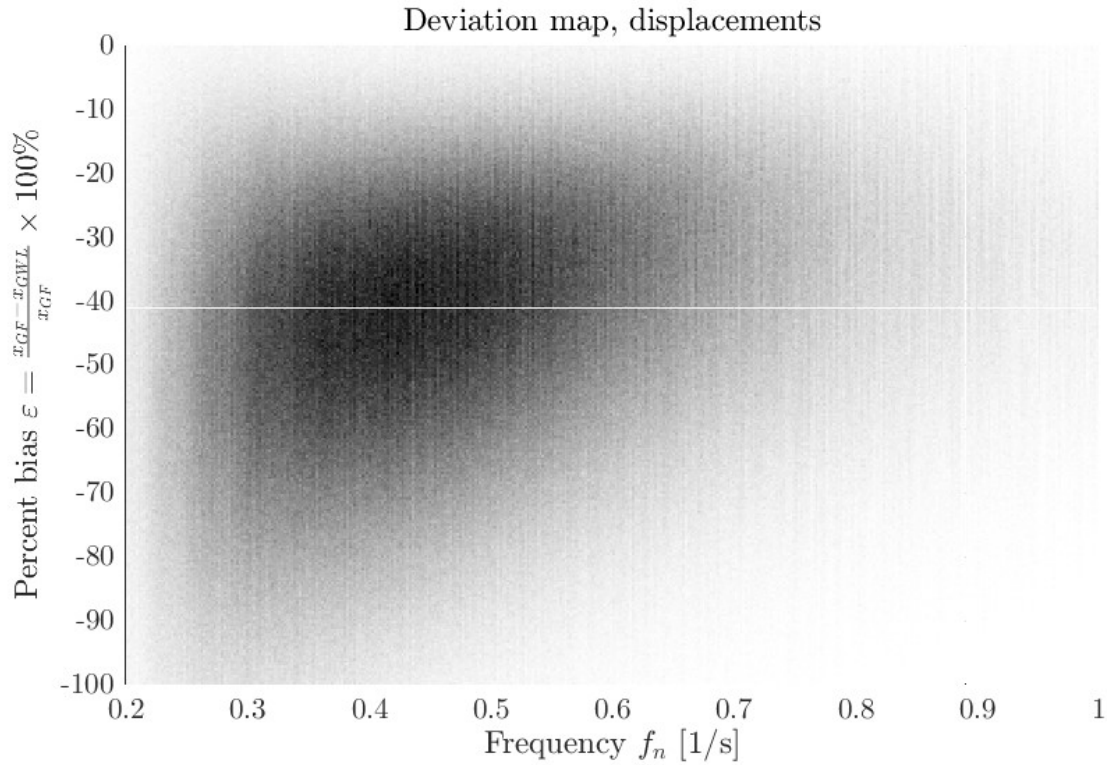


Figure 29 Deviation map of the displacements of the gust factor approach and the generalized wind load. Darker colors indicate higher concentrations of frames.

**Figure 30** shows a correlation plot of the response displacements between the gust factor approach and the generalized wind load. Observe that the Pearson  $R^2$  is high with a value of 0.969. The figure shows that the generalized wind load generally results in larger displacements.



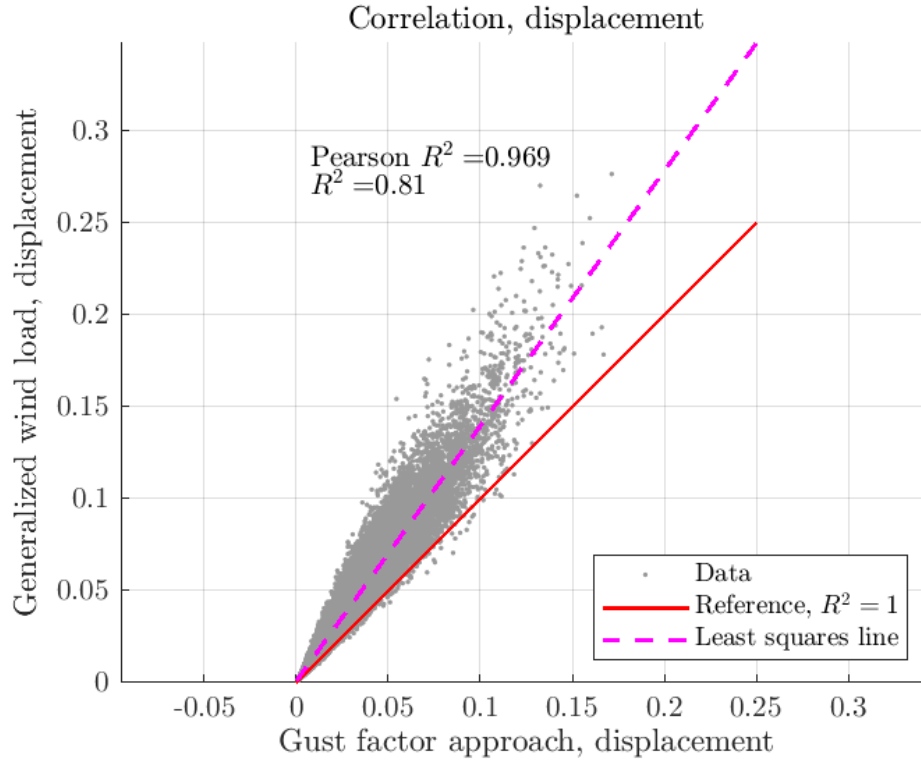


Figure 30 Correlation plot of the response displacements between the gust factor approach and the generalized wind load. The purple line is the least-squares line of the data. The red line is the reference line for a perfect fit.

### 5.3 Nonlinear regression

Nonlinear regressions are performed for the accelerations and displacements for both the gust factor approach, the generalized wind load method, and the natural frequency. The regressions are performed using the Levenberg-Marquardt least squares algorithm on an expression of the following form:

$$y_{\text{pred}} = \prod_{i=1}^{n_p} x_i^{c_i}, \quad (5.3.1)$$

where  $n_p$  is the number of parameters,  $x_i$  is the parameter, and  $c_i$  is an exponent. By using **Equation 5.3.1**, the parameters which are insignificant to the predicted values become obvious. If the coefficients  $c_i$  of the parameters approaches zero, the parameters are insignificant to the predicted values and can be neglected. By eliminating one parameter per iteration of nonlinear regressions, the fit of the expression can be evaluated by investigating the correlation with the simulated values from the gust factor approach and the generalized wind load.

The nonlinear regressions produce expressions that are not dimensionally consistent. The use of the expressions is limited to within the range for which they are calibrated for, and for the same input units.

#### 5.3.1 Natural frequency

The initial nonlinear expression for the regression of the natural frequency  $f_n$  is based upon the analytical expression for the natural frequency:

$$f_n = \text{constant} \cdot \sqrt{\frac{\text{stiffness}}{\text{mass}}}.$$

From the analytical expression, observe that the stiffness parameters have positive exponents and the mass parameters have negative exponents. Based on this observation, the nonlinear regression results in the following expression for the predicted natural frequency  $f_{n,\text{pred}}$ :

$$f_{n,\text{pred}} = \frac{c_i \left(N_{\text{bay}} \frac{EI_c}{H^3}\right)^{0.22} (N_{\text{bay}} k_\theta)^{0.21} k_{x,z,\text{sup}}^{0.018}}{h^{0.5} (N_{\text{floor}} N_{\text{bay}} L_b \times p)^{0.5}}, \quad (5.3.2)$$

where  $c_i$  is a support coefficient. For **Equation 5.3.2**, the support coefficient  $c_i$  and key metrics are shown in **Table 12**. For the three support coefficients, the average error is between 4% and 5%, and both the Pearson  $R^2$  and the normal  $R^2$  are higher than 0.97. The largest errors occur for the most flexible frames with nine and ten floors and two bays.

Name			Pinned	Semi-rigid	Semi-rigid
Support stiffness	$k_{\theta,\text{sup}}$	Nm/rad	1	$5 \times 10^6$	$10 \times 10^6$
Support coefficient	$c_i$	–	1.00	1.09	1.13
Average error	$\bar{\varepsilon}$	%	4.5125	4.3639	4.1729
Pearson $R^2$	$R^2$	–	0.987	0.988	0.988
$R^2$	$R^2$	–	0.973	0.977	0.976

Table 12 Key metrics of the regression of the natural frequency  $f_{n,\text{pred}}$ .

In **Equation 5.3.2**, observe that the denominator is the squared total mass of the structure. This is in full agreement with **Equation 5.3.1**. From the exponents, the total height  $h$  of the structure and the total mass  $m$  are equally important for the natural frequency  $f_n$ . If the expression is rearranged, the total height  $h$  is the most important parameter. Observe that the column stiffness and the connection stiffness are almost equal in their importance.

**Figure 31** shows the correlation plots and histograms for the predicted natural frequency  $f_{n,\text{pred}}$  in **Equation 5.3.2** against the analytical expressions obtained through the eigenvalue problem. For all three support stiffnesses  $k_{\theta,\text{sup}}$ , the histogram of the predicted natural frequency  $f_{n,\text{pred}}$  matches the analytical natural frequency  $f_n$  almost exactly. For the correlation plots, observe that higher support connection stiffnesses  $k_{\theta,\text{sup}}$  yield a more slender and narrow distribution of the data. For higher support connection stiffnesses  $k_{\theta,\text{sup}}$ , higher natural frequencies can be achieved. This result agrees with the results in the following section about the frequency reduction factor. The outliers above the least squares dashed purple line, are the most slender, flexible, and light frames.

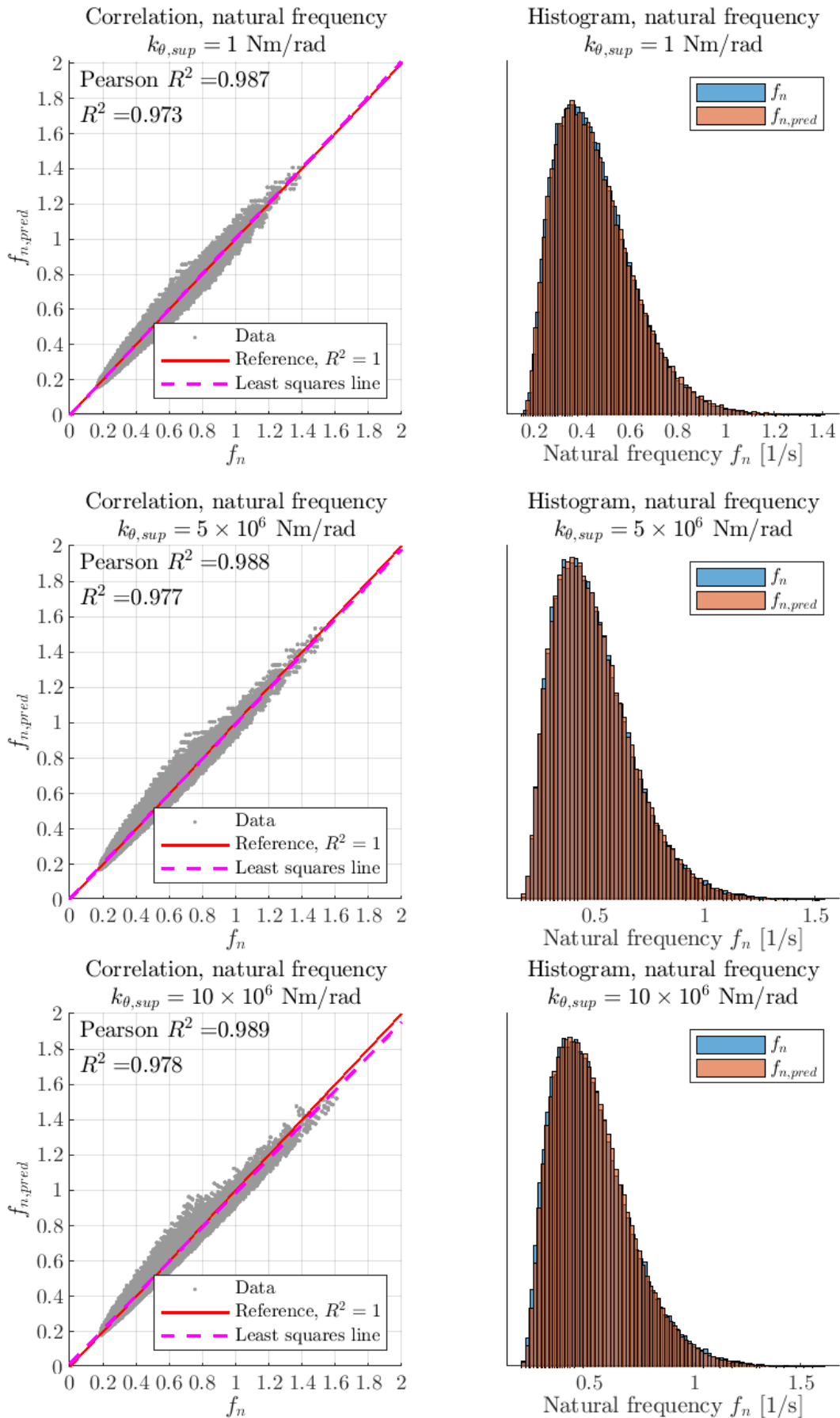


Figure 31 Correlation plots and histograms for the regression of the predicted natural frequency  $f_{n,pred}$  for different supports.

The total height  $h$  is the most important parameter as it is directly linked to the flexibility of the structure. The number of bays indirectly indicates the number of columns, beams, and connections per frame, making it another important stiffness parameter. The column stiffness is naturally more important than the beam stiffness for the building, which can be attributed to the beam stiffness being higher than the connection stiffness. Thus, the connection absorbs most of the deformations associated with the beam. With the connection stiffness being the weakest link with respect to rotations, it is natural that it also holds higher importance for the natural frequency than the beam stiffness. Both the lateral support stiffness and the rotational support stiffness are the least important parameters. This can be attributed to the limited rigid body behavior of the columns, with a limited ability to transfer shear forces. It is expected that structures with shear walls or structural panels that can transfer shear forces are more sensitive to the support stiffnesses.

### 5.3.2 Frequency reduction factor

From the computations of the natural frequencies, a unique  $f_n$ - $k_\theta$  sigmoid behavior with respect to connection stiffnesses for each of the frames is hypothesized and subsequently observed. To make the sigmoid behavior of each of the frames comparable, the natural frequencies  $f_n$  are normalized with respect to the natural frequency of a frame with rigid connections  $f_{n,\infty}$  and pinned supports. The normalized natural frequency inherits values  $f_n/f_{n,\infty}$  varies from zero to unity. An attempt to unify the sigmoid behavior for the semi-rigid frames is performed, resulting in an adjusted connection stiffness  $k_{\theta,adj}$ . A total of 24 300 different frames are analyzed in the investigation of the sigmoid behavior.  $k_\theta$

The adjusted connection stiffness  $k_{\theta,adj}$  is a function of the number of bays, number of floors, beam and column lengths, beam and column stiffness, and the connection stiffness. The adjusted connection stiffness can be expressed as:

$$k_{\theta,adj} = \left( \frac{n_{bay}}{n_{floor}^2} \cdot \frac{L_c^4}{EI_c^6} \cdot \frac{L_b^3}{EI_b} \right)^{\frac{1}{10}} \cdot k_\theta. \quad (5.3.3)$$

Based on the unified sigmoid of the normalized natural frequency, several types of mathematical sigmoids are used such as logistic, hyperbolic, and several algebraic sigmoids. Of these sigmoids, the following algebraic sigmoid is superior with a Pearson  $R^2$  of 1.00 for the pinned case:

$$\frac{f_n}{f_{n,\infty}} = \eta = \frac{1}{\left( 1 + \frac{200}{(k_{\theta,adj} + k_s)^{0.95}} \right)^{0.5}}, \quad (5.3.4)$$

where  $k_s$  is a support rigidity index. The support rigidity index  $k_s$  adjusts the lower tail of the sigmoid, or the frequency reduction factor  $\eta$ , according to the type of support conditions. The support rigidity index  $k_s$  has a range from zero for pinned supports, to five for rigid supports. An overview of the values of the rigidity index can be viewed in **Table 13**.

Support condition	Rigidity index $k_s$
Pinned ( $k_{\theta,sup} = 0$ )	0
Semi-rigid ( $k_{\theta,sup} = 5000$ kNm)	2
Rigid ( $k_{\theta,sup} = \infty$ )	5

Table 13 Overview of the rigidity index  $k_s$  according to the support conditions.

If the normalized natural frequency  $f_n/f_{n,\infty}$  in **Equation 5.3.4** is reformulated, the following expression can be obtained:

$$f_n = \frac{1}{\sqrt{1 + \frac{200}{(k_{\theta,adj} + k_s)^{0.95}}}} f_{n,\infty}, \quad f_{n,\infty} = \frac{1}{2\pi} \sqrt{\frac{k}{m}}. \quad (5.3.5)$$

The implication of the simple yet accurate expression for the natural frequency in **Equation 5.3.5**, is a simple equation to determine the natural frequency of a semi-rigid frame  $f_n$  from the natural frequency of a rigid frame  $f_{n,\infty}$ . A rigid frame is fast and easy to model in any finite element program, much more so than a semi-rigid frame.

The sigmoid, or the frequency reduction factor  $\eta$ , is plotted together with the computed normalized natural frequencies  $f_n/f_{n,\theta}$  in **Figure 32**. From **Figure 32**, observe that the normalized natural frequency  $f_n/f_{n,\infty}$  converges to zero when the adjusted connection stiffness is very low  $k_{\theta,adj}$  for pinned supports. When the adjusted connection stiffness  $k_{\theta,adj}$  is very high, the normalized natural frequency  $f_n/f_{n,\infty}$  converges towards unity. The frequency reduction factor  $\eta$  in **Equation 5.3.4** follows the sigmoid shape of the frames with great precision.

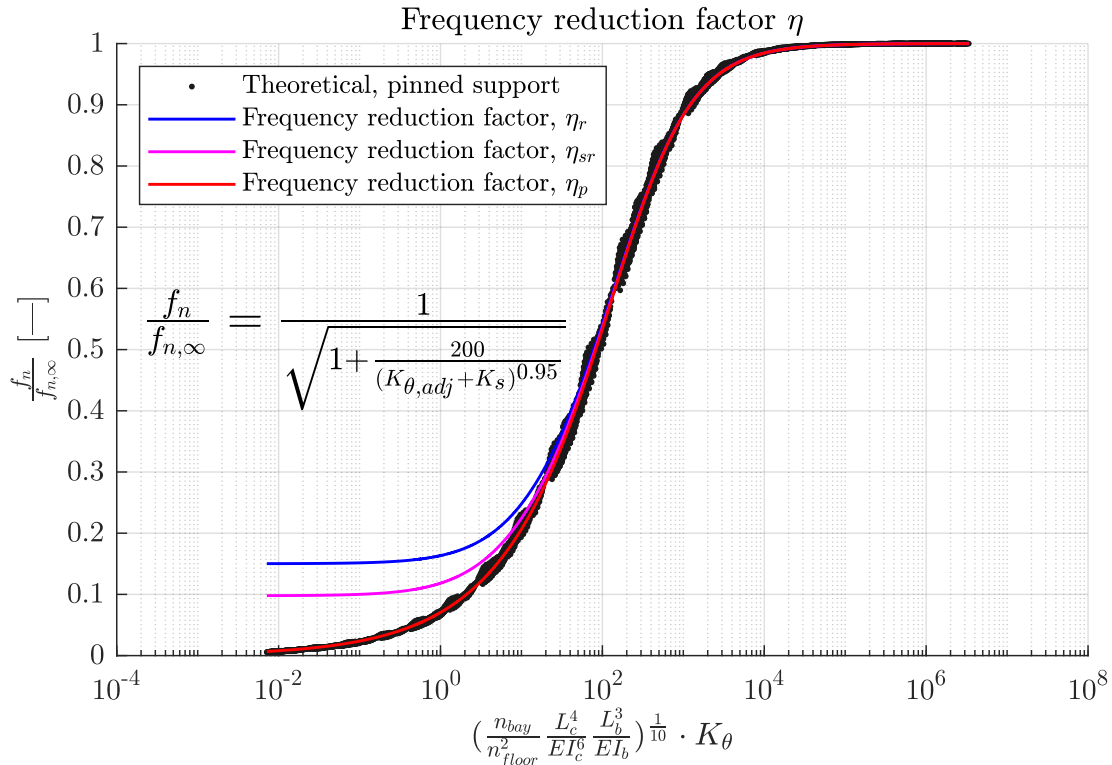


Figure 32 The frequency reduction factor  $\eta$  with respect to the adjusted beam-to-column rotational stiffness  $k_{\theta,adj}$  for pinned  $\eta_p$ , semi-rigid  $\eta_{sr}$ , and rigid  $\eta_r$  supports.

For the semi-rigid and rigid supports, observe that the normalized natural frequency  $f_n/f_{n,\infty}$  or the frequency reduction factor  $\eta_{sr}$  and  $\eta_r$  does not converge towards zero for pinned connections. For the rigid support, the frequency reduction factor  $\eta_r$  converges towards a value of about 0.2. For the

semi-rigid support, the frequency reduction factor  $\eta_{sr}$  converges towards a value of about 0.1. Both the semi-rigid  $\eta_{sr}$  and the rigid supports  $\eta_r$  converges to the same curvature as the pinned supports with an increasing adjusted connection stiffness  $k_{\theta,adj}$ .

The support conditions are not of high importance for the natural frequency of most engineering structures subjected to normal loads. The adjusted connection stiffness  $k_{\theta,adj}$  for most engineering structures is above  $10^2$ , yielding a frequency reduction factor  $\eta$  of about 0.5. The effects of the support conditions are mostly present for adjusted connection stiffnesses  $k_{\theta,adj}$  below the threshold of  $10^2$ . However, the effect of the support conditions may be important for robustness considerations.

From **Figure 32**, observe that the implications of semi-rigid or rigid support conditions is the presence of a residual natural frequency. If, for any reason, some, or most of the connections in the structure lose their connection stiffness in consistency with the behavior of plastic hinges, then any support stiffness will assist in preserving the natural frequency. In turn, any support stiffness will also preserve some of the stiffness in the structure in such an event. This can be observed through the relationship between the natural frequency, stiffness, and mass. Also, observe the nonlinear relationship between the support stiffness and the residual frequency. By using a relatively small support stiffness of  $5 \times 10^6$  Nm, the residual frequency is considerably closer to the rigid case than the pinned case.

The sigmoid relationship between the adjusted connection stiffness  $k_{\theta,adj}$  and the frequency reduction factor  $\eta$  is likely to exist in structures of other materials such as in concrete and steel. The investigation of the frequency reduction factor  $\eta$  for other types of structures is outside the scope of this thesis and should be an area of future research.

### Worked example 1

Consider the following example consisting of a two-story frame with two bays, beam dimensions  $0.28 \times 0.825$  m, column dimensions  $0.28 \times 0.30$  m, bay length 8 m, column height 4 m, surface load  $3000 \text{ kN/m}^2$ , frame spacing 2.4 m, connection stiffness of 10 000 kNm, and pinned supports. Then, the adjusted stiffness  $k_{\theta,adj}$  is:

$$k_{\theta,adj} = \left( \frac{n_{bay}}{n_{floor}^2} \cdot \frac{L_c^4}{EI_c^6} \cdot \frac{L_b^3}{EI_b} \right)^{\frac{1}{10}} \cdot k_{\theta} = 324 \text{ Nm.}$$

The frequency reduction factor  $\eta$  becomes:

$$\frac{f_n}{f_{n,\infty}} = \eta = \frac{1}{\left( 1 + \frac{200}{k_{\theta,adj}^{0.95}} \right)^{0.5}} = 0.74.$$

The following equation derived from analytical structural dynamics may be used to find the natural frequency of the rigid frame, and thus also the natural frequency of the semi-rigid frame:

$$f_{n,\infty} = \frac{1}{2\pi} \sqrt{\frac{k}{m}} = 1.02 \text{ Hz} \therefore f_n = f_{n,\infty} \eta = 0.76 \text{ Hz}$$

The theoretical solution for the natural frequency is 0.80 Hz, yielding an error of about 5%.

### Worked example 2

If the same calculations are done for an eleven-story frame with two bays, beam dimensions  $0.28 \times 0.825$  m, column dimensions  $0.28 \times 0.80$  m, bay length 8 m, column height 3.5 m, surface load  $3000 \text{ kN/m}^2$ , frame spacing 2.4 m, and a connection stiffness of 25 000 kNm, then the following numbers are obtained:

$$k_{\theta,\text{adj}} = 93 \text{ Nm} \therefore \eta = 0.52 \therefore f_{n,\infty} = 0.8642 \text{ Hz} \therefore f_n = 0.45 \text{ Hz}.$$

The theoretical solution for the natural frequency is 0.47 Hz, yielding an error of about 4%.

### 5.3.3 Accelerations

Based on the results in **Table 10**, the acceleration should be a function of the geometry, load, stiffness, and damping ratio. In this thesis, a damping ratio of 2% is chosen for the simulations. A damping ratio around 2% is common in measurements of existing timber structures (Feldmann, Harris, Dietsch, Gräfe, & Hein, 2016). Other parameters that are important for the accelerations are the mean wind velocity, wind spectrum, and the natural frequency of the structure. The geometry is important in terms of the wind velocity, the windward surface area, and the mass. For the wind velocity, the mean wind velocity is a function of the total height of the structure. For the windward surface area, the windward width can be used. For the mass, the same expression in the denominator can be used as in **Equation 5.3.2**. The stiffness of the structure is indirectly included in the natural frequency. The wind spectrum and damping ratio are included directly. The resulting expressions for the peak response accelerations for the gust factor approach and the generalized wind load are:

$$\ddot{x}_{GF,\text{pred}} = \frac{\rho_a c_f b \bar{u}}{N_{\text{floor}} N_{\text{bay}} L_b \times p} \frac{1}{2\pi\xi} \bar{u}^{1.4} S_L^{1.2} f_n^{-0.44}, \quad (5.3.6a)$$

$$\ddot{x}_{GWL,\text{pred}} = \frac{\rho_a c_f b \bar{u}}{N_{\text{floor}} N_{\text{bay}} L_b \times p} \frac{1}{2\pi\xi} \bar{u}^{1.1} S_L^{0.75} f_n^{-0.34}. \quad (5.3.6b)$$

where  $S_L$  is the normalized Kaimal spectrum in the Eurocodes:

$$S_L = \frac{f S_u(z, f)}{\sigma_u^2} = \frac{6.8 \cdot f_L(z, f)}{(1 + 10.2 f_L(z, f))^{\frac{5}{3}}}, \quad f_L = \frac{f L_u(z)}{\bar{u}(z)}. \quad (5.3.7)$$

In **Equation 5.3.7**,  $L_u$  is the turbulent length scale and  $f_L$  is the normalized frequency. For the generalized wind load in **Equation 5.3.6b**, the predicted peak acceleration is assumed as the 95% percentile for a gaussian distribution.

In **Equation 5.3.6**, the mean wind velocity  $\bar{u}$  is by far the most important parameter. Observe that the exponents of the normalized wind spectrum and the natural frequency are quite similar in both expressions in **Equation 5.3.6**. It is assumed that the damping ratio plays an important role for the accelerations. However, the damping ratio is not parametrized in this thesis.

**Table 14** shows key metrics of the regressions for the peak response accelerations in **Equation 5.3.6**. The Pearson  $R^2$  are both higher than 0.94, and the  $R^2$  higher than 0.89. The average error for the gust factor approach is about 10.7%, and the average error for the generalized wind load is about 16.3%. The higher average error in the generalized wind load can be attributed to stochastic

variations in the simulations, in contradiction to the gust factor approach which is a deterministic approximation.

	<b>Pearson R<sup>2</sup></b>	<b>R<sup>2</sup></b>	<b>Average error</b>
<b>Gust factor approach</b>	0.972	0.945	10.742
<b>Generalized wind load</b>	0.948	0.898	16.262

*Table 14 Key metrics of the regression of the peak acceleration for the gust factor approach and the generalized wind load.*

**Figure 33** shows the correlation plots and histograms for the predicted peak response accelerations  $\ddot{x}_{\text{pred}}$  in **Equation 5.3.6** against the analytical expression for the gust factor approach, and the stochastic simulations for the generalized wind load. In both cases, the histogram of the predicted peak acceleration  $\ddot{x}_{\text{peak}}$  matches the analytical expression and the stochastic simulations almost exactly. For the correlation plots, observe that the gust factor approach has a slenderer spread and a more gradual tail for the higher accelerations than the generalized wind load. From the histograms and correlation plots, observe that the accelerations in the gust factor approach are lower than in the generalized wind load. Like the expression of the predicted natural frequency in **Equation 5.3.2**, the outliers are the lightest and most flexible frames. Increased accuracy can be achieved by neglecting the data for the most flexible and light structures. The most important parameter for the flexibility of the structure is found to be the number of bays  $N_{\text{bay}}$ .



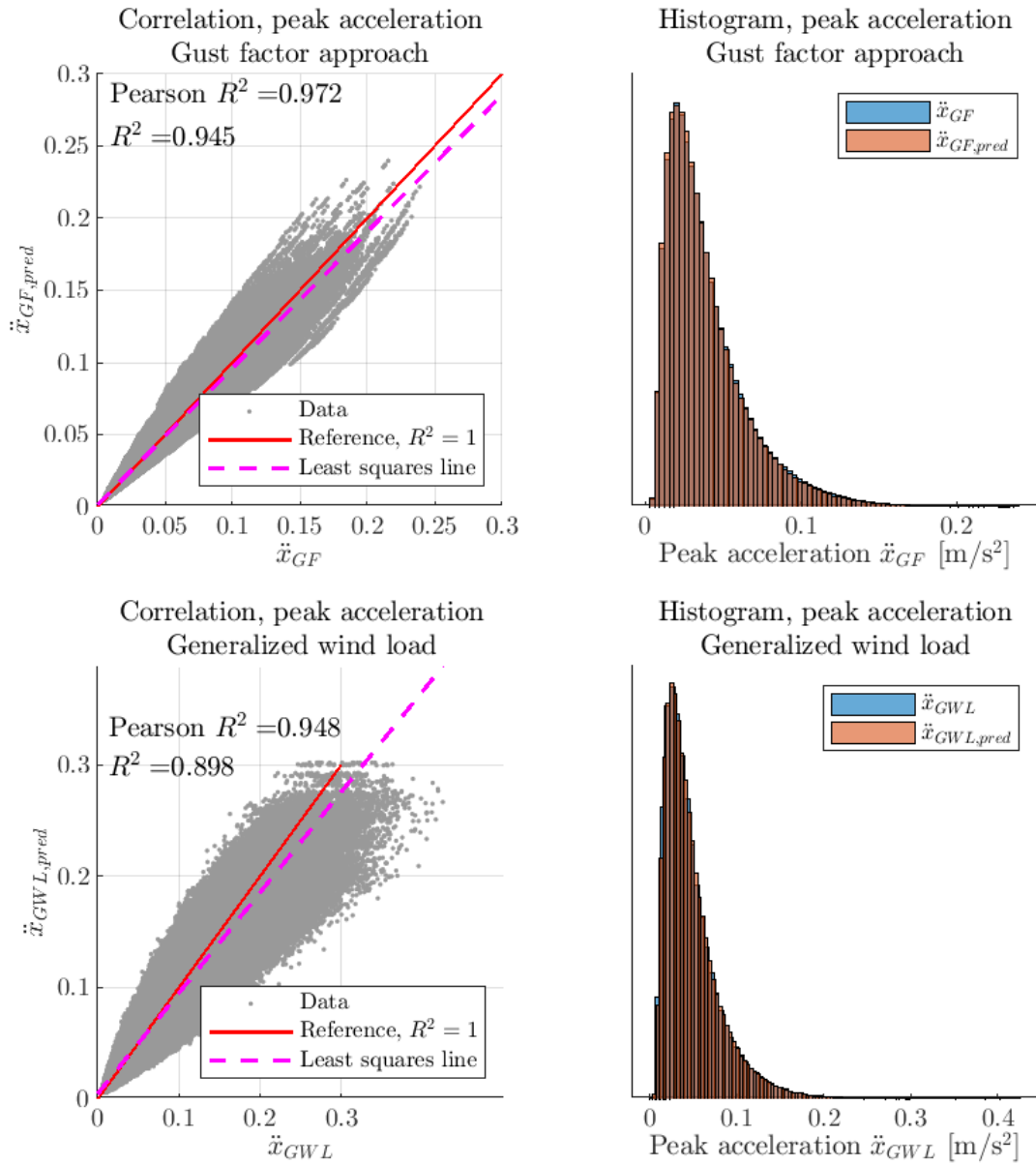


Figure 33 correlation plots and histograms for the regression of the predicted peak response accelerations  $\ddot{x}_{pred}$  for the gust factor approach and the generalized wind load.

### 5.3.4 Displacements

Based on the results in **Table 10**, the displacement should be a function of the geometry and stiffness parameters. Other parameters that are important for the displacements are the mean wind velocity and turbulent length scale. The geometry is important in terms of the wind velocity, the windward surface area, and the stiffness. For the wind velocity, the mean wind velocity is a function of the total height of the structure. The entire windward surface area is used, with a reduction with respect to the turbulent length scale to account for the aerodynamic admittance. The resulting expressions for the peak displacements are:

$$x_{GF} = c_i \frac{\frac{1}{2} \rho_a \bar{u}^2 c_f (N_{\text{floor}} H \times b) \times \left( \frac{L_u}{\sqrt{N_{\text{floor}} H \times b}} \right)^{5.34}}{N_{\text{bay}}^{1.25} \left( \frac{EI_b}{L_b^3} \right)^{0.05} \left( \frac{EI_c}{H^3} \right)^{0.4} k_{\theta}^{0.7} k_{x,z,\text{sup}}^{0.06}}, \quad (5.3.8a)$$

$$x_{GWL} = c_i \frac{\frac{1}{2} \rho_a \bar{u}^2 c_f (N_{\text{floor}} H \times b) \times \left( \frac{L_u}{\sqrt{N_{\text{floor}} H \times b}} \right)^{5.9}}{N_{\text{bay}}^{0.8} \left( \frac{EI_b}{L_b^3} \right)^{0.1} \left( \frac{EI_c}{H^3} \right)^{0.43} k_{\theta}^{0.71} k_{x,z,\text{sup}}^{0.05}}, \quad (5.3.8b)$$

where  $c_i$  is a support coefficient. For the generalized wind load in **Equation 5.3.8b**, the predicted peak displacement is assumed as the 95% percentile for a gaussian distribution.

In **Equation 5.3.8**, the mean wind velocity and the geometry are important parameters. The beam stiffness and lateral support stiffness are of less importance. Observe that in both expressions, the connections stiffness has similar exponents and is of high importance.

**Table 15** shows key metrics of the regressions for the peak response displacements in **Equation 5.3.8** for different support conditions. The Pearson  $R^2$  are both higher than 0.93, and the  $R^2$  higher than 0.87. The average error for the gust factor approach varies between about 12.0% and 15.0%, and for the generalized wind load between about 17.7% and 18.8%. In general, correlation is higher and the average error lower for the gust factor approach than the generalized wind load. This may in part be attributed to the stochastic variations in the simulations of the generalized wind load.

Support stiffness		$k_{\theta,\text{sup}}$	Nm/rad	Pinned	Semi-rigid	Semi-rigid
				1	$5 \times 10^6$	$10 \times 10^6$
Support coefficient	Gust factor approach	$c_i$	-	1.00	0.843	0.791
	Generalized wind load				0.801	0.736
Average error	Gust factor approach	$\bar{\epsilon}$	%	11.969	14.264	14.959
	Generalized wind load			17.660	18.229	18.765
Pearson $R^2$	Gust factor approach	$R^2$	-	0.971	0.958	0.956
	Generalized wind load			0.937	0.928	0.928
$R^2$	Gust factor approach	$R^2$	-	0.941	0.917	0.914
	Generalized wind load			0.878	0.860	0.860

Table 15 Key metrics of the regression of the peak displacement for the gust factor approach and the generalized wind load.

**Figure 34** shows the correlation plots and histograms for the predicted peak response displacements  $\ddot{x}_{\text{pred}}$  in **Equation 5.3.8a** against the analytical expression for the gust factor approach for different support conditions. Observe that the histograms of the predicted peak displacement for the gust factor approach matches the analytical expression almost exactly. For the correlation plots, observe that the correlation is the highest for the pinned support. For the semi-rigid supports, the accelerations are reduced considerably. The outliers are the most flexible and light structures.

**Figure 35** shows the correlation plots and histograms for the predicted peak response displacements  $\ddot{x}_{\text{pred}}$  in **Equation 5.3.8b** against the simulated data for the generalized wind load for different support conditions. Observe that the histograms of the predicted peak displacement for the generalized wind load are not as good as for the gust factor approach. For the correlation plots, the spread is also larger compared to the gust factor approach in **Figure 34**. For the semi-rigid supports, the accelerations are reduced considerably, with the outliers being the most flexible and light structures. This agrees with the observations in **Figure 34**.

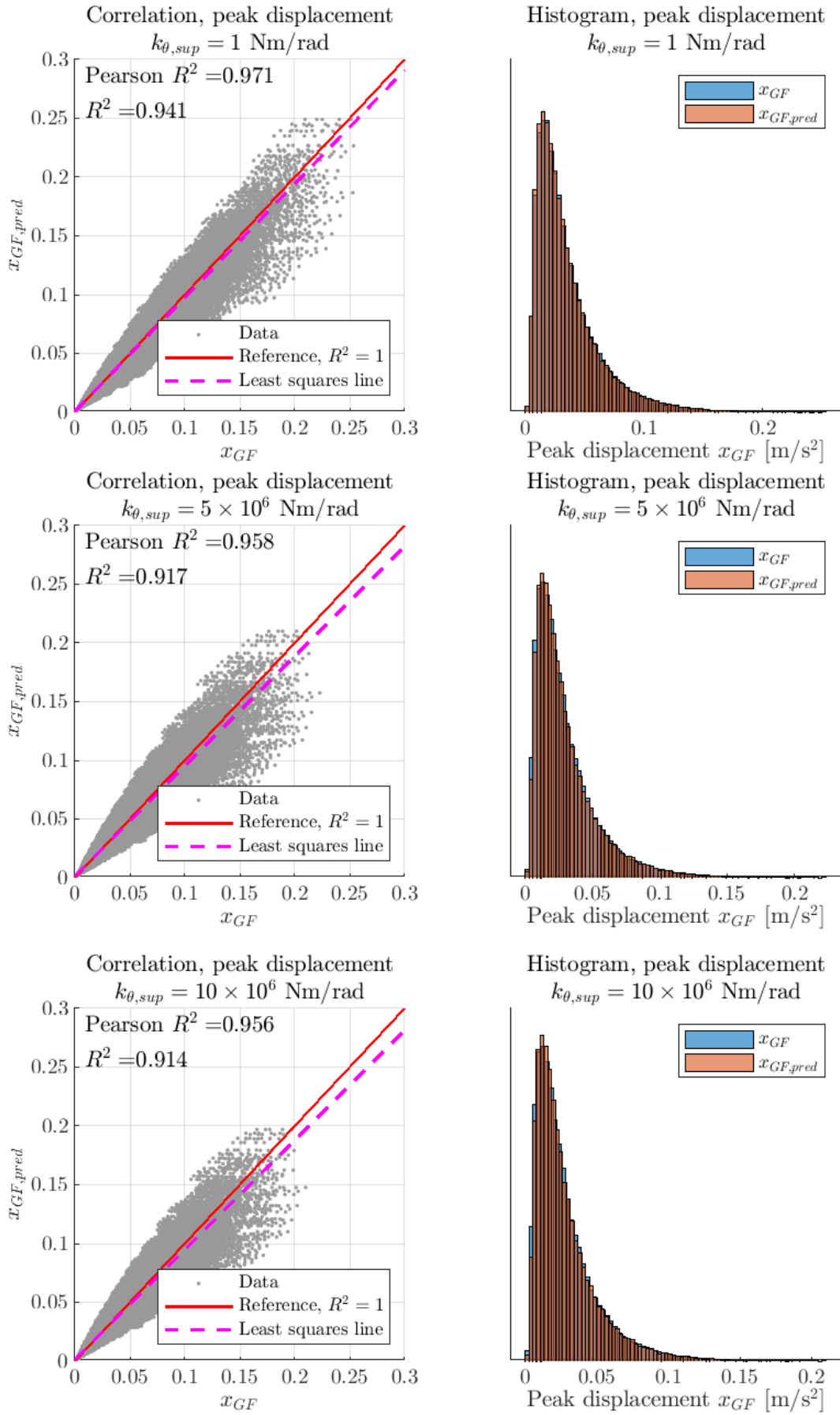


Figure 34 Correlation plots and histograms for the regression of the predicted displacement for the gust factor approach for different supports.

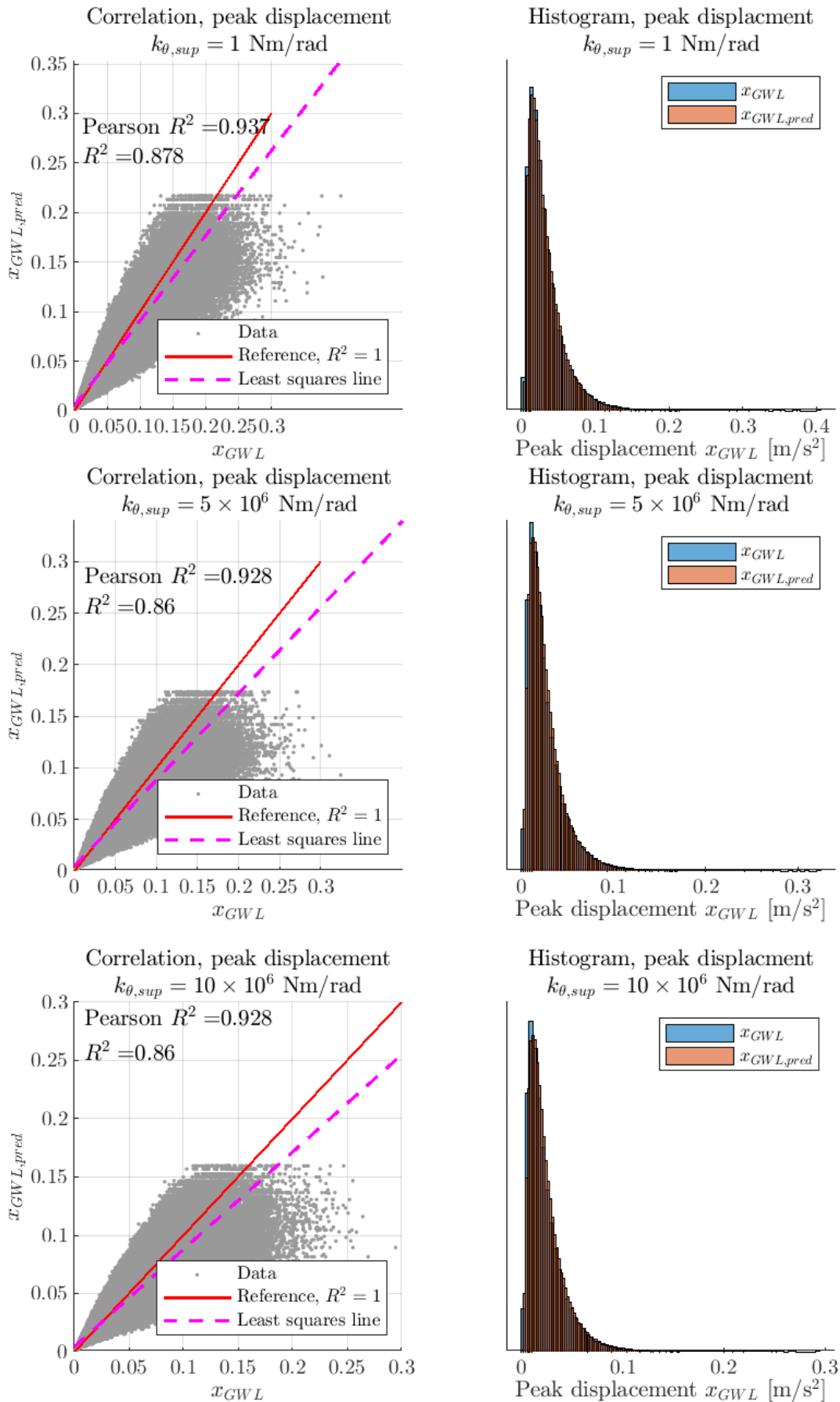


Figure 35 Correlation plots and histograms for the regression of the predicted displacements for the gust factor approach for different supports.

#### 5.4 Serviceability requirements in ISO 10137-2007

ISO 10137-2007 gives serviceability criteria for wind-induced vibrations in structures. It is based upon comfort criteria and gives the acceleration criteria with respect to the natural frequency of the structure in question. **Figure 36** shows the peak response accelerations for the gust factor approach and the generalized wind load for different wind velocities in the form of intensity maps. Darker colors indicate higher concentrations of simulated frames.

For a basic wind velocity  $v_{b,0}$  of 22 m/s, observe that all the frames in the generalized wind load satisfy the serviceability criteria for both office and residential structures. In the gust factor approach, almost all the frames satisfy the serviceability criteria. For the higher wind velocities  $v_{b,0}$ , the cloud of peak accelerations moves upwards with more frames not satisfying the serviceability criteria. For a basic wind velocity  $v_{b,0}$  of 30 m/s, between 18% and 19% of the frames do not satisfy the serviceability criteria. However, most of the frames do satisfy the strictest serviceability criteria of residential structures for all the wind velocities  $v_{b,0}$ .

Although the deviations in the computed response accelerations between the gust factor approach and the generalized wind load are large in **Figure 25** and **Figure 27**, the deviations in the percentages in **Figure 36** are surprisingly low. The intensity map of the gust factor accelerations in **Figure 36** is clearly less smoothly distributed than for the generalized wind load. However, the range of the observed data are in good agreement. The smoothness in the distributions for the generalized wind load is probably a result of the stochastic behavior of the generated time-series.

The intensity maps in **Figure 36** show that the wide range of semi-rigid timber frames simulated in this thesis are feasible. The frames that do not satisfy the serviceability criteria are the lightest and most flexible ones.

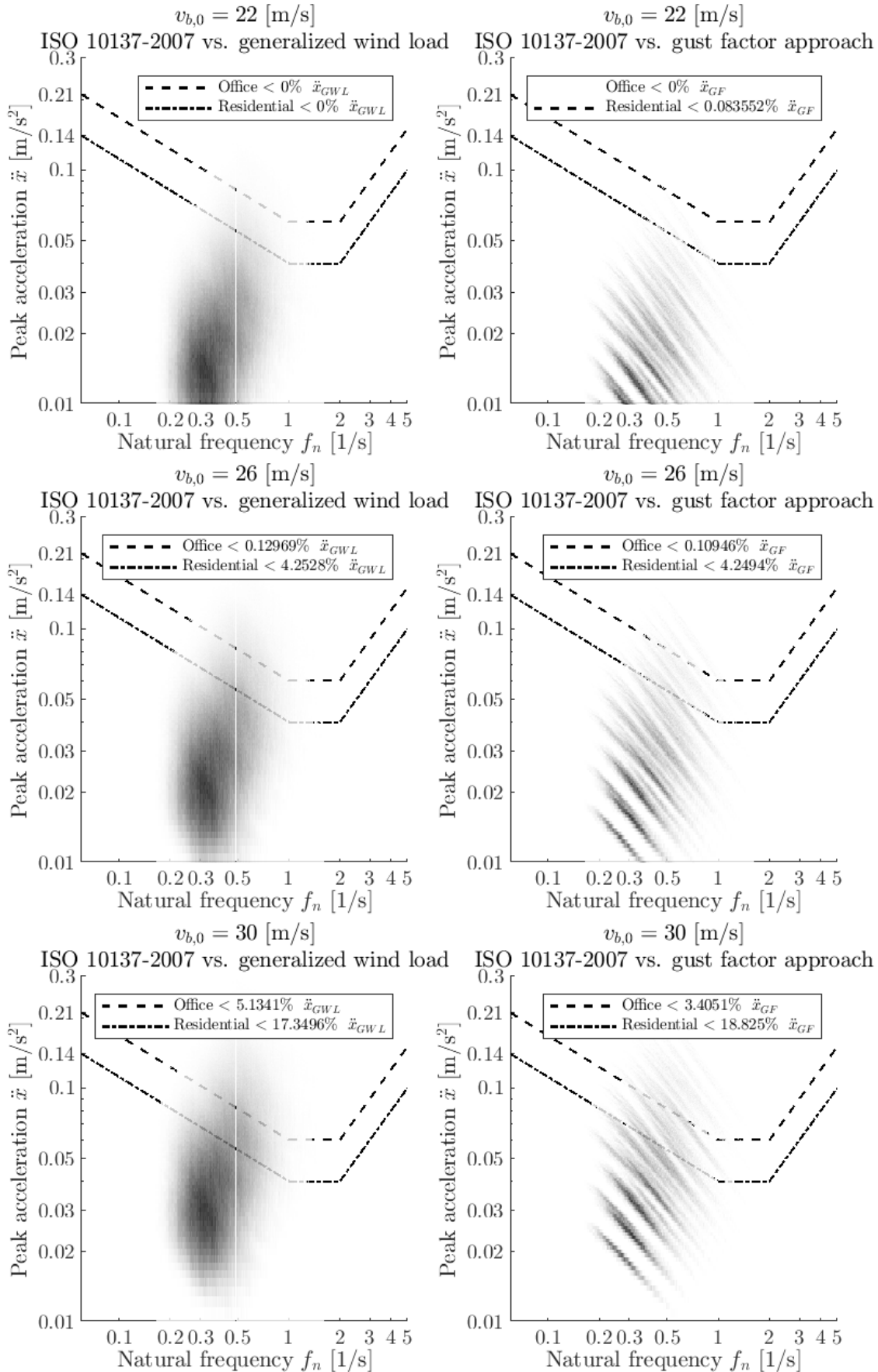


Figure 36 Peak acceleration criteria for wind induced vibrations from ISO 10137 and intensity maps of the peak accelerations for the gust factor approach and generalized wind load for different wind velocities.

## 5.5 Mass and height factor

Based on the parameters in **Table 6** and **Table 8**, the effect of the mass is investigated. First, the effect of an increasing uniform mass distribution in the structure is investigated. Second, the effect of adding more mass to one specific floor in the structure is investigated. For the nonuniform mass distribution, the simulations are limited to a structure with ten floors.

The results are presented in terms of a mass factor  $\eta_m$  and a normalized acceleration  $A_{N,m}$ , or a height factor  $\eta_h$  and a normalized acceleration  $A_{N,h}$ . The mass factor is the mass of the frames, normalized with respect to the lightest mass case:

$$\eta_m = \frac{p_s}{1600 \frac{\text{N}}{\text{m}^2}}. \quad (5.5.1)$$

The height factor is used for the nonuniform mass distribution. It is the location of the added mass in terms of height, normalized with respect to adding the mass at the very top of the structure:

$$\eta_h = \frac{h_m}{h_m = h}. \quad (5.5.2)$$

The normalized acceleration for the mass factor  $A_{N,m}$  is the acceleration of the structure, normalized with respect to a unit mass factor  $\eta_m$ , and a unit height factor  $\eta_h$ :

$$A_{N,m} = \frac{\ddot{x}(\eta_m, \eta_h)}{\ddot{x}(\eta_m = 1, \eta_h = 1)}. \quad (5.5.3)$$

The normalized acceleration for the height factor  $A_{N,h}$  is the acceleration of the structure, normalized with respect to a unit mass factor:

$$A_{N,h} = \frac{\ddot{x}(\eta_m, \eta_h)}{\ddot{x}(\eta_m = 1, \eta_h)}. \quad (5.5.4)$$

### 5.5.1 Uniform mass distribution

**Figure 37** shows the effect of increasing the mass of the structure uniformly for the gust factor approach used in the Eurocodes. Observe that increasing the mass decreases the accelerations. When the mass factor  $\eta_m$  is unity, the surface load is equivalent to a quasi-permanent load combination with a self-weight of 1 kN/m<sup>2</sup> and a live load of 2 kN/m<sup>2</sup>. This is regarded as the absolute lightest load combination for the semi-rigid timber frames using the Woodsol system. A structure with concrete floors will be equivalent to a mass factor  $\eta_m$  between 3.5 and 4.0 in **Figure 37**. If the gust factor approach is used, structures with concrete floors will have an acceleration that is more than 40% lower than the lightest timber frame. For the heaviest frame with a surface load of 7 kN/m<sup>2</sup>, the reduction in accelerations is more than 50%.



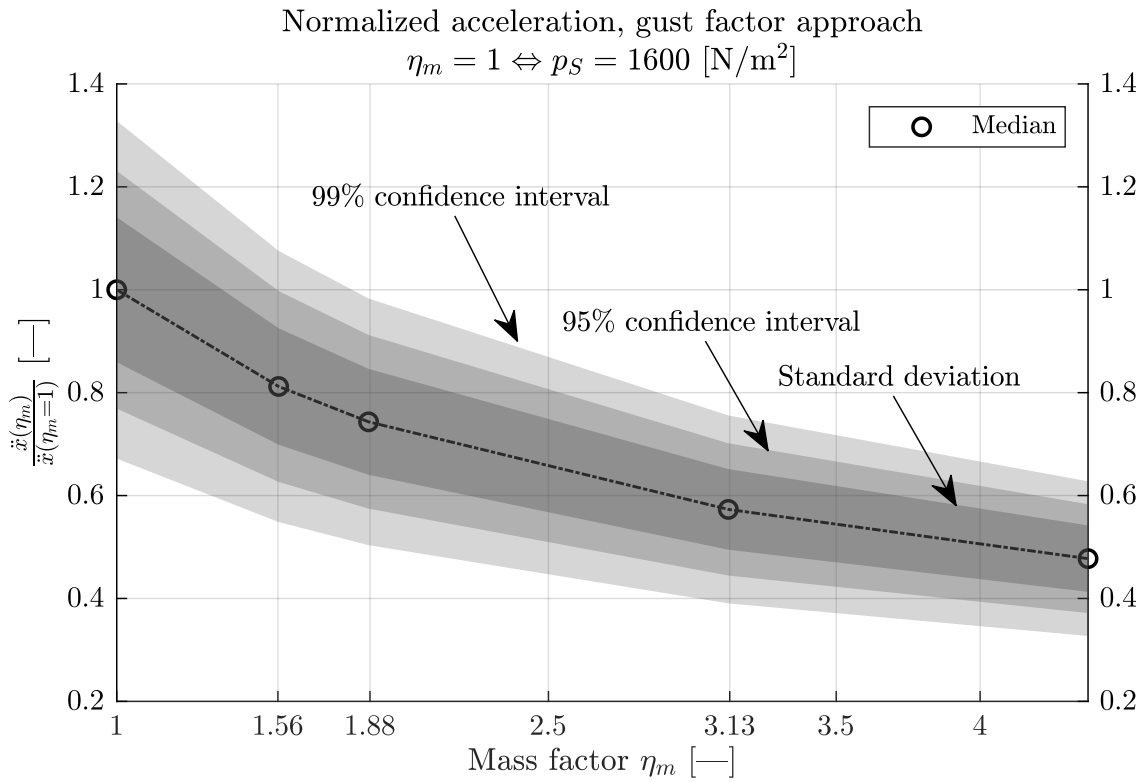


Figure 37 Normalized acceleration  $A_{N,m}$  with respect to the mass factor  $\eta_m$  for a uniform mass distribution. The figure shows the results for the gust factor approach.

**Figure 38** shows the effect of increasing the mass of the structure uniformly for the generalized wind load. Observe that the decreasing trend is similar to the trend in **Figure 37**. However, the trend in **Figure 38** has a more aggressive reduction with a steeper slope. For the heaviest frame with a surface load of  $7 \text{ kN/m}^2$ , the reduction in accelerations is more than 60% for the generalized wind load.

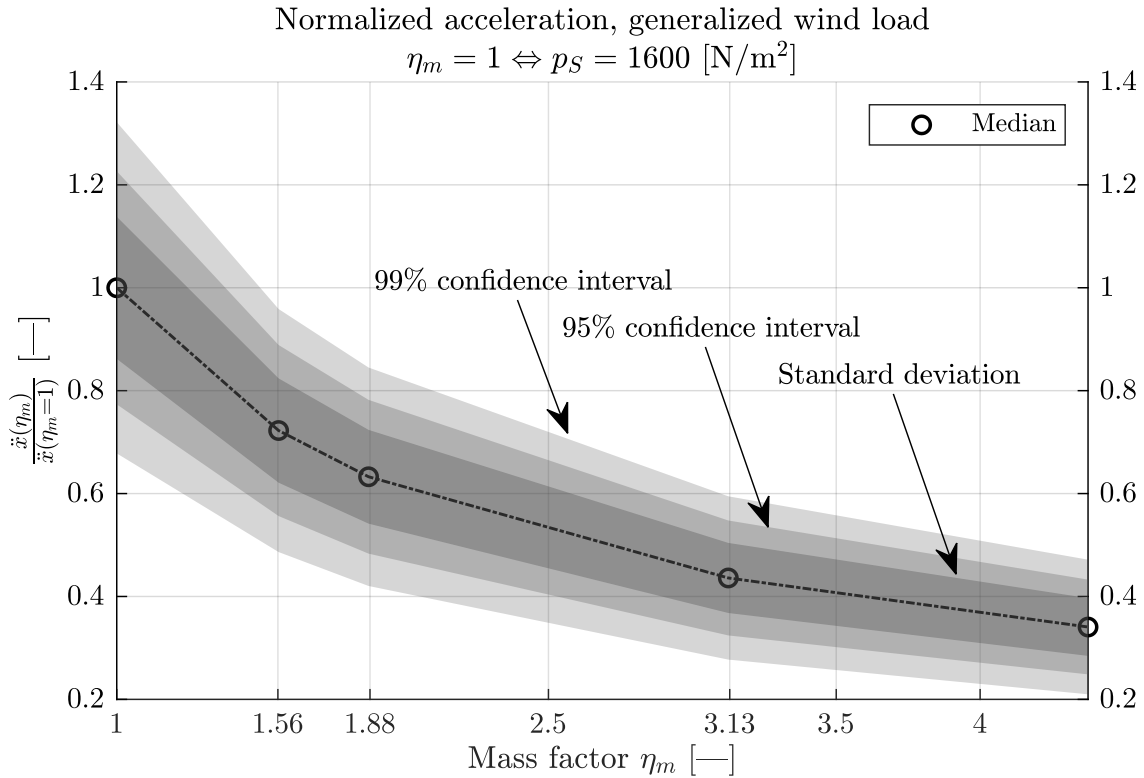


Figure 38 Normalized acceleration  $A_{N,m}$  with respect to the mass factor  $\eta_m$  for a uniform mass distribution. The figure shows the results for the generalized wind load.

## 5.5.2 Nonuniform mass distribution

### 5.5.2.1 Gust factor approach

**Figure 39** shows the effect of adding different amounts of mass  $\eta_m$  at different heights  $\eta_h$  for the gust factor approach, with the horizontal axis showing the mass factor  $\eta_m$ . The accelerations are normalized with respect to the base case where no additional mass is added. From the figure, observe that all added mass will contribute to reducing the accelerations independently of the location, except for a unit height factor  $\eta_h$ .

The optimal location of the mass is surprisingly not at the top node for the gust factor approach. From **Figure 39**, observe that the effect of adding the mass at the very top may increase the accelerations. This is the case if the amount of added mass is insufficient. If the mass factor  $\eta_m$  is 5 and the height factor  $\eta_h$  is unity, there is a slight decrease in the accelerations of about 1%. Observe that the optimal location of the mass is for a height factor  $\eta_h$  of 0.9. For a mass factor  $\eta_m$  of 5 and a height factor  $\eta_h$  of 0.9, the median reduction in acceleration is about 24%. For a mass factor  $\eta_m$  of 2 and a height factor  $\eta_h$  of 0.9, the median reduction in acceleration is about 3%.

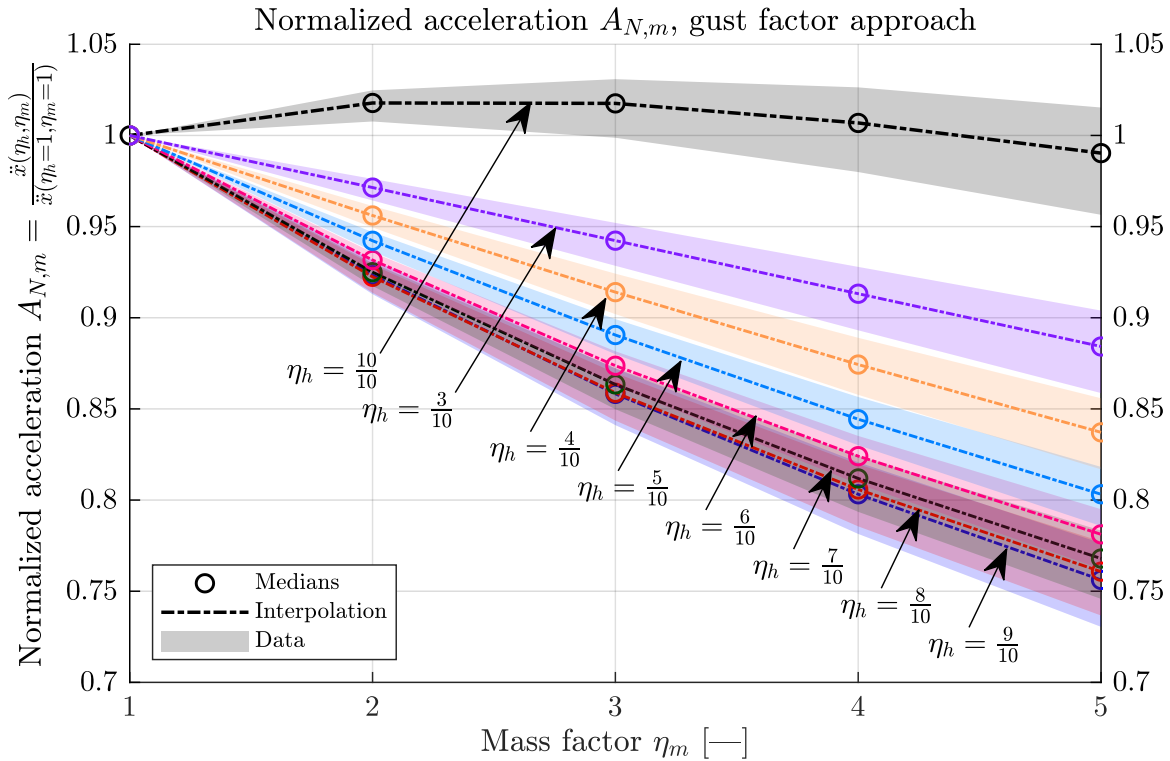


Figure 39 The effect of adding mass to the top floor of a ten-story structure for the gust factor approach. The circles denote the medians of the data, the shaded areas show the range of the data, and the dotted lines show the regressions.

**Figure 40** shows the effect of adding different amounts of masses  $\eta_m$  at different heights  $\eta_h$  for the gust factor approach, with the horizontal axis showing the height factor  $\eta_h$ . The accelerations are normalized with respect to the case where the individual added mass is added at the top of the structure with a unit height factor  $\eta_h$ . From the figure, observe that the optimal location for adding mass for the gust factor approach is for a height factor  $\eta_h$  of 0.9. Compared with placing the added mass at the very top of the structure, all other locations give a larger reduction in the accelerations.

If the mass is placed at the optimal location with a height factor  $\eta_h$  of 0.9, the reduction in accelerations for a mass factor  $\eta_m$  of 5 is up to 24%. If instead the mass factor  $\eta_m$  is 2, the reduction in accelerations is about 9%.

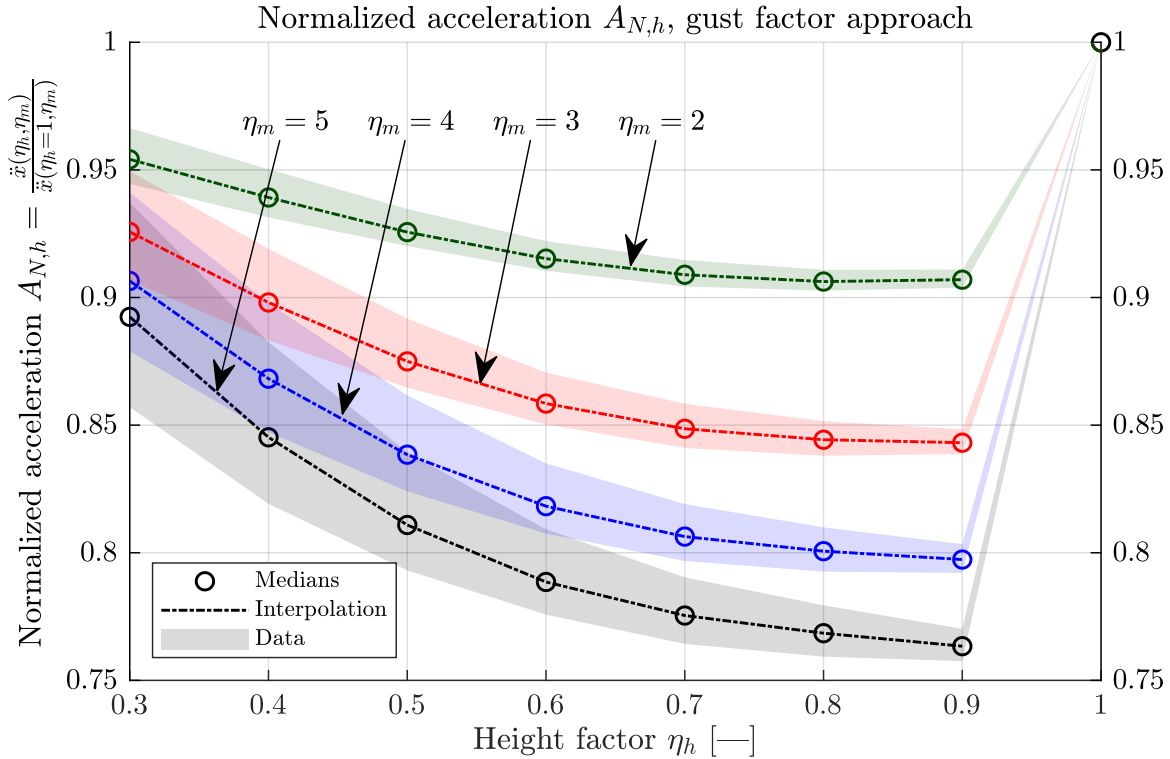


Figure 40 The effect of the location of the added mass on a ten-story structure for the gust factor approach. The circles denote the medians of the data, the shaded areas show the range of the data, and the dotted lines show the regressions.

From the results in **Figure 39** and **Figure 40**, the optimal location of the mass for the gust factor approach is at a height factor  $\eta_h$  of 0.9. At this optimal location, the added mass reduces the accelerations significantly more than for other locations. If the mass is placed at the top of the structure with a height factor  $\eta_h$  of 1.0, insufficient amounts of added mass may lead to larger accelerations. The implication of larger accelerations may be the exceedance of the serviceability criteria.

#### 5.5.2.2 Generalized wind load

**Figure 41** shows the effect of adding different amounts of mass  $\eta_m$  at different heights  $\eta_h$  for the generalized wind load, with the horizontal axis showing the mass factor  $\eta_m$ . Observe that the optimal location of the added mass is at the very top of structure with a unit height factor  $\eta_h$ . This result deviates from the similar figure for the gust factor approach in **Figure 39**. In the gust factor approach in **Figure 39**, placing the mass at the very top increases the accelerations, whereas in the generalized wind load in **Figure 41**, the same location decreases the accelerations. If the datapoint for a unit height factor  $\eta_h$  in the gust factor approach is neglected, the trends are the same in **Figure 39** and **Figure 41**.

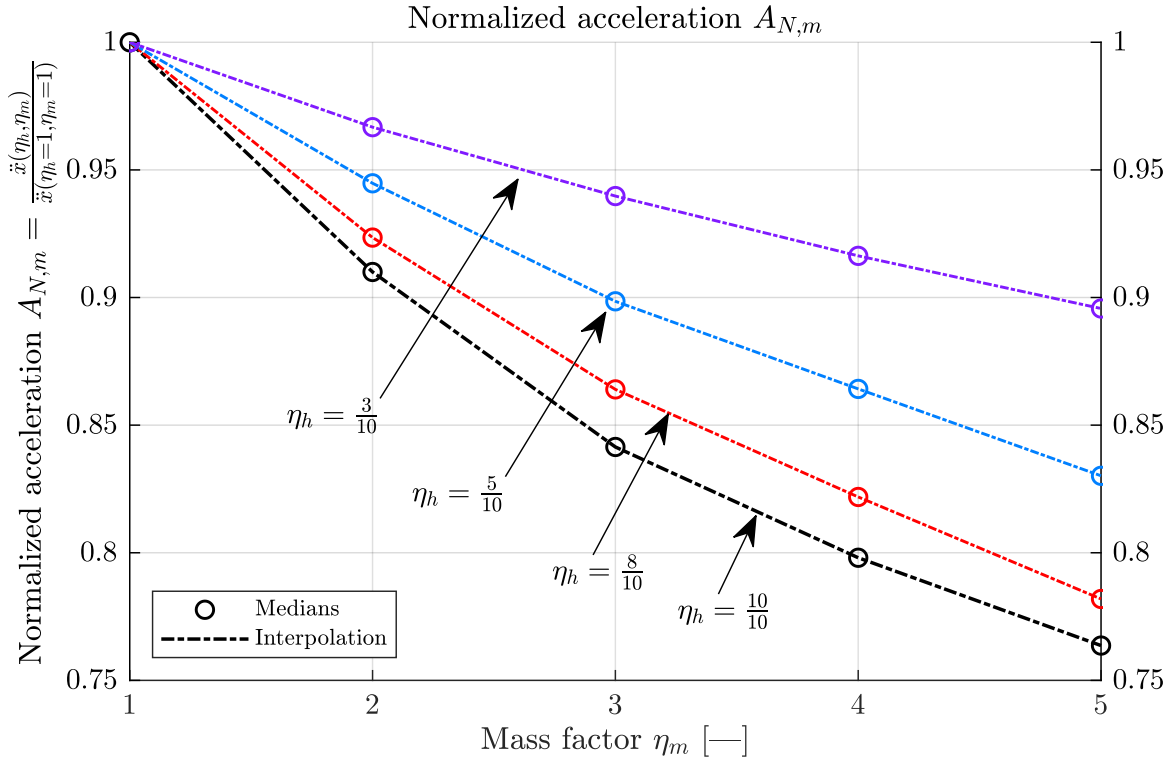


Figure 41 The effect of adding mass to the top floor of a ten-story structure for the generalized wind load. The circles denote the medians of the data, the shaded areas show the range of the data, and the dotted lines show the regressions.

The results in **Figure 41** for the generalized wind load, are in agreement with the uniform mass distributions for the gust factor approach in **Figure 37** and the generalized wind load in **Figure 38**. From **Figure 41**, observe that the reduction in accelerations for a unit height factor  $\eta_h$  for a mass factor  $\eta_m$  of four is about 20%. If instead a uniform mass distribution for a mass factor  $\eta_m$  of four is used, a 62% reduction in accelerations can be observed from **Figure 38**.

**Figure 42** shows the effect of adding different amounts of masses  $\eta_m$  at different heights  $\eta_h$  for the gust factor approach, with the horizontal axis showing the height factor  $\eta_h$ . Observe that the optimal location of the added mass is at the very top of the structure with a unit height factor  $\eta_h$ . This result deviates from the similar figure for the gust factor approach in **Figure 40**. In the gust factor approach in **Figure 40**, placing the mass at the very top gives larger accelerations than if the mass is placed anywhere else in the structure. Observe that the individual trends in **Figure 40** is similar to that of **Figure 42** for the height factors  $\eta_h$  up to and including 0.9.

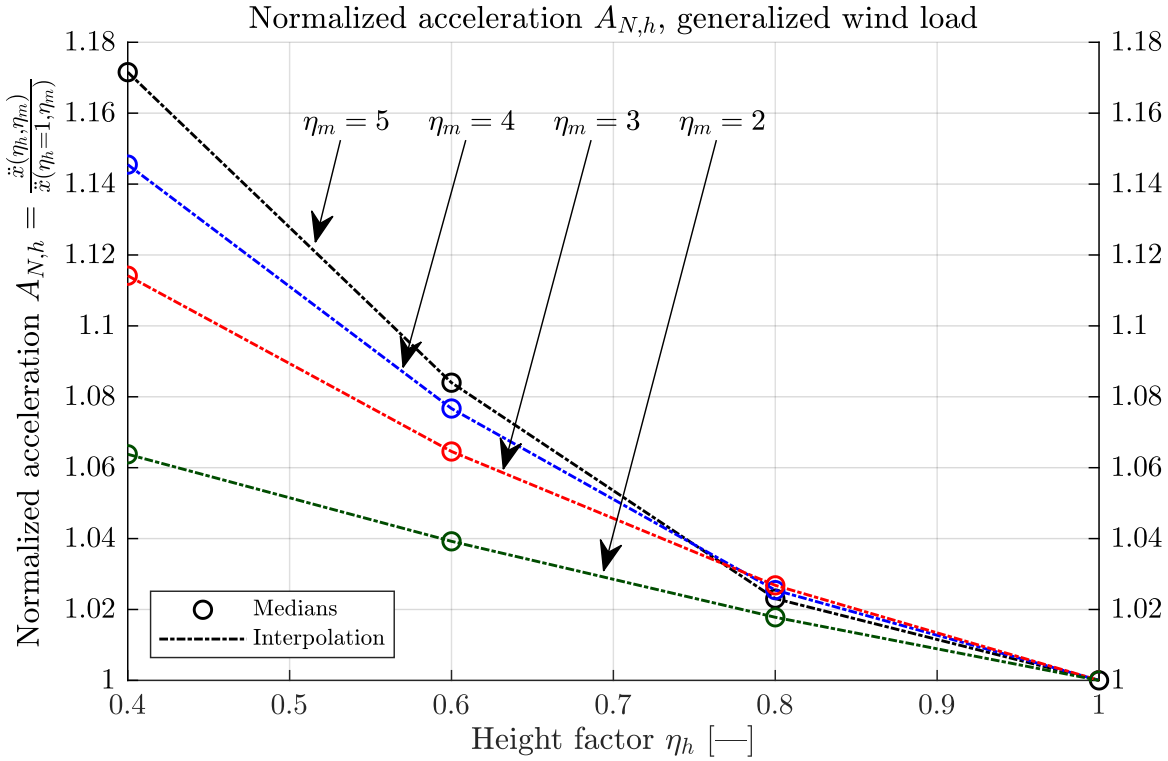


Figure 42 The effect of the location of the added mass on a ten-story structure for the generalized wind load. The circles denote the medians of the data, the shaded areas show the range of the data, and the dotted lines show the regressions.

The deviations with respect to the height factor  $\eta_h$  between the gust factor approach and the generalized wind load may be related to the method in the gust factor approach. The theoretical expression for the standard deviation of the response acceleration in the Eurocodes is provided at the end of this section.

From **Equation 5.5.9** in the derivation, observe that the force component is divided by the modal mass per unit height  $m_n$ . Thus, a higher modal mass per unit height  $m_n$  will result in smaller accelerations. To investigate this further, the modal mass per unit height for a structure with ten floors can be investigated. In this consideration, a mode shape according to the Eurocodes is used with a mode shape parameter  $\zeta$  of 0.6. The resulting normalized modal masses per unit height  $M_n$  are shown in **Table 16**.

$\eta_m$	1	10										
$\eta_h$	–	0	0.1	0.2	0.3	0.4	0.5	0.6	0.7	0.8	0.9	1.0
$M_n = \frac{m_n(\eta_h, \eta_m)}{m_n(\eta_m = 1)}$	1	1.004	1.119	1.287	1.464	1.659	1.861	2.071	2.289	2.513	2.743	1.989

Table 16 Normalized modal masses for a structure with ten floors for a mass factor  $\eta_m$  of 10 and a mode shape parameter  $\zeta$  of 0.6.

The data in **Table 16** are visualized in **Figure 43**. Observe that the normalized modal mass per unit length  $M_n$  has a sharp drop at a height factor  $\eta_h$  of 0.9. If the general trend for the data excluding the unit height factor  $\eta_h$  is extrapolated, the normalized modal mass per unit length  $M_n$  should increase by about 9%. However, the normalized modal mass per unit length  $M_n$  decreases by about 27% compared with a height factor  $\eta_h$  of 0.9.

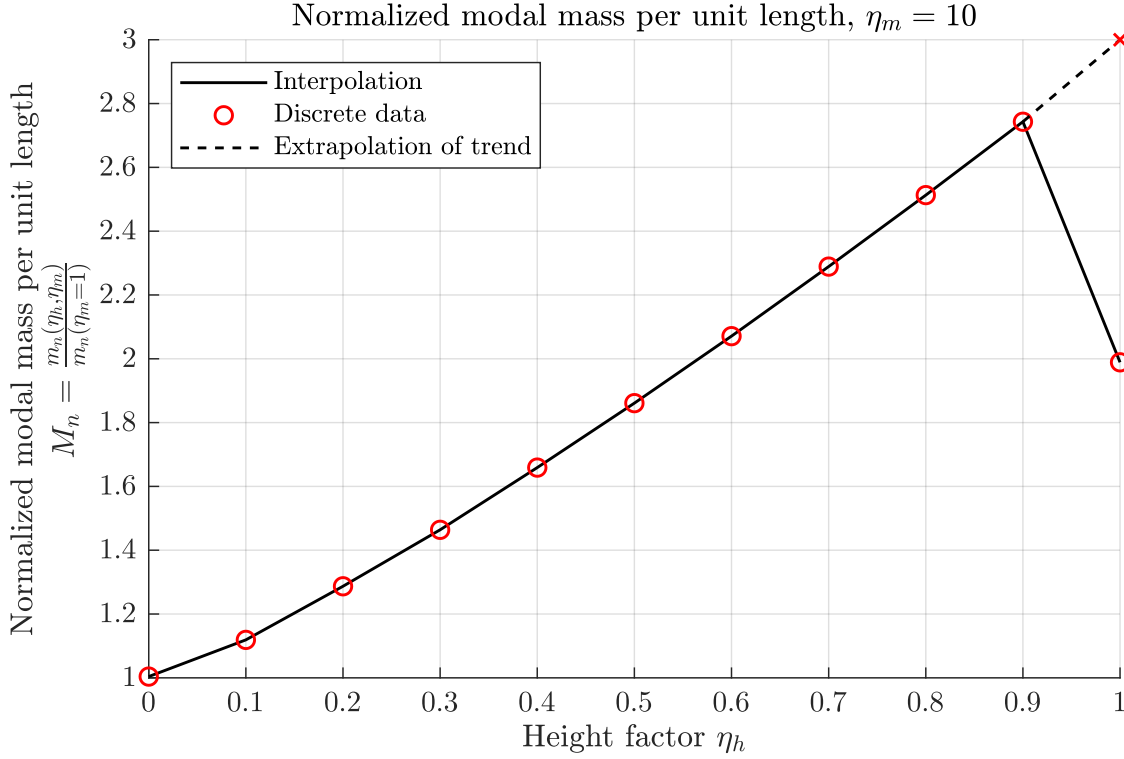


Figure 43 Visualization of the data in **Table 16** for the normalized modal mass per unit length  $M_n$  with respect to the height factor  $\eta_h$ , and an extrapolation of the trend.

#### Derivation of the standard deviation of the response acceleration:

The response acceleration can be derived from **Equation 3.34**, which is repeated here for convenience:

$$\frac{\sigma_x^2}{\bar{x}^2} = 4 \frac{\sigma_u^2}{\bar{u}^2} [A_B + A_R] = 4 \frac{\sigma_u^2}{\bar{u}^2} \left[ \int_0^\infty \frac{S_{uu}(\omega)}{\sigma_u^2} \chi^2(\omega) d\omega + \frac{\pi^2}{2\delta} \frac{\omega_n S_{uu}(\omega_n)}{\sigma_u^2} \chi^2(\omega_n) \right]. \quad (5.5.5)$$

To compute the response accelerations, the background factor  $A_B$  can be neglected. By substituting  $\bar{x} = \bar{F}/k$  for the mean static displacement, the following expression can be obtained:

$$\sigma_x^2 = 4 \frac{\bar{F}}{k} \frac{\sigma_u^2}{\bar{u}^2} \left[ \frac{\pi^2}{2\delta} S_L(\omega_n) \chi^2(\omega_n) \right]. \quad (5.5.6)$$

The mean static force is defined as **Equation 3.56a**. The mean static force is repeated here for convenience:

$$\bar{F}_n = \frac{1}{2} \rho C_{D,r} \bar{u}_r^2 A. \quad (5.5.7)$$

To find the standard deviation of the response acceleration, **Equation 5.5.6** can be multiplied by  $\omega_n^4$  before the square root is performed:

$$\sigma_{\ddot{x}} = \frac{\rho C_D A \bar{u} I_u}{m} \sqrt{\frac{\pi^2}{2\delta} S_L(\omega_n) \chi^2(\omega_n)}, \quad (5.5.8)$$

where  $I_u = \sigma_u/\bar{u}$  is the turbulence intensity. For modal analysis, **Equation 5.5.8** can be rewritten as:

$$\sigma_{\ddot{\eta}_n} = \frac{\rho C_D b \bar{u} I_u}{m_n} \sqrt{\frac{\pi^2}{2\delta} S_L(f_n) \chi_{\phi_n}^2(f_n)}, \quad (5.5.9)$$

where  $m_n$  is the modal mass per unit height and  $n$  is the vibration mode. The modal mass per unit height  $m_n$  can be expressed as:

$$m_n = \frac{\int_h \phi_n^2(z) m(z) dz}{\int_h \phi_n^2(z) dz}. \quad (5.5.10)$$

### 5.5.2.3 Mode shapes

To investigate the effect of the location of the mass  $\eta_h$ , the mode shapes  $\phi_i$  are evaluated qualitatively. **Figure 44** shows the nine first mode shapes  $\phi_i$  for a structure with a mass factor  $\eta_m$  of five, and a height factor  $\eta_h$  from 0.3 to 1.0. In the MATLAB routine, one single finite element is programmed for each of the beams. For a structure with ten floors, there are ten finite elements in the vertical direction. Thus, the solution of the eigenvalue problem to obtain the mode shapes will only yield discrete points in each of the floors. For better visualization of the higher modes, cubic spline interpolation is used to smooth the mode shapes and to obtain the intermediate points.

Observe that for the first mode shape  $\phi_1$ , a lower height factor  $\eta_h$  will result in a more shear-dominated displacement pattern. For the higher height factors  $\eta_h$  above 0.7, the displacement pattern is more flexural. For a height factor  $\eta_h$  of 0.7, the mode shape is very consistent with the case of uniform mass distribution for most of the modes. The lower part of the building in timber structure, will in many cases have a more shear-dominated displacement pattern. This is due to the limited connection stiffness, especially in the column-to-foundation connections.

From the second and third mode shapes  $\phi_2$  and  $\phi_3$ , observe that the maximum amplitudes are reduced if the mass is located strategically at the peaks of the mode shapes. However, the amplitudes can be reduced even more if the mass is located at slightly different locations. For instance, the second mode shape  $\phi_2$  can be reduced by a magnitude of about 40% for a height factor  $\eta_h$  of 0.6. For a height factor  $\eta_h$  of 0.3, the peak of the second mode shape  $\phi_2$  is not reduced as much as for a height factor  $\eta_h$  of 0.6. However, the magnitude of the second mode shape above a normalized height of 0.6 is less severe.



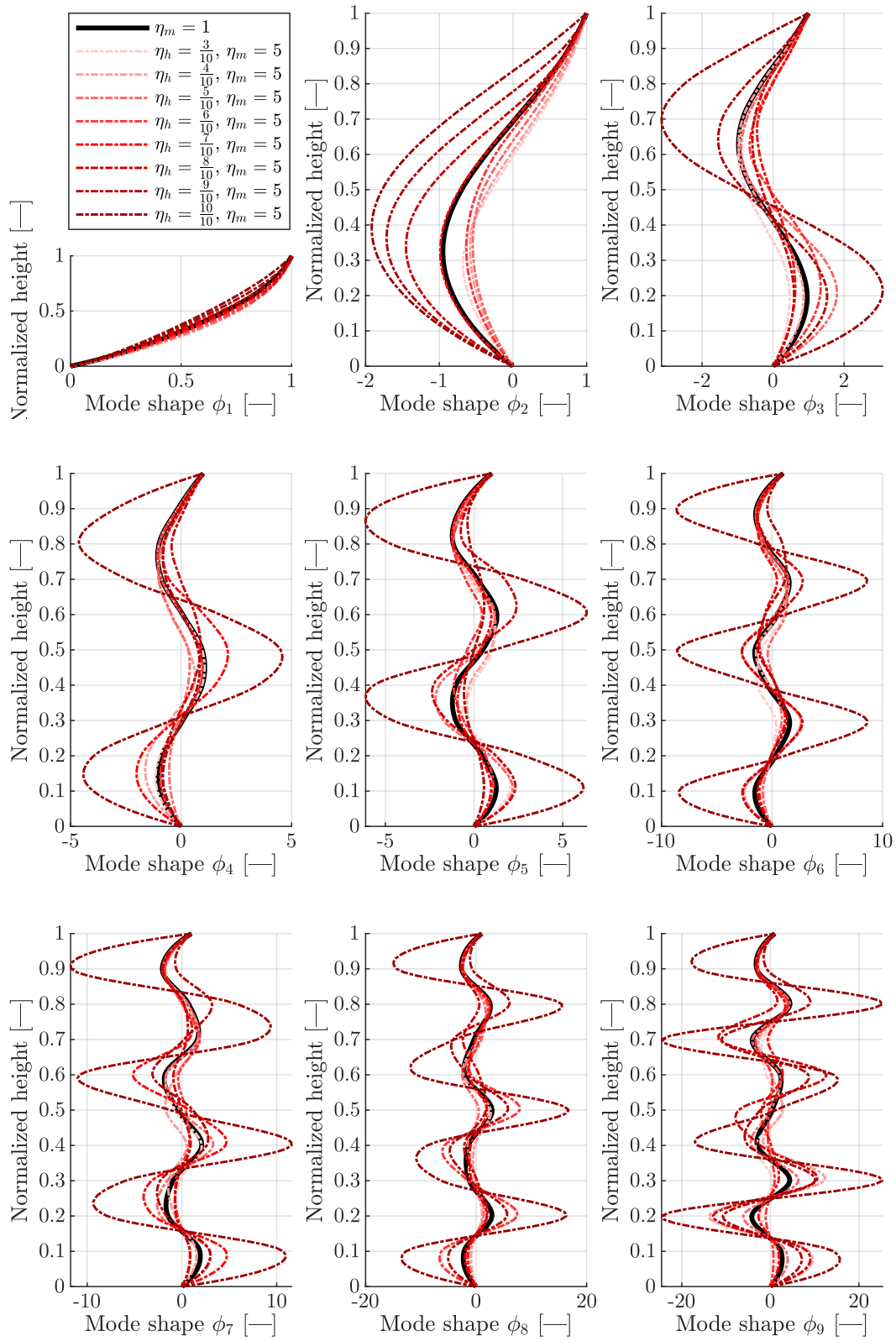


Figure 44 Mode shapes for various height factors  $\eta_h$  and a mass factor  $\eta_m$  of five.

Observe for the second and higher modes  $\phi_{i \geq 2}$  that the amplitude of the mode shapes are amplified for large height factors  $\eta_h$ . For the second mode shape  $\phi_2$ , height factors above 0.7 result in an amplitude that is almost twice as large as for the uniform mass distribution. For the third mode shape, a unit height factor  $\eta_h$  gives a maximum amplitude of more than three times that of a uniform mass distribution.

For the higher mode shapes, the maximum amplitude is consistently larger for a unit height factor  $\eta_h$ . However, the higher mode shapes are of less importance. For rigid-like structures such as most conventional concrete and steel buildings, the first mode shape  $\phi_1$  is often the governing mode shape. In the Eurocodes, only the first mode shape  $\phi_1$  is used for most buildings. For more flexible structures such as long-span bridges, the inclusion of more mode shapes is necessary to model the dynamic response appropriately. Timber buildings are more flexible and lightweight than rigid-like concrete and steel buildings, but more rigid than long-span bridges. Thus, the dynamic response of timber buildings may necessitate the inclusion of higher modes as their influence is magnified.

In the design for long-span floating pontoon bridges with seabed anchors, mooring lines can be used to damp the amplitudes of the mode shapes. In the Bjørnafjorden fjord crossing project on the western coast of Norway, several concept designs have been proposed for a floating bridge with anchors. The fjord is about 5 km wide. The location of the mooring lines is such that they intersect the maximum number of amplitudes for all the modes. In this manner, the maximum amplitudes may be damped. The amount of damping is dependent on the slope and stiffness of the mooring lines. The same strategy is used in super-tall structures, albeit with tuned mass dampers located at strategic heights of the structure to damp as many of the mode shapes as possible. This strategy can readily be applied to tall timber structures to reduce the dynamic response with active or passive masses.

In super-tall structures, active tuned mass dampers are widely used. For other tall structures, passive masses such as the concept in this thesis are used. For the 81 m tall timber building Mjøstårnet in Norway, the upper seven floors have 300 mm concrete slabs (Abrahamsen, 2017). For the other floors above the ground floor, prefabricated timber deck elements are used. The introduction of 300 mm concrete slabs in the upper seven floors enables the building to satisfy the ISO 10137 serviceability criteria with respect to wind-induced vibrations.

The strategic location of mass in timber structures may be a necessity for constructing taller timber structures than today. A uniform mass distribution is feasible, as is demonstrated in **Figure 37** and **Figure 38**. However, a light structure is desired to reduce the base shear in seismic design. In seismic design, heavier structures are synonymous with larger shear forces in the base of the structure. For timber structures, shear capacity is limited and is a brittle failure mode. Thus, increased base shear may pose a challenge with respect to the shear force in the column-to-foundation connections if a uniform mass distribution is used. Therefore, light weight structures are desired to reduce the overall seismic loads on the structure.

## 6 Limitations and future work

### 6.1 Limitations

In this thesis, several hundred thousand semi-rigid frames were simulated for several wind loads. In total, several million simulation were performed. This approach brings with it advantages, primarily with the large dataset. However, the choices and the scope of this thesis result in some limitations. The limitations are discussed in the following sections.

#### 6.1.1 Structural model

In this thesis, a finite element script is developed in MATLAB for planar skeleton frames. To account for the windward width, the planar frames are assumed to have a spacing of 2.4 m for a total windward width of 24 m. It is assumed that the connecting timber decks between the frames inherit full diaphragmatic behavior. Due to the planarity of the system, only lateral deformations and eigenmodes can be modelled. To reduce the size of the eigenvalue problem, only the lateral degrees of freedom are retained. In this simplification, all axial vibration modes and deformations are neglected. This simplification through static condensation has been widely applied in dynamics, where the horizontal degrees of freedom are the most important. It is assumed that the vertical inertia is small. For braced systems, this simplification leads to a greater loss of accuracy compared to the semi-rigid skeleton frame system in this thesis.

In the finite element formulation, the structural elements are mathematically perfect. In this sense, the connections have no spatial dimensions and the beams and columns are not offset from each other. For real structures, a small eccentricity or offset is always present in the connections. It is assumed that the eccentricity that the connections introduce is negligible.

For every floor, the columns are modelled with rigid boundary conditions. In this way, the columns are essentially continuous without any joints. In practice, all timber structures have numerous joints and connections due to limitations on element lengths due to transportation criteria. Due to this, the modelled structures are believed to be stiffer than what is realistic. This is especially due to the extreme difficulty in timber engineering to engineer sufficiently rigid joints and connections. Future improvements in the finite element routine should include rotational springs in the column-to-column joints to quantify the effect of semi-rigid column-to-column joints.

To model the stiffness of the prefabricated timber decks in the Woodsol system, an equivalent cross-section for a beam with constant width is used. The prefabricated timber deck is a composite laminated veneer lumber and glued laminated timber deck. The intersection between laminated timber beams and the laminated veneer lumber plates is either glued or connected by using self-tapping screws. It is assumed that there is full composite behavior in the prefabricated timber deck. From existing prototypes of the prefabricated timber deck, the Euler-Bernoulli stiffness has been measured through a series of bending tests. In the finite element model, an equivalent rectangular Euler-Bernoulli beam cross-section is used. Consequently, shear deformations in the prefabricated timber deck is neglected. In timber engineering, shear deformations are much more prominent than in steel or concrete structures and should be accounted for.

To simplify the choice of cross-sectional dimensions, the width of the column and equivalent beam cross-sections are kept constant at a width of 0.28 m. This choice makes the choice of beam and column stiffnesses intuitive, as the Euler-Bernoulli bending stiffness is then only a choice of the cross-sectional height. However, this simplification leads to inaccuracies in the columns since they

are modelled using Timoshenko beam elements. In Timoshenko beam theory, the bending and shear components of the stiffness matrix are functions of the cross-sectional area. Therefore, the stiffness in the columns may be slightly inaccurate due to some unrealistic choices of the column cross-sections for the frames with higher floors. However, the stiffness components get the highest stiffness contributions from normal Euler-Bernoulli beam theory. Thus, the effect of neglecting the different cross-sectional area due to unrealistic cross-sections is assumed to be insignificant.

In timber structures, cracks in the structural elements are of common occurrence. Cracks are present in most structural timber elements due to natural swelling and shrinking. In the Eurocodes, the cross-sectional area is reduced in all shear-related design checks to account for the cracks. In this thesis, the structural elements are modelled as mathematically perfect without any cracks or imperfections. The effect of the cracks if they are modelled, will only impact the cross-sectional area of the columns in the Timoshenko formulation. Since this thesis is focused on the serviceability of timber structures, it is assumed that the effect of the cracks on the overall stiffness of the structure can be neglected. For designs in the ultimate limit state, the reduction of the cross-sectional area due to cracks should be included.

Based on the connections of the Woodsol system, connection stiffnesses of up to 25 000 kNm/rad can be achieved by reasonable dimensions in the prefabricated timber deck and columns. However, the scope of this thesis does not include the analysis of the connections, their design, and cyclic behavior. Thus, the semi-rigid frames in this thesis are indifferent to the design of the connections if they can demonstrate sufficient rotational stiffnesses. At present, the connections in the Woodsol system are state of the art in timber engineering.

For the connections, all the degrees of freedom except for the rotational are rigid. Experimental validation of this assumption has been carried out for the Woodsol system, and the assumption has been shown to be of reasonably accuracy (Vilguts, Malo, & Stamatopoulos, 2018).

In the finite element routine, it is assumed that there is no central core which provide lateral stiffness to the structure. It is also assumed that walls and other structural and non-structural elements do not contribute to the overall stiffness of the structure. Elevator and staircase shafts are present in most engineering structures, which in most cases often provide necessary lateral stiffness. However, there are some structures which do not have elevator and staircase shafts in the structure. In such cases, they are often built as a separate secondary structure adjacent to the primary structure. These secondary structures may be connected to the primary structure by non-structural elements. Thus, some structures may behave as the skeleton frame system in this thesis.

In the mathematical model, all nonlinear effects are neglected. This includes nonlinear structural behavior, but also nonlinear effects from loads such as air-elastic effects. In the serviceability limit state, this is likely a good approximation. Nonlinear structural response is more important for the ultimate limit state with the utilization grade reaching 100%. It is assumed that the connection stiffness is linear in its behavior. Air-elastic effects become important for slender structures subjected to high wind velocities. However, vortex-shedding is a well-known phenomenon in square or rectangular structures of some height. If the frequency of the vortex frequency coincides with the natural frequency of the structure, excessive across-wind vibrations may occur. For light and flexible structures such as timber structures, nonlinearities may become more prominent at an early stage than for steel and concrete structures. Here, only the linear analysis is performed for the along-wind response.

In this thesis, Rayleigh damping with a damping ratio of 2% is chosen for all the simulations except for in the parameter study of the reference frame. In timber structures, damping is a black box and is a major area of research at present. However, measured values of the damping ratio in existing timber structures exist. The chosen damping ratio of 2% is in the same range as the measured values for existing dowel-type timber structures. The damping ratio for semi-rigid timber frames with rod-connections is not well quantified in literature. From the parameter study for the reference frame, the damping ratio has little impact on the response displacements. However, the damping ratio is important for the response accelerations. To accurately predict the response accelerations in timber structures, an accurate damping ratio is paramount.

The Woodsol system used in this thesis is a promising system for enabling greater architectural flexibility without the need of extensive bracing elements. However, a frame spacing of 2.4 m is difficult to justify in real structures. For the Woodsol system and similar systems to be feasible, a frame-spacing of at least 4 m is desired. To reach such frame spacings, several challenges in the structural system and in practice must be addressed. Such challenges include the limitations to transportation, increasing the connection stiffness without an unpractical deck height, and more.

At present, the Woodsol system does only provide stiffness in one lateral direction. Due to space constraints in the columns, a solution has not yet been found for a connection with stiffnesses in two lateral directions. For this thesis, it is assumed that the stiffness in the crosswind direction is sufficient. If the present Woodsol system is used, shear walls or other types of structural elements which provide bracing stiffness must be used in the lateral direction normal to the connection direction.

The values for the foundation stiffness are approximate values of the same magnitude as common soil types. Soil structure interactions are neglected in this thesis.

### 6.1.2 Wind engineering

In this thesis, the wind loading, and the dynamic response of the structure is estimated through the gust factor approach and the generalized wind load. Wind is an intrinsically stochastic process with random fluctuations in the wind velocity. The gust factor approach is based on the work done in the 60s and 70s by Davenport, Vickery, and others. However, it relies on many simplifications which in sum may add up to be significant. The generalized wind load is based on modal analysis, in which only linear systems can be computed with accuracy. In both the gust factor approach and the generalized wind load, there are several simplifications which may contribute to inaccuracies.

In the gust factor approach, the concept of decoupling the resonant response and the background response may be accurate for heavier structures such as conventional steel and concrete structures. The background response in the gust factor approach is approximated with an algebraic sigmoid. This approximation is a function of the total windward width and height of the structure, and the turbulent length scale. However, it was most likely calibrated for heavier structures than what is the case of timber structures. Thus, it may be a significant source of inaccuracies in the method. In this thesis, the background factor affects the gust factor displacements. The decoupling is reliant on the response spectrum being narrow-banded, which may not always be the case.

For the resonant response in the gust factor approach, the aerodynamic admittance may be the largest source of error. The current aerodynamic admittance used in the Eurocodes was developed based on measurements of cantilevered concrete and steel structures. Thus, it may not be accurately

calibrated for lightweight and flexible timber structures. The result may be an over- or underestimation of the reduction in wind loads.

The generalized wind load method is based on modal analysis, which means that it presumes a linear uncoupled system. The aerodynamic admittance function in the generalized wind load is based on some imaginary quantities, which make it difficult to grasp conceptually. The standard deviation of the response accelerations is based on the generalized wind load. Thus, it should only be accurate for small nonlinearities.

In this thesis, the gust factor approach and the generalized wind load is used to estimate the response accelerations and displacements. In the generalized wind load, time series of 10 minutes are generated for each of the floors for the force based on the force spectrum. The equation of motion is solved numerically for the generated force time series. Due to the stochasticity of the resulting force time series, each unique combination of frame parameters and wind parameters are simulated five times. However, a repetition of five times is not deemed sufficient to effectively quantify the response accelerations. Due to limitations in computing power, more simulations per unique parameter is not feasible due to the time-constraint of this thesis. The total simulation time in this thesis is about one month, and the total duration of the work with this thesis is about five months.

Due to the large deviations between the gust factor approach and the generalized wind load, the reader may ask which method is the best. The goodness of each of the method can only be quantified through experimental verification of the data in this thesis or by other means. Thus, it is not immediately clear which of the methods is the most suitable. However, the gust factor approach tends to produce nonconservative accelerations compared to the generalized wind load for very flexible structures. Compared with theoretical values, the nonconservative tendency of the gust factor approach has also been noted by others such as in Steenbergen et al. (2012) for other structures. For the response displacements, the gust factor approach also produces nonconservative results compared to the generalized wind load. Thus, the accelerations from the gust factor approach should be used with caution for the lightest structures.

### 6.1.3 Proposed nonlinear expressions

The nonlinear regressions in this thesis are performed based on parameters that are deemed important for the behavior of the structural system. However, the proposed expressions are mostly empirical and not derived from theory. The expressions are all done for semi-rigid timber frames, or skeleton systems. Very few structures behave as pure skeleton systems, with most structures having a central core which provides lateral stiffness, and load-sharing walling or cladding to some extent. Thus, their accuracy and applicability for skeleton systems outside the simulated range and for other structural systems should be used with caution. The expressions are calibrated and developed for skeleton timber structures, which are lightweight and flexible. However, similar behavior may be observed in other structures but for different ranges. This applies for the frequency reduction factor and the considerations of nonuniform mass distributions. If possible, the regressions should be recalibrated for the structural system in question and its accuracy validated before it is applied in engineering.

The regressions in this thesis are not dimensionally consistent and are based on empirical relations. The expressions can only be used within the range for which it is calibrated for, and with the input

units that are used in the calibrations. It is not advised to extrapolate the expressions outside the range for which they are calibrated for.

#### 6.1.4 Mass distribution

The analysis of the mass distributions in this thesis are performed for semi-rigid timber structures with ten floors. It is assumed that the behavior of the gust factor accelerations with a unit height factor with respect to the nonuniform mass distributions is present also in other structures. The deviation between the gust factor approach and the generalized wind load for a unit height factor should be investigated further. If the optimal location of a single passive mass is for a unit height factor as the results from the generalized wind load simulations indicate, the location of the mass at lower floors may result in a suboptimal use of resources.

In this thesis, only a single passive mass is considered. The strategy of placing several passive masses at different locations in a timber structure to damp the resonant responses should be investigated further. For taller timber buildings, the effect of higher modes will likely become more prominent due to the flexibility of such structures. Thus, a strategy with several passive masses may be a cost-efficient way of reducing the response accelerations.

## 6.2 Future work

During the work with this thesis, the scope has been the subject of several expansions. The latest additions to this thesis are the frequency reduction factor, and the effect of uniform and nonuniform mass distributions. In the following sections, some areas of future work are identified and briefly presented.

For the structural model, the next natural step is to introduce geometric, material, and numerical nonlinearities. For analyses in the ultimate limit state, a parameter to regulate the density of the finite elements must be introduced to accurately present the force distribution in the system.

For wind engineering, validations of the gust factor approach and the generalized wind load should be carried out in wind tunnel experiments for light and flexible structures. If necessary, the gust factor approach should be recalibrated. In this thesis, only the turbulent component is analyzed. This is appropriate for the accelerations, but insufficient for the displacements. The serviceability of the displacements is in relation to cosmetic crack developments in surface finishes, deformations exceeding tolerances for windows and more. Thus, the peak total displacements should be evaluated for the serviceability with respect to displacements.

For the structural system, an extension of the work in this thesis can be performed for braced and hybrid systems. It is believed that a hybrid system with semi-rigid connections and bracing elements can provide the stiffness needed to design and construct record-breaking tall timber structures.

For the accelerations, the introduction of several passive masses in strategic areas is believed to be a cost-efficient method of reducing the peak dynamic response of the structure. The amount and location of the masses should be optimized with respect to structural efficiency and cost. From the analysis in this thesis of a single passive mass, the reduction in accelerations are promising.

For the Woodsol system, seismic analysis should be carried out to quantify the dynamic response to base accelerations. Stiffer systems are more susceptible to seismic loads due to lesser dissipation of energy.

In the ultimate limit state, the reliability and robustness of the Woodsol system should be quantified.

In timber structures, the structural damping is a topic where there is a considerable knowledge gap. At present, the Timber Group at NTNU has a research project where the structural damping in timber structures is investigated. To accurately predict the dynamic response of timber structures, the structural damping must be quantified and an accurate way of modelling it should be developed.



## 7 Conclusion

In this thesis, more than 12 million simulations of semi-rigid timber frames are carried out. The results quantify the technical feasibility of semi-rigid timber frames with respect to wind-induced serviceability vibrations. Two methods are used to study the structural response and nonlinear regressions are proposed based on the simulations. A sigmoid relationship between the connection stiffness and natural frequency is discovered, and a simple algebraic expression is proposed. An empirical expression for the natural frequency is formulated based on the natural frequencies of the frames. The response accelerations, natural frequency, and mass distribution are studied in-depth. For completeness, response displacements are included as well. However, the response displacements in this thesis do not include the static displacement from the mean wind pressure. In the following paragraphs, the main findings in this thesis are presented.

From the parameter study of the reference frame, the most important structural parameters with respect to the accelerations are the geometry of the structure, quasi-permanent load, connection stiffness, and damping ratio. For the displacements, the most important structural parameters are the geometry and connection stiffness. In general, the semi-rigid frames in this thesis have a natural frequency around 0.4 Hz with most of the frames within the interval between 0.3 Hz and 0.6 Hz. For the mode shape parameter, the median is around 0.63, indicating that the simulated frames are flexible.

For the response accelerations, the gust factor approach may in some cases yield nonconservative results compared with the generalized wind load. The response accelerations from the gust factor approach are more nonconservative for the lightest frames with a quasi-permanent surface load of  $1.6 \text{ kN/m}^2$ , with a median percent bias of about  $-40\%$ . For frames with quasi-permanent surface loads of more than  $7 \text{ kN/m}^2$ , the median is conservative. The Pearson  $R^2$  for the response accelerations between the generalized wind load and the gust factor approach is about 0.93. For the turbulent response displacements, the gust factor approach yields mostly nonconservative results compared with the generalized wind load. The Pearson  $R^2$  for the response displacements between the generalized wind load and the gust factor approach is about 0.97.

Nonlinear regressions of the natural frequency, response accelerations, and response displacements result in reasonable correlation and average error. For the natural frequency, the average error is about 4.3% and the Pearson  $R^2$  is above 0.98. The connection stiffness is almost of equal importance as the column stiffness for the natural frequency. For the response accelerations, the average error for the gust factor approach is about 10.7% and 16.3% for the generalized wind load, and the Pearson  $R^2$  is about 0.97 for the gust factor approach and 0.95 for the generalized wind load. The mean wind velocity is the most important parameter for the response accelerations. For the response displacements, the average error for the gust factor approach is about 13.7% and 18.2% for the generalized wind load, and the Pearson  $R^2$  is above 0.95 for the gust factor approach and 0.92 for the generalized wind load. The reduced correlation and accuracy for the generalized wind load can be attributed to the stochastic variations in the simulations.

The frequency reduction factor shows the dependency of the natural frequency on the connection stiffness. For varying connection stiffnesses, the natural frequency follows a sigmoid shape which can accurately be described by a simple algebraic expression. The frequency reduction factor can be used to quickly assess the natural frequency of a semi-rigid frame based on a rigid frame, without time-consuming modelling of the connections in a finite element software. It is believed that the

sigmoid behavior is present in steel and concrete structures as well. Within the simulated range of parameters, the frequency reduction factor can predict the natural frequency of semi-rigid frames with less than 5% error.

For a basic wind velocity of 22 m/s and a single year return period, all the simulated semi-rigid frames satisfy the wind-induced acceleration criteria of ISO10137-2007 for the gust factor approach and the generalized wind load. For the higher wind velocities of 26 m/s and 30 m/s, most of the simulated semi-rigid frames satisfy the criteria. From this, most of the semi-rigid frames simulated in this thesis can be deemed feasible.

For a uniform mass distribution for structures with ten floors, increasing the mass from 1.6 kN/m<sup>2</sup> to 7 kN/m<sup>2</sup> can reduce the accelerations more than 50% for the gust factor approach, and more than 60% for the generalized wind load. For nonuniform mass distributions, a single passive mass with five times the mass of the quasi-permanent load at the top of the structure can reduce the accelerations by more than 24% for the gust factor approach and the generalized wind load. The optimal location of the passive mass is at the very top of the structure for the generalized wind load, and just below the top for the gust factor approach in the Eurocodes. A deviation between the gust factor approach in the Eurocodes and the generalized wind load is found when the mass is placed at the very top. The normalized modal mass per unit length in the Eurocodes collapses when the mass is placed at the very top. This should be investigated more in-depth.

The strategic location of several passive masses may reduce the structural response in a simple and cost-efficient manner. This strategy is used in the design of super-tall structures today and can readily be applied to tall timber structures.

The results in this thesis are based on the extensive simulations of semi-rigid timber frames. The results show that the semi-rigid frames in this thesis are feasible for timber structures of up to 12 floors with uniform mass distributions. For nonuniform mass distributions, even taller structures can be designed and built to comply with the serviceability criteria. The results are indifferent to the detailed designs of the connections and slab type.

The proposed nonlinear expressions for the response accelerations, natural frequency, and frequency reduction factor provide a simplified method of estimating the structural response and properties. However, their application is limited to the range in which they are calibrated for in this thesis. For structures outside the simulated range, the expressions should be recalibrated and validated for the parameters in question.

## References

- Abrahamsen, R. (2017). *Mjøstårnet - Construction of an 81 m tall timber building*. Paper presented at the Internationales Holzbau-Forum IHF 2017. [https://www.forum-holzbau.com/pdf/31\\_IHF2017\\_Abrahamsen.pdf](https://www.forum-holzbau.com/pdf/31_IHF2017_Abrahamsen.pdf)
- Cook, R. D., Malkus, D. S., Plesha, M. E., & Witt, R. J. (2002). *Concepts and applications of finite element analysis* (4th ed.): John Wiley & Sons. Inc.
- Davenport, A. G. (1961a). The application of statistical concepts to the wind loading of structures. *Proceedings of the Institution of Civil Engineers*, 19(4), 449-472. doi:10.1680/iicep.1961.11304
- Davenport, A. G. (1961b). The spectrum of horizontal gustiness near the ground in high winds. *Quarterly Journal of the Royal Meteorological Society*, 87(372), 194-211. doi:10.1002/qj.49708737208
- Delany, N. K., & Sorensen, N. E. (1953). *Low-speed drag of cylinders of various shapes*.
- Dyrbye, C., & Hansen, S. O. (1997). *Wind Loads on Structures* (1st ed.): John Wiley & Sons Ltd.
- Feldmann, A. H., Haoyu
- Chang, Wen-Shao, Harris, R., Dietsch, P., Gräfe, M., & Hein, C. (2016). *Dynamic properties of tall timber structures under wind-induced vibration*. Paper presented at the WCTE 2016, World Conference on Timber Engineering 2016, Vienna, Austria.
- Forestry, S. (2018). Changing Cities into Forests: Creating Environmentally-Friendly and Timber-Utilizing Cities [Press release]. Retrieved from [http://sfc.jp/english/news/pdf/20180214\\_e\\_01.pdf](http://sfc.jp/english/news/pdf/20180214_e_01.pdf)
- Irwin, P. A. (2010). Vortices and tall buildings: A recipe for resonance. *Physics Today*, 63(9), 68-69. doi:10.1063/1.3490510
- Kaimal, J. C., Wyngaard, J. C., Izumi, Y., & Coté, O. R. (1972). Spectral characteristics of surface-layer turbulence. *Quarterly Journal of the Royal Meteorological Society*, 98(417), 563-589. doi:10.1002/qj.49709841707
- Kareem, A. (1986). Synthesis of Fluctuating along Wind Loads on Buildings. *Journal of Engineering Mechanics*, 112(1), 121-125. doi:doi:10.1061/(ASCE)0733-9399(1986)112:1(121)
- Lui, E. M., & Lopes, A. (1997). Dynamic analysis and response of semirigid frames. *Engineering Structures*, 19(8), 644-654. doi:10.1016/S0141-0296(96)00143-5
- Newland, D. E. (1993). *An introduction to random vibrations, spectral and wavelet analysis* (3rd ed.): Pearson Education Limited.
- Norge, S. (2005). NS-EN 1991-1-4:2005+NA:2009 Eurocode 1: Actions on Structures. Part 1-4: General actions, Wind actions
- In. Norway: Standard Norge.
- Shinozuka, M. (1971). Simulation of Multivariate and Multidimensional Random Processes. *The Journal of the Acoustical Society of America*, 49(1B), 357-368. doi:10.1121/1.1912338
- Shinozuka, M., & Deodatis, G. (1991). Simulation of Stochastic Processes by Spectral Representation. *Applied Mechanics Reviews*, 44(4), 191-204. doi:10.1115/1.3119501
- Simiu, E., & Yeo, D. (2019). *Wind Effects on Structures: Modern Structural Design for Wind* (4th ed.): John Wiley & Sons Ltd.
- Solari, G. (1993a). Gust Buffeting. I: Peak Wind Velocity and Equivalent Pressure. *Journal of Structural Engineering*, 119(2), 365-382. doi:doi:10.1061/(ASCE)0733-9445(1993)119:2(365)
- Solari, G. (1993b). Gust Buffeting. II: Dynamic Alongwind Response. *Journal of Structural Engineering*, 119(2), 383-398. doi:doi:10.1061/(ASCE)0733-9445(1993)119:2(383)
- Solari, G., & Kareem, A. (1998). On the formulation of ASCE7-95 gust effect factor. *Journal of Wind Engineering and Industrial Aerodynamics*, 77-78. doi:10.1016/S0167-6105(98)00182-2

- Stamatopoulos, H. M., Kjell Arne. (2018). *Wood frame solutions for free space design in urban buildings (WOODSOL)*. Paper presented at the 7th Forum Wood Building Nordic Växjö 18, Växjö, Sweden.
- Steenbergen, R. D. J. M., Vrouwenfelder, A. C. W. M., & Geurts, C. P. W. (2012). The use of Eurocode EN 1991-1-4 procedures 1 and 2 for building dynamics, a comparative study. *Journal of Wind Engineering and Industrial Aerodynamics*, 129, 103-106.  
doi:10.1016/j.jweia.2014.03.017.
- Van der Hoven, I. (1957). POWER SPECTRUM OF HORIZONTAL WIND SPEED IN THE FREQUENCY RANGE FROM 0.0007 TO 900 CYCLES PER HOUR. *Journal of Meteorology*, 14(2), 160-164.  
doi:10.1175/1520-0469(1957)014<0160:Psohws>2.0.Co;2
- van Oosterhout, G. P. C. (1996). The wind-induced dynamic response of tall buildings, a comparative study. *Journal of Wind Engineering and Industrial Aerodynamics*, 64(2-3), 135-144.  
doi:10.1016/S0167-6105(96)00063-3
- Vickery, B. (1972). *The provisions and limitations of the Australian Wind Loading Code, AS1170*. Paper presented at the Proceedings of the Australian conference on design & planning of tall buildings, Sydney.
- Vilguts, A., Malo, K. A., & Stamatopoulos, H. (2018). *Moment resisting frames and connections using threaded rods in beam-to-column timber joints*. Paper presented at the WCTE 2018, World Conference on Timber Engineering, Seoul, Republic of Korea.

# Appendices

Appendix A	Planar frame
Appendix B	Wind spectrum
Appendix C	Force time-series
Appendix D	Numerical integration
Appendix E	Gust factor approach
Appendix F	Analysis

## Appendix A: Planar frame

```
function [fn,Kh,Mh,Phi] =
PlanarFrameFunction(Nc,H,L,Nb,bc,hc,bb,hb,rhoc,rhob,Ec,Gc,shc,Eb,Krotb,Kxsup,Kysup,Krotsup,Mfloor
,etaM)
%PlanarFrameFunction.m
% Computes the natural frequencies, stiffness matrix, mass matrix, and
% mode shapes of a frame.

% Haris Stamatopoulos, January 2020
% LEGEND
% Nc - number of columns
% H - floor height
% L - bay length
% Nb - number of bays
% bc - width of the column
% hc - height of the column
% bb - width of the beam
% hb - height of the beam
% rhoc - column density
% rhob - beam density
% Ec - elastic modulus of the column
% Gc - shear modulus of the column
% shc - shear coefficient for the column
% Eb - elastic modulus of the beam
% Krotb - connection stiffness
% Kxsup - horizontal support stiffness
% Kysup - vertical support stiffness
% Krotsup - rotational support stiffness

Lc=repmat(H,1,Nc);
Lb=repmat(L,1,Nb);

Ic = bc*hc^3/12; Ac=bc*hc;
Ib = bb*hb^3/12; Ab=bb*hb;

Nb = numel(Lb); L = sum(Lb); Nc = numel(Lc); h=sum(Lc);

% Xs(1) =0; Ys(1)=0;
Xs=zeros(1,Nb+1);
for m=1:Nb
    Xs(m+1) = Xs(m)+Lb(m);
end

Ys=zeros(1,Nb+1);
for n=1:Nc
    Ys(n+1) = Ys(n)+Lc(n);
end

for m=1:(Nb+1)
    for n=1:(Nc+1)
        Node = (m-1)*(Nc+1)+n;
        X(Node) = Xs(m);
```

```

        Y(Node) = Ys(n);
    end
end

Ndof = (Nc+1)*(Nb+1)*3;
K = zeros(Ndof,Ndof);
M = zeros(Ndof,Ndof);

for m=1:(Nb+1)
    for n=1:Nc
        i =(m-1)*(Nc+1)+n; j=i+1;
        dK = LG(Ndof,SMC(Ec,Ic,Ac,Lc(n),Gc,shc,90),i,j);
        K = K+dK;
        dM = LG(Ndof,MM(rhoc,Ac,Lc(n),90),i,j);
        M = M+dM;
    end
end

for n=2:(Nc+1)
    for m=1:Nb
        i = (m-1)*(Nc+1)+n; j= m*(Nc+1)+n;
        dK = LG(Ndof,SMB(Eb,Ib,Ab,Lb(m),Krotb,0),i,j);
        K = K+dK;
        dM = LG(Ndof,MM(rhob,Ab,Lb(m),0),i,j);
        M = M+dM;
    end
end

Ksupport = zeros(Ndof,Ndof);
for m=1:(Nb+1)
    % Finds the number of the supported nodes (SN) at the bottom
    SN(m) = (m-1)*(Nc+1)+1;
    % Sets the spring stiffness value in the corresponding DOF
    Ksupport(SN(m),SN(m)) = Kxsup ;
    Ksupport(SN(m)+Ndof/3,SN(m)+Ndof/3) = Kysup;
    Ksupport(SN(m)+2*Ndof/3,SN(m)+2*Ndof/3) = Krotsup;
end
K = K + Ksupport;

Ktt=K(1:Ndof/3,1:Ndof/3);      Kt0=K(1:Ndof/3,Ndof/3+1:Ndof);
K0t=K(Ndof/3+1:Ndof,1:Ndof/3); K00=K(Ndof/3+1:Ndof,Ndof/3+1:Ndof);
% Kc: Condensed lateral stiffness matrix
Kc=Ktt-transpose(K0t)*K00^-1*K0t;
% Mc=M(1:Ndof/3,1:Ndof/3);

dKc = zeros(Nc+1,Ndof/3);
for n=1:(Nc+1)
    for m=1:(Nb+1)
        i = (m-1)*(Nc+1)+n; %j= m*(Nc+1)+n;
        dKc(n,:) = dKc(n,)+Kc(i,:);
    end
end
%
dKc2 = zeros(Nc+1,Nc+1);

```

```

for n=1:(Nc+1)
    for m=1:(Nb+1)
        i = (m-1)*(Nc+1)+n; %j= m*(Nc+1)+n;
        dKc2(:,n) = dKc2(:,n)+dKc(:,i);
    end
end
Kh = dKc2;

Mh = zeros(Nc+1,Nc+1);
Mh(1,1)= (Nb+1)*rhoc*Ac*Lc(1)/2;
Mh(Nc+1,Nc+1) = (Nb+1)*rhoc*Ac*Lc(Nc)/2 + rhob*Ab*L;
for i=2:Nc
    Mh(i,i) = (Nb+1)*rhoc*Ac*(Lc(i)+Lc(i-1))/2 + rhob*Ab*L;
end
minus=Nc-Mfloor;
Mh(size(Mh,1)-minus,size(Mh,2)-minus)=Mh(size(Mh,1)-minus,size(Mh,2)-minus)*etaM;

[Phi2,Lambda2]= eig(Kh,Mh); w2 = sqrt((Lambda2));
[w,ind] = sort(diag(w2)); Phi = Phi2(:,ind);
Tn=2*pi./w; fn=1./Tn;

for i=1:size(Phi,1)
    Phi(:,i)=Phi(:,i)/Phi(size(Phi,1),i); % Normalization of eigenmodes
end

end

```

*[Published with MATLAB® R2019a](#)*



```

function [dk] = LG(Ndof,κlocal,i,j)

ki = zeros(Ndof,Ndof);

%-----
ki(i,i)      = κlocal(1,1); ki(i,Ndof/3+i)      = κlocal(1,2); ki(i,2*Ndof/3+i)
= κlocal(1,3);
ki(Ndof/3+i,i) = κlocal(2,1); ki(Ndof/3+i,Ndof/3+i) = κlocal(2,2); ki(Ndof/3+i,2*Ndof/3+i)
= κlocal(2,3);
ki(2*Ndof/3+i,i) = κlocal(3,1); ki(2*Ndof/3+i,Ndof/3+i) = κlocal(3,2); ki(2*Ndof/3+i,2*Ndof/3+i)
= κlocal(3,3);
%-----
ki(i,j)      = κlocal(1,4); ki(i,Ndof/3+j)      = κlocal(1,5); ki(i,2*Ndof/3+j)
= κlocal(1,6);
ki(Ndof/3+i,j) = κlocal(2,4); ki(Ndof/3+i,Ndof/3+j) = κlocal(2,5); ki(Ndof/3+i,2*Ndof/3+j)
= κlocal(2,6);
ki(2*Ndof/3+i,j) = κlocal(3,4); ki(2*Ndof/3+i,Ndof/3+j) = κlocal(3,5); ki(2*Ndof/3+i,2*Ndof/3+j)
= κlocal(3,6);
%-----
ki(j,i)      = κlocal(4,1); ki(j,Ndof/3+i)      = κlocal(4,2); ki(j,2*Ndof/3+i)
= κlocal(4,3);
ki(Ndof/3+j,i) = κlocal(5,1); ki(Ndof/3+j,Ndof/3+i) = κlocal(5,2); ki(Ndof/3+j,2*Ndof/3+i)
= κlocal(5,3);
ki(2*Ndof/3+j,i) = κlocal(6,1); ki(2*Ndof/3+j,Ndof/3+i) = κlocal(6,2); ki(2*Ndof/3+j,2*Ndof/3+i)
= κlocal(6,3);
%-----
ki(j,j)      = κlocal(4,4); ki(j,Ndof/3+j)      = κlocal(4,5); ki(j,2*Ndof/3+j)
= κlocal(4,6);
ki(Ndof/3+j,j) = κlocal(5,4); ki(Ndof/3+j,Ndof/3+j) = κlocal(5,5); ki(Ndof/3+j,2*Ndof/3+j)
= κlocal(5,6);
ki(2*Ndof/3+j,j) = κlocal(6,4); ki(2*Ndof/3+j,Ndof/3+j) = κlocal(6,5); ki(2*Ndof/3+j,2*Ndof/3+j)
= κlocal(6,6);
%-----

dk = ki;

end

```

*Published with MATLAB® R2019a*

```

function [Mg1] = MM(rho,A,L,theta)

% Angle
c = cosd(theta); s = sind(theta);

% Transformation matrix
T = [c s 0 0 0 0;...
     -s c 0 0 0 0;...
     0 0 1 0 0 0;
     0 0 0 c s 0;...
     0 0 0 -s c 0;...
     0 0 0 0 0 1];

Mlocal = rho*A*L/420*[140  0  0  70  0  0; ...
                    0 156 22*L  0  54 -13*L; ...
                    0 22*L  4*L^2  0 13*L -3*L^2;...
                    70  0  0  140  0  0;...
                    0  54 13*L  0 156 -22*L;...
                    0 -13*L -3*L^2  0 -22*L  4*L^2];

Mg1 = T*Mlocal*transpose(T);

end

```

*[Published with MATLAB® R2019a](#)*

```

function [Kg] = SMB(E,I,A,L,Krot,theta)

% Rotational flexibility % Reference: M.A. Hadianfard*, R. Razani 2001
Rstar = (1+4*E*I/(L*Krot))^2-(E*I/L)^2*4/Krot^2;
Sii = (4+12*E*I/(L*Krot))/Rstar; Sij = 2/Rstar;

% Shear deformation (Reference Henri P. Gavin 2018)
%sh = 0; %sh=12*E*I/(G*A/a*Lb^2) a=6/5

% Angle
c = cosd(theta); s = sind(theta);

% Transformation matrix
T = [c s 0 0 0 0;...
     -s c 0 0 0 0;...
     0 0 1 0 0 0;
     0 0 0 c s 0;...
     0 0 0 -s c 0;...
     0 0 0 0 0 1];

Klocal = E*I/L*[A/I      0      0      -A/I      0      0;...
                0  2*(Sii+Sij)/L^2  (Sii+Sij)/L  0      -2*(Sii+Sij)/L^2  (Sii+Sij)/L; ...
                0      (Sii+Sij)/L      Sii  0      -(Sii+Sij)/L      Sij;...
                -A/I      0      0      A/I      0      0;...
                0  -2*(Sii+Sij)/L^2  -(Sii+Sij)/L  0      2*(Sii+Sij)/L^2  -(Sii+Sij)/L;...
                0      (Sii+Sij)/L      Sij  0      -(Sii+Sij)/L      Sii];

Kg = T*Klocal*transpose(T);
end

```

*[Published with MATLAB® R2019a](#)*

```

function [Kg1] = SMC(E,I,A,L,G,sh,theta)

% Rotational flexibility % Reference: M.A. Hadianfard*, R. Razani 2001
% Off: not needed in columns

% Shear deformation (Reference Henri P. Gavin 2018)
ash=12*E*I/(G*A/sh*L^2);

% Angle
c = cosd(theta); s = sind(theta);

% Transformation matrix
T = [c s 0 0 0 0;...
     -s c 0 0 0 0;...
     0 0 1 0 0 0;
     0 0 0 c s 0;...
     0 0 0 -s c 0;...
     0 0 0 0 0 1];

klocal = [A*E/L          0          0 -A*E/L          0
0;...
          0 (1/(1+ash))*12*E*I/L^3 (1/(1+ash))*6*E*I/L^2 0 -(1/(1+ash))*12*E*I/L^3
(1/(1+ash))*6*E*I/L^2; ...
          0 (1/(1+ash))*6*E*I/L^2 (4+ash)/(1+ash)*E*I/L 0 -(1/(1+ash))*6*E*I/L^2
(2-ash)/(1+ash)*E*I/L; ...
-A*E/L          0          0 A*E/L          0
0;...
          0 -(1/(1+ash))*12*E*I/L^3 -(1/(1+ash))*6*E*I/L^2 0 (1/(1+ash))*12*E*I/L^3
-(1/(1+ash))*6*E*I/L^2; ...
          0 (1/(1+ash))*6*E*I/L^2 (2-ash)/(1+ash)*E*I/L 0 -(1/(1+ash))*6*E*I/L^2
(4+ash)/(1+ash)*E*I/L];

Kg1 = T*klocal*transpose(T);
end

```

*[Published with MATLAB® R2019a](#)*

## Appendix B: Wind spectrum

```
function [vm,Lt,Iu,f,Suu] =  
WindCPSDFunction(R, KK, n, cdir, cseason, calt, vb0, z, z0, zmin, zmax, zt, y, kr, co, Ltr, T, fmax, Cuz, Cuy)
```

```
%WindCPSDFunction.m  
% Generates a correlated cross-spectral density of the wind velocity  
  
% Alex Sixie Cao, January 2020  
% LEGEND  
% R - return period  
% KK - shape parameter  
% n - exponent  
% cdir - direction factor  
% cseason - season factor  
% calt - altitude factor  
% vb0 - basic wind velocity  
% z - height vector  
% z0 - roughness length  
% zmin - minimum height  
% zmax - maximum height  
% zt - reference height for the turbulence length scale  
% y - windward width vector  
% kr - terrain factor  
% co - orography factor  
% Ltr - reference turbulence length scale  
% T - averaging time  
% fmax - maximum frequency in the frequency axis  
% Cuz - vertical decay coefficient  
% Cuy - horizontal decay coefficient
```

### Basic values NS-EN 1991-1-4:2005 Section 4.2

```
cprob=cprobFunction(R, KK, n); % Probability factor NA.4.1  
vb=cdir*cseason*calt*cprob*vb0; % Basic wind velocity NA.4.2(2)
```

### Mean wind NS-EN 1991-1-4:2005 Section 4.3

```
cr=TerrainRoughnessFactor(z, z0, zmin, zmax, kr); % Terrain roughness factor  
vm=cr*co*vb; % Mean wind velocity profile 4.3.1 Eq.4.3
```

### Wind turbulence NS-EN 1991-1-4:2005 Section 4.4

```
k1=1; % Turbulence factor 4.4(1)*  
[stdu, Iu]=TurbulenceIntensity(z, z0, zmin, zmax, vm, kr, k1, vb);
```

### Wind field characteristics NS-EN 1991-1-4:2005 Annex B

```
Lt=TurbulenceLengthScale(z, zt, z0, zmin, Ltr);  
NPSD=2^log2((T+0.5)*fmax);
```

```
[f,Su]=KaimalSpectrum(NPSD,fmax,z,vm,stdu,Lt);  
Suu=CowindSpectrum(z,y,f,Su,Cuz,Cuy,vm);
```

```
end
```

*[Published with MATLAB® R2019a](#)*

```

function [cprob] = cprobFunction(R,K,n)
% cprob.m Probability factor in NS-EN 1991-1-4:2005 Section 4.2
% Probability factor of annual exceedance

% Alex Sixie Cao, February 2020
% LEGEND
% R - return period
% K - shape parameter
% n - exponent

p=1/R;
if R<=1.4
    cprob=0.73;
elseif R<1
    error('Return period must be larger than 1.4\n')
else
    cprob=((1-K*log(-log(1-p)))/(1-K*log(-log(0.98))))^n;
end
end

```

*Published with MATLAB® R2019a*

```

function [cr] = TerrainRoughnessFactor(z,z0,zmin,zmax,kr)
%TerrainRoughnessFactor.m generates terrain roughness factors
% Generates terrain roughness factors according to
% NS-EN 1991-1-4:2005 Section 4.3

% Alex Sixie Cao, January 2020
% LEGEND
% z - vertical axis
% z0 - roughness length
% zmin - minimum height
% zmax - maximum height
% kr - terrain factor

cr=zeros(1,length(z)); % Pre-allocation
for i=1:length(z)
    if z(i)>=zmin && z(i)<=zmax
        cr(i)=kr*log(z(i)/z0); % Roughness factor
    else
        cr(i)=kr*log(zmin/z0); % Roughness factor close to ground
    end
end
end
end

```

*Published with MATLAB® R2019a*



```

function [stdu,Iu] = TurbulenceIntensity(z,z0,zmin,zmax,vm,kr,k1,vb)
%TurbulenceIntensity.m generates turbulence intensities
% Generates turbulence intensities according to
% NS-EN 1991-1-4:2005 Section 4.4

% Alex Sixie Cao, January 2020
% LEGEND
% z - vertical axis
% z0 - roughness length
% zmin - minimum height
% zmax - maximum height
% vm - mean wind speed profile
% kr - terrain factor
% k1 - turbulence factor
% vb - basic wind velocity

stdu=kr.*vb.*k1; % standard deviation of the along-wind speed
Iu=zeros(1,length(z)); % Pre-allocation
for i=1:length(z)
    if z(i)>=zmin && z(i)<=zmax
        Iu(i)=stdu./vm(i); % Turbulence intensity along-wind, 10 min
    else
        Iu(i)=stdu./(kr*log(zmin/z0)); % Turbulence intensity along-wind close to ground (10 min)
    end
end
end
end

```

*[Published with MATLAB® R2019a](#)*

```

function [L] = TurbulenceLengthScale(z,zt,z0,zmin,Lt)
%TurbulenceLengthScale.m Generates turbulence length scales
% Generates turbulence length scales according to
% NS-EN 1991-1-4:2005 Annex B.1 wind turbulence

% Alex Sixie Cao, January 2020
% LEGEND
% z - vertical axis
% zt - reference height
% z0 - roughness length
% zmin - minimum height
% Lt - reference length scale
% L - along-wind turbulence length scale

alpha=0.67+0.05*log(z0); % Exponent
L=zeros(1,length(z)); % Pre-allocation
for i=1:length(z)
    if z(i)>zmin
        L(i)=Lt*(z(i)/zt)^alpha; % Turbulence length scale
    elseif z(i)<=zmin
        L(i)=Lt*(zmin/zt)^alpha; % Turbulence length scale
    end
end
end
end

```

*[Published with MATLAB® R2019a](#)*

```

function [f,Su] = KaimalSpectrum(NPSD,fmax,z,vm,stdu,L)
%KaimalSpectrum.m generates a single-point Kaimal spectrum
% Generates a single-point Kaimal spectrum according to
% NS-EN 1991-1-4:2005 Annex B.1 Wind Turbulence

% Alex Sixie Cao, January 2020
% LEGEND
% NPSD - number of sampling points
% fmax - maximum sampling frequency
% z - vertical axis
% vm - mean along-wind speed
% stdu - standard deviation of the along-wind speed
% L - Turbulence length scale
% f - frequency axis
% Su - single-point power spectral density

f=linspace(0,fmax,NPSD); % Frequency axis
Au=6.8; % NS-EN 1991-1-4:2005 Annex B
Su=zeros(length(z),length(f)); % Pre-allocation
for zz=1:length(z)
    for n=1:length(f)
        Su(zz,n)=stdu^2*L(zz)/vm(zz)*Au/(1+1.5*Au*f(n)*L(zz)/vm(zz))^(5/3); % Single-point
    spectrum
    end
end
end
end

```

*[Published with MATLAB® R2019a](#)*

```

function [Suu] = CowindSpectrum(z,y,f,Su,Cuz,Cuy,vm)
%CowindSpectrum.m generates cross-spectral wind densities
% Generates cross-spectral densities according to Steenbergen et al.
% (2012)

% Alex Sixie Cao, January 2020
% LEGEND
% z - vertical axis
% y - lateral axis
% f - frequency axis
% Su - single-point power spectral density
% Cuz - vertical decay coefficient
% Cuy - lateral decay coefficient
% vm - mean along-wind speed

Suu=zeros(length(z),length(z),length(f)); % Pre-allocation
for ff=1:length(f)
    for z1=1:length(z)
        for z2=z1:length(z)
            %
            coh=exp(-2*f(ff)/(vm(z1)+vm(z2)))*sqrt(Cuz^2*(z(z2)-z(z1))^2+Cuy^2*(y(z2)-
y(z1))^2)); % Coherence function
            Suu(z1,z2,ff)=sqrt(Su(z1,ff)*Su(z2,ff)); % Joint spectrum
            %
            Suu(z1,z2,ff)=coh*S; %Co-spectrum
        end
    end
end
end
end

```

*Published with MATLAB® R2019a*

## Appendix C: Force time-series

```
function [Fb_time,t] = ModalForceTimeHistoryFunction(z,f,Phi,SFF,N)
%ModalForceTimeHistory.m
% Generates a modal force history from a cross-spectral density

% Alex Sixie Cao, January 2020
% LEGEND
% z - height vector
% f - frequency axis
% Phi - mode shapes
% SFF - cross-spectral density of the force
% N - number of floors
Fb_time=zeros(length(z),2^nextpow2(2*length(f)),length(Phi)); % Pre-allocation
for n=1:N
    [Fb_time(:,:,n),df,NFFT]=TimeHistory(SFF(:,:,n),f,N); % Buffeting force time history for
all n eigenmodes
end
t=linspace(0,1/df,NFFT); % Time axis
end
```

*[Published with MATLAB® R2019a](#)*

```

function [SFF] = ForceCPSDFunction(Phi,f,z,y,vm,Cuz,Cuy,h,d,rho,A,Suu)
%ForceCPSDFunction
% Generates the cross-spectral density of the wind force according to
% Steenbergen et al. (2012)

% Alex Sixie Cao, January 2020
% LEGEND
% Phi - mode shapes
% f - frequency axis
% z - windward height vector
% y - windward width vector
% vm - mean wind velocity
% Cuz - vertical decay coefficient
% Cuy - horizontal decay coefficient
% h - windward height
% d - windward depth
% rho - air density
% A - windward area
% Suu - cross-spectral density of the wind velocity

chi2=AerodynamicAdmittance(Phi,f,z,y,vm,Cuz,Cuy); % Aerodynamic admittance function
cpe=PressureCoefficient(h,d); % Pressure coefficient
SFF=CoForceSpectrum(Phi,z,f,cpe,rho,vm,A,chi2,Suu); % Buffeting force spectrum
end

```

*[Published with MATLAB® R2019a](#)*

```

function [Chi2] = AerodynamicAdmittance(Phi,f,z,y,vm,Cuz,Cuy)
%AerodynamicAdmittance.m calculates the N aerodynamic admittance functions
% Generates Aerodynamic Admittance Functions (AAF) for all eigenmodes
% Phi. The AAF used is based eq.8 in Steenbergen et al. (2012), proposed
% by Hansen and Krenk (1999).

% Alex Sixie Cao, January 2020
%LEGEND
% Phi - eigenmodes
% f - frequency axis
% z - vertical axis
% y - lateral axis
% vm - mean along-wind speed profile
% Cuz - vertical decay coefficient
% Cuy - horizontal decay coefficient

H=z(length(z));
Chi2=zeros(length(f),size(Phi,1));
for n=1:size(Phi,1)
    p=Phi(:,n);
    for ff=1:length(f)
        for z1=1:length(z)
            for z2=1:length(z)
                coh=exp(-2*f(ff)/(vm(z1)+vm(z2))*sqrt(Cuz^2*(z(z2)-z(z1))^2+Cuy^2*(y(z2)-
y(z1))^2));
                pp=p(z1)*p(z2);
                v=vm(z1)*vm(z2)/(0.6*z(end))^2;
                I(z1,z2)=coh*pp*v;
            end
        end
        Chi2(ff,n)=1/H^2*trapz(z,trapz(z,I));
    end
end
end

```

*[Published with MATLAB® R2019a](#)*

```
function [cpe] = PressureCoefficient(h,d)
%PressureCoefficient.m
% Computes the external pressure coefficient according to NS-EN
% 1991-1-4:2005 Section 7.2.2

% Alex Sixie Cao, February 2020
% LEGEND
% h - windward width
% d - windward depth

if h/d<=0.25
    cpe=0.7+0.3; % External pressure coefficient
elseif h/d==1
    cpe=0.8+0.5;
else
    cpe=0.8+0.7;
end
end
```

*Published with MATLAB® R2019a*



```

function [SFF] = CoForceSpectrum(Phi,z,f,cp,rho,vm,A,chi2,Suu)
%CoForceSpectrum.m generates cross-spectral force densities
% Generates cross-spectral force densities from cross-spectral wind
% densities Suu and aerodynamic admittance functions chi2.

% Alex Sixie Cao, January 2020
% LEGEND
% Phi - eigenmodes
% z - vertical axis
% f - frequency axis
% cp - pressure coefficient
% rho - air density
% vm - mean along-wind speed
% A - force area vector
% chi2 - aerodynamic admittance functions
% Suu - cross-spectral wind densities

vm=0.6*z(end);
SFF=zeros(length(z),length(z),length(f),length(Phi)); % Pre-allocation
for n=1:length(Phi)
    for ff=1:length(f)
        for z1=1:length(z)
            for z2=1:length(z)
                SFF(z1,z2,ff,n)=(cp*rho*vm*A(z1))^2*abs(chi2(ff,n))*Suu(z1,z2,ff); % Buffeting
force spectrum
            end
        end
    end
end
end
end

```

*Published with MATLAB® R2019a*

## Appendix D : Numerical integration

```
function [u,udot,u2dot] = TimeIntegrationFunction(zeta,fn,modes,m,k,Phi,Fb_time,t)
%TimeIntegrationFunction.m
% Computes the total response of the structure

% Alex Sixie Cao, January 2020
% LEGEND
% zeta - damping ratio
% fn - fundamental natural frequency
% modes - number of modes for Rayleigh matrix
% m - mass matrix
% k - stiffness matrix
% Phi - mode shapes
% Fb_time - force history
% t - time vector

% Rayleigh damping
a0=zeta*2*fn(1)*fn(modes)/(fn(1)+fn(modes));
a1=zeta*2/(fn(1)+fn(modes));
c=a0*m+a1*k; % Damping matrix

% Normalization of modes
K=zeros(1,size(Phi,2)); M=zeros(1,size(Phi,2)); C=zeros(1,size(Phi,2));
P=zeros(size(Fb_time,2),size(Fb_time,1));
for n=1:size(Phi,2)
    K(n)=Phi(:,n)'*k*Phi(:,n);
    M(n)=Phi(:,n)'*m*Phi(:,n);
    C(n)=Phi(:,n)'*c*Phi(:,n);
    P(:,n)=Phi(:,n)'*Fb_time(:, :, n);
end

% Newmark integration of the equation of motion
gam=1/2; beta=1/4; % Undamped constant average acceleration method, implicit;
q0=zeros(size(K,1),1); qdot0=zeros(size(K,1),1); % Initial conditions

q=zeros(size(Phi,2),size(P,1));
qdot=zeros(size(Phi,2),size(P,1));
q2dot=zeros(size(Phi,2),size(P,1));
for n=1:size(Phi,2)
    [q(n,:),qdot(n,:),q2dot(n,:)] = NewmarkInt(t,M(n),C(n),K(n),P(:,n)',gam,beta,q0,qdot0); %
    Newmark integration
end
u=Phi(:,1:modes)*q(1:modes,:); % Response displacement
udot=Phi(:,1:modes)*qdot(1:modes,:); % Response velocity
u2dot=Phi(:,1:modes)*q2dot(1:modes,:); % Response acceleration
end
```

*Published with MATLAB® R2019a*

```
function [u udot u2dot] = NewmarkInt(t,M,C,K,P,gam,beta,u0,udot0)
```

```
%Newmark's Direct Integration Method
%-----
% OUTPUT
% u =      Displacemente Response   [n,2]
% (n = number of time steps)
% (ndof = number degrees of freedom)

% INPUT
% t =      Time vector              [1,n]
% M =      mass matrix              [ndof,ndof]
% C =      damping matrix           [ndof,ndof]
% K =      stiffness matrix         [ndof,ndof]
% P =      load vs. time            [ndof,n]
% gam =    gamma (constant)
% beta =   beta (constant)
% u0 =     Initial displacements
% udot0 =  Initial velocity

%-----
% beta = 0,   gamma = 1/2 -> explicit central difference method
% beta = 1/4, gamma = 1/2 -> undamped trapezoidal rule (implicit)
```

## 1.0 Initial calculations

```
%1.1
u=zeros(size(M,1),length(t));
u(:,1)=u0;
udot=udot0;
u2dot = M\(P(:,1)-C*udot0-K*u0);

%1.2
dt = t(2) - t(1);
%1.3
kgor = K + gam/(beta*dt)*C + M*1/(beta*dt^2);
%1.4
a = M/(beta*dt) + gam/beta*C;
b = 0.5*M/beta + dt*(0.5*gam/beta - 1)*C;
```

## 2.0 Calculations for each time step i

```
for i = 1:(length(t)-1)
    %2.1
    deltaP = P(:,i+1)-P(:,i) + a*udot(:,i) + b*u2dot(:,i);
    %2.2
    du_i = kgor\deltaP;
    %2.3
    dudot_i = gam/(beta*dt)*du_i - gam/beta*udot(:,i) + dt*(1-0.5*gam/beta)*u2dot(:,i);
    %2.4
    du2dot_i = 1/(beta*dt^2)*du_i - 1/(beta*dt)*udot(:,i) - 0.5/beta*u2dot(:,i);
    %2.5
```

```
u(:,i+1) = du_i + u(:,i);  
udot(:,i+1) = dudot_i + udot(:,i);  
u2dot(:,i+1) = du2dot_i + u2dot(:,i);  
end  
  
% u = u';  
% udot=udot';  
% u2dot=u2dot';
```

*Published with MATLAB® R2019a*

## Appendix E: Gust factor approach

```
function [ustaticp, stdax, kpa, kpc] =
GustFactorFunction(b, H, d, h, z, A, N, Lt, Iu, vm, rho, fn, k, m, zeta, Phi, t)
%GustFactorFunction.m
% Computes the static displacement, acceleration, and peak factors
% according to NS-EN 1991-1-4:2005 Annex B

% Alex Sixie Cao, March 2020
% LEGEND
% b - windward width
% H - floor height
% d - windward depth
% z - height vector
% A - windward width
% N - number of floors
% Lt - turbulence length scale
% Iu - turbulence intensity
% vm - mean wind velocity
% rho - air density
% fn - fundamental natural frequency
% k - stiffness matrix
% m - mass matrix
% zeta - damping ratio
% Phi - mode shape
% t - time vector

% Structural factor
B2=1./(1+0.9*((b+h)./Lt(round(0.6*h/H)+1)).^0.63); % Background factor
SLr=Lt(round(0.6*h/H)+1)/vm(round(0.6*h/H)+1)*6.8/(1+1.5*6.8*fn(1)*Lt(round(0.6*h/H)+1)/vm(round(
0.6*h/H)+1))^5/3)*fn(1); % Non-dimensional power spectral density
fLr=fn(1)*Lt(round(0.6*h/H)+1)/vm(round(0.6*h/H)+1); % Non-dimensional frequency at reference
height
etah=4.6*h./Lt(round(0.6*h/H)+1)*fLr; etab=4.6*b./Lt(round(0.6*h/H)+1)*fLr;
Rh=1/etah-1/(2*etah^2)*(1-exp(-2*etah)); % Aerodynamic admittance, height
Rb=1/etab-1/(2*etab^2)*(1-exp(-2*etab)); % Aerodynamic admittance, width
delta=2*pi*zeta; % Logarithmic decrement
R2=pi^2/(2*delta)*SLr*Rh*Rb; % Resonance response factor

nu=fn(1)*sqrt(R2/(B2+R2)); % Up-crossing rate for the structural factor
if nu<0.08
    nu=0.08;
end

kpc=sqrt(2*log(nu*t(end)))+0.6/sqrt(2*log(nu*t(end))); % Peak factor for the structural factor
if kpc<3
    kpc=3;
end

kpa=sqrt(2*log(fn(1)*t(end)))+0.6/sqrt(2*log(fn(1)*t(end))); % Peak factor for turbulent part
only
if kpa<3
    kpa=3;
```

```

end

% cs=(1+7*Iu(round(0.6*h/H)+1)*sqrt(B2))/(1+7*Iu(round(0.6*h/H)+1)); % Static factor
cs=1;
% cd=(1+2*kpc*Iu(round(0.6*h/H)+1)*sqrt(B2+R2))/(1+7*Iu(round(0.6*h/H)+1)*sqrt(B2)); % Dynamic
factor
cd=(2*kpc*Iu(round(0.6*h/H)+1)*sqrt(B2+R2))/(1+7*Iu(round(0.6*h/H)+1)*sqrt(B2)); % Dynamic factor
cscd=cs*cd; % Structural factor;

qm=1/2*rho*vm.^2; % Mean velocity pressure NA.4.5
% qp=(1+2*kpc*Iu).*qm; % Peak velocity pressure NA.4.5
qp=(2*kpc*Iu).*qm; % Peak velocity pressure, turbulent
qpe=zeros(1,length(qp)); % Peak velocity pressure
for i=1:length(z)
    if z(i)<b && round(b/h+1)<=N
        qpe(i)=qp(round(b/h+1));
    elseif z(i)<b && round(b/h+1)>N
        qpe(i)=qp(N);
    elseif b/(h-z(i))>1
        qpe(i)=qp(end);
    else
        qpe(i)=qp(i);
    end
end

cf=ForceCoefficient(d,b,h); % Force coefficient
Fwep=cscd*cf.*A'*qp(round(0.6*h/H)+1); % Peak external forces, turbulent
ustaticp=(Fwep'/k)'; % Peak static displacement, turbulent

Kx=trapz(z,vm.^2'.*Phi(:,1))/(vm(round(0.6*h/H)+1)^2*trapz(z,Phi(:,1).^2));
m1x=trapz(z,Phi(:,1).^2.*diag(m))/trapz(z,Phi(:,1).^2); % Equivalent mass

stdax=cf*rho*b*Iu(round(0.6*h/H)+1)*vm(round(0.6*h/H)+1)^2*sqrt(R2)*Phi(:,1)*Kx/m1x; % Standard
deviation of response acceleration

end

```

*[Published with MATLAB® R2019a](#)*

```

function [cf] = ForceCoefficient(d,b,h)
%ForceCoefficient.m
% Drag or force coefficient in NS-EN 1991-1-4:2005 Section 7.6

% Alex Sixie Cao, February 2020
% LEGEND
% d - windward depth
% b - windward width
% h - windward height

if d/b<0.2
    cf0=2; % Force coefficient
elseif d/b<0.6
    cf0=2+(2.35-2)/(0.6-0.2)*(d/b-0.2);
elseif d/b<0.7
    cf0=2.35+(2.4-2.35)/(0.7-0.6)*(d/b-0.6);
elseif d/b<1
    cf0=2.4+(2.1-2.4)/(1-0.7)*(d/b-0.7);
elseif d/b<2
    cf0=2.1+(1.65-2.1)/(2-1)*(d/b-1);
elseif d/b<5
    cf0=1.65+(1.0-1.65)/(5-2)*(d/b-2);
elseif d/b<10
    cf0=1.0+(0.9-1.0)/(10-5)*(d/b-5);
else
    cf0=0.9;
end

psir=1.0; % Sharp corners

if max([b,h])<=50
    lambda=min([1.4*max([b,h])/min([b,h]),70]);
elseif max([b,h])<15
    lambda=min([2*max([b,h])/min([b,h]),70]);
else
    lambda=2*15+(1.4*50/min([b,h])-2*15/min([b,h]))/(50-15)*(max([b,h])-15);
end

phi=1; % solidity ratio

if lambda<10
    psilambda=0.61+(0.69-0.61)/(10-1)*(lambda-1);
elseif lambda<70
    psilambda=0.69+(0.915-0.69)/(70-10)*(lambda-10);
else
    psilambda=0.915+(1-0.915)/(200-70)*(lambda-70);
end

cf=cf0*psilambda*psir; % Force coefficient
end

```

*Published with MATLAB® R2019a*

## Appendix F: Analysis

```
function [kpa,kpc, stdax, stdu2dot, stdu, ustaticp, fn, Phi, IDRGFp, IDRGLStd] =
AnalysisFunction(R, vb0, N, Nb, Eb, Ec, Gc, shc, hc, hb, bc, bb, Krotb, Kxsup, Kzsup, Lb, H, W, s, xi, p, rhoc, Mfloor
, etaM)
%AnalysisFunction.m
% Computes the peak factor, dynamic response, natural frequency, mode
% shapes, and IDR for a set of parameters

% Alex Sixie Cao, May 2020
% LEGEND
% N - number of floors
% Nb - number of bays
% hb - beam height
% hc - column height
% Krotb - connection stiffness
% Kxsup - horizontal support stiffness
% Kzsup - vertical support stiffness
% Krotsup - rotational support stiffness
% Lb - bay length
% H - floor height
% W - windward width
% p - surface load
% vb0 - basic wind velocity
% s - frame spacing
% xi - damping ratio

modes=N;
```

## Constants

```
run('ConstantsAll.m')
```

## Basic parameters

```
z=linspace(0,N*H,(N+1)); % Height vector
y=linspace(-w/2,w/2,(N+1)); % width vector of windward facade
h=N*H; % Building height
d=Lb*Nb; % Building depth
A=w*[0.5 linspace(1,1,(N-1)) 0.5]*H; % Area vector
rhob=p*s/hb/bb/9.81; % Equivalent density

% Power spectral density, wind velocity
[vm, Lt, Iu, f, Suu] =
windCPSDFFunction(R, KK, n, cdir, cseason, calt, vb0, z, z0, zmin, zmax, zt, y, kr, co, Ltr, T, fmax, Cuz, Cuy);
% Output: vm, Lt, Iu, f, Suu
```

## Planar frame

```
Kxsup=Ksup; Kzsup=Ksup;
[fn, Kh, Mh, Phi]=PlanarFrameFunction(N, H, Lb, Nb, bc, hc, bb, hb, rhoc, rhob, Ec, Gc, shc, Eb, Krotb, Kxsup, Kzsup
```



```
,Krotsup,Mfloor,etaM);
fn=fn';
k=round(w/s)*kh; m=round(w/s)*Mh;

clear fnh kh Mh
% Output: fn, k, m, Phi
```

## Generalized wind load

```
[SFF] = ForceCPSDFunction(Phi, f, z, y, vm, Cuz, Cuy, h, d, rho, A, Suu);
% Output: SFF

% Modal buffeting force time history
[Fb_time,t] = ModalForceTimeHistoryFunction(z, f, Phi, SFF, N);
% Output: Fb_time

% Time history turbulence response
[u,~,u2dot] = TimeIntegrationFunction(xi, fn, modes, m, k, Phi, Fb_time, t);
% Output: u, udot, u2dot
% u2dot=u2dot(end,:); % For Nfloor simulations uudot(:)=uudot(end,:);

% Standard deviation
stdu=zeros(N+1,1)';
stdu2dot=zeros(N+1,1)';
for i=1:N+1
    stdu(i)=std(u(i,:))';
    stdu2dot(i)=std(u2dot(i,:))';
end
IDRGWLstd=(diff(stdu)/H)';
```

## Gust factor approach

```
[ustaticp, stdax, kpa, kpc] = GustFactorFunction(W, H, d, h, z, A, N, Lt, Iu, vm, rho, fn, k, m, xi, Phi, T);
ustaticp=ustaticp';
stdax=stdax(end);
kpa=kpa(end);
kpc=kpc(end);
IDRGFp=(diff(ustaticp)/H)';

end
```

*Published with MATLAB® R2019a*

```

% Constants.m

% Time history
T=600; % Simulation time
fmax=3; % Cut-off frequency
R=1; % Return period of exceedance

% Wind velocity
% vb0=26; % Fundamental value of the basic wind velocity, Trondheim (Oslo=22)
cdir=1.0; cseason=1.0; calt=1.0; % Direction, season, altitude factors
n=0.5; % Exponent 4.2(2)
KK=0.2; % Shape parameter depending on cov of the extreme value distribution 4.2(2)

% Turbulence
kl=1; % Turbulence factor 4.4(1)*
kp=3.5; % Peak factor NA.4.5
rho=1.25; % Air density 4.5(1)
zt=200; % Reference height, NS-EN 1991-1-4:2005 Annex B
Ltr=300; % Reference length scale, NS-EN 1991-1-4:2005 Annex B

% Terrain
zmin=8; % Minimum height NA.4.3.2
zmax=200; % Maximum height 4.3.2(1)
z0=0.3; % Roughness length NA.4.3.2
kr=0.22; % Terrain factor NA.4.3.2
co=1.0; % Terrain orography factor 4.3.1(1)

% Cross-spectral density
Cuz=11.5; Cuy=11.5;

```

*[Published with MATLAB® R2019a](#)*